Segmented Hollow Core Photonic Crystal Fiber as a Gas Cell

By

Joshua Ottorino Trevisanutto

A thesis submitted to the Faculty of Graduate Studies
Lakehead University
In partial fulfillment of the requirements for the degree of
Doctor of Philosophy
Chemistry and Materials Science

Lakehead University
December 2022

Abstract

Developing a unique gas cell based on hollow core photonic crystal fiber (HC-PCF) improving its ability to be used in measurements which require higher temporal resolution. Traditional HC-PCF is an excellent candidate for a gas cell due to its extremely small filling volume combined with its small footprint, however a detriment it suffers from is an extraordinarily long fill and evacuation time, a matter of hours for cells surpassing 10 m. The HC-PCF in this work was segmented into smaller lengths, with each segment allowing gas to enter and exit the fiber. By stringing multiple segments of HC-PCF together one can increase to overall length of the gas cell, thus lowering the detection limit of the system, without increasing the fill and evacuation time required to saturate the HC-PCF with gas. By segmenting HC-PCF the fill time can be reduced to a matter of minutes, which makes it an attractive candidate for use in a remote monitoring setting due to the fact that it can operate in the telecommunications band, reducing the cost of implementing such a system, as well as operating at room temperature, removing the need to power an active cooling system.

Contributions

Peer-reviewed:

Article in communication with Measurement: Sensors – Joshua O. Trevisanutto and G. Das, "Detection of C_2H_2 at parts per million (ppmv) using a fiber laser system", Submitted on July 14, 2022.

Joshua O. Trevisanutto and G. Das, "Gas Cell based on Segmented Hollow-Core Photonic Crystal Fiber and its Application in an Intracavity Absorption Spectroscopy System", CLEO 2021, Virtual, USA, May 12, 2021.

Presentations at the Canadian Association of Physicists:

Joshua O. Trevisanutto and G. Das, "Gas Cell Based on Hollow-Core Fiber for Trace Gas Detection", CAP Congress 2019, Simon Fraser University, June 2-7, 2019.

G. Das and Joshua O. Trevisanutto, "Photonic Device for Gas Detection", CAP Congress 2019, Simon Fraser University, June 2-7, 2019.

Joshua O. Trevisanutto, Jonas K. Valiunas and G. Das, "Photonic device for the detection of trace gases, CAP Conference, Dalhousie University, Halifax, Nova Scotia, June 11-15, 2018.

Acknowledgements

Thank you to my supervisor Dr. Gautam Das, who gave me the opportunity to work with both him and the Photonics Research Group here at Lakehead University. His constant support and motivation made this possible, along with the infrastructure he has painstakingly developed over the years.

I would also like to thank all past and present members of the Photonics Research Group who have helped to develop both this project and others over the years. It has been a pleasure working with everyone here, and I look forward to collaborating with all of my peers in the future.

Dedication

To my mother and sisters, Sandy, Jenna, and Sara, who I've lived with for the entirety of the time I've dedicated to this work. I can't imagine having the drive to continue without you all giving me such an incredible home to come back to every single day.

To both my employers and my friends, Ken and Sandy, who have kept me working nearly every weekend (and even some weekday nights) for the entirety of my studies. Working on your farm was the change of pace I needed to keep me focused in the lab, and I wouldn't trade the things I have learned with you or the wonderful memories I have made for anything.

To my best friend, Patrick, who always gave me something to look forward to whether it was our next fishing trip or our next game night. Even though I never had much free time, I wouldn't have wanted to spend it on anything else.

Finally, to my Rosie, who has been a constant source of inspiration and motivation for me. She has been so patient living an ocean away from me, and I can't wait to see what life has in store for us as we are finally able to move forward together.

Contents

List of Figures

Chapter 1

Introduction

1.1 The Evolution of Infrared Spectroscopy

This work discusses the implementation of a segmented gas cell based on optical fiber, which was used in an Intra Cavity Laser Absorption Spectroscopic (ICLAS) System. An ICLAS system is a highly sensitive spectroscopic system, which makes use of the radiation in a laser cavity. The infrared spectrum of light has been known since 1800 with observations made by William Herschel [1]. He was able to detect a source of heat beyond the red line in the visible spectrum. The road to its use as an analytical technique for identifying compounds however was a long one. To begin this journey one must discuss the precursor to absorption spectroscopy in general, namely emission spectroscopy, which originated in 1822 with William Herschel's son, John Herschel. John Herschel noted that compounds burned with different colours, and as such one could use the colour of the flame to identify the compound even if only a minute amount of it was present [2]. This procedure was expanded upon and developed into something we would recognize as analytical spectroscopy by Gustav Kirchhoff and Robert Bunsen in 1855 during their study of the spectrum of sodium [3]. By constructing a spectroscope and observing the refracted light of burning sodium they showed the distinct bands of yellow light that are produced. Later, Kirchhoff noted that the wavelength of light that

was observed to be emitted during their experiments was consistent with the Fraunhofer 'D' line in the spectrum of sunlight. This was a realization that not only do elements give off energy at particular wavelengths, but they must absorb them too.

Both observing and acknowledging the importance of absorption in the visible spectrum is in and of itself a great achievement, however it wasn't until 1880 when William Abney, through use of photographic plates, analytically detected and logged the infrared spectra coming from the solar system out to a wavelength of 10000 nm, well into the IR region [4]. Even forty years later the methods employed by Frederick Brackett only revealed a few more absorption lines in the same region studied by Abney [5]. This was far beyond anything William Herschel was capable of doing in 1800 and a great step forward in the field of absorption spectroscopy. However beyond the academic success there was no commercialization efforts, even after Abney showed that the infrared region contains information characteristic to the structure of the molecule under investigation [6]. When one examines their experimental setup, it becomes more obvious why this was the case. The light source employed in their experiments was run off of a three-horsepower engine (the performance of which they "can not speak too highly"). Their sample containers were tubes of glass which varied between two feet to three inches in length. Additionally they had to have a custom-built camera and a spectrometer which consisted of an elegant design of three to five prisms depending on the measurement taken. All of these components needed to be carefully aligned, and it required specialized knowledge of the system to collect and interpret the data which was developed on photographic plates which had a scale etched onto them at ¼ millimetre intervals. While the fundamental technology they were using would be considered 'simple' by today's

standards, it was by no means user friendly. Compounding this issue was the fact that it could take hours of exposure to adequately expose the photographic plates used for collection of the spectra, and the system would need to be kept stable throughout this period.

Even as these incredible advances in spectroscopy were taking place in the academic space, there were significant technological limitations which prevented spectroscopy in any of its forms from entering the market. The colour comparator, developed in 1885 by Joseph Lovibond, was one of the first commercial machines introduced to make measurements in the visible spectrum which made use of the most fundamental detector available at the time, the human eye [7]. The inherent problem with using the human eye, however, is that it is difficult to calibrate, and the results can vary from operator to operator. While this method was more qualitative than quantitative it was the beginning of a long and still developing path which would explore how observing light's interaction with matter could tell us so many details about it.

During the intervening years absorption and emission spectroscopy were investigated across the spectrum, but it was not at the point of becoming commercially viable as a quantitative system. Great advancements were made in the theory surrounding the phenomena, most significantly the calculations of Niels Bohr in 1913 [8]. Bohr was responsible for connecting spectral lines to the new era of quantum mechanics. His work linked the electron's transition from one energy state to another which results in the emission or absorption of a photon at a very particular wavelength (quantized energy) [9]. Because the energy states of atoms are quantized the energies of emitted photons are

discreet, which explains why absorption and emission lines are typically seen as sharp peaks.

Finally, in 1945, technology caught up to the concept of absorption spectroscopy. The Perkin-Elmer corporation developed the first commercially available infrared spectroscopy system, the Model 12A [10]. The authors of the review article noted the 'light weight' design of 100 pounds, and its 'compact size' of 31x12x9 inches which was true for the time. The light source was a 'Globar' with an average lifetime of only six weeks, and the method of discriminating lines was once again a prism system housed within the detector and a series of mirrors which would focus the radiation to a thermocouple. The current generated by the thermocouple is then measured by a galvanometer system. It was through use of this machine that infrared spectroscopy was finally able to enter the market as a means of fingerprinting compounds based on their characteristic absorption peaks.

Perhaps one of the most influential researchers in terms of making infrared spectroscopy recognized as an analytical tool was Alan Walsh, who not only developed a lamp which produced a narrow pulsed spectral line which improved upon previously available sources, but also improved upon the design of the Perkin-Elmer spectrometer in order to increase the possible resolution of the machine, and as a result obtained some of the best infrared absorption spectra [11]. The methods Walsh used in his experiments are to some degree still used today, albeit with modernized sources and detectors. Once the idea of absorption spectroscopy as an analytical tool took hold it was up to the march of technological progress to determine its limitations. As lasers began to come into prominence the potential for high-quality narrow band sources in a wide array of

wavelengths was a significant boon to the field. Being able to interrogate specific wavelengths allowed for the development of specialized systems.

Today, by way of utilizing modern technology, the resolution of individual absorption lines (and even the fine structure within those lines) can be observed for extremely low (trace) gas concentrations and a relatively weak absorption interaction with light. In today's market there are endless applications for trace gas detection, be it in an industrial setting to detect contaminants [12], in a medical setting to detect compounds in breath which may be indicative of a health problem [13], in an environmental setting to detect contaminants or changes in the atmosphere [14], and in an agricultural setting to detect emissions from fertilizer [15]. Three techniques will be discussed and compared to the system, which was designed for this work, the first of which is the simplest, and the one which is most intuitive: Direct Absorption Spectroscopy (DAS). DAS requires that light simply passes from the light source, through the sample once, and then to the detector. While the principle is quite simple, the physics behind what is happening as the light and sample interact is quite complex, and will be examined in later sections. What is important to understand at this stage is that a DAS setup works quite well when the interaction length between the light and the sample is quite large, or the concentration of the sample is quite high. If these parameters are reduced, the effectiveness of DAS suffers, and an alternative technique may have to be used to achieve the required sensitivity [16].

The next technique to be introduced is Cavity Ring-Down Spectroscopy (CRDS). A conventional CRDS involves measuring the decay time of the laser pulse injected into a high finesse cavity (Fabry-Perot or ring configuration) that contains the gas sample,

where the rate of decay of the pulse indicates the absorption by the gas [17]. This method is significantly more involved than DAS. If the pulse is introduced into an empty cavity, the decay would only be dependant on the loss due to its interaction with the cavity components (e.g., reflectors in a linear cavity setup). However, when an absorbing sample is introduced the rate of laser pulse decay will have an additional factor introduced due to the pulse's interaction with the sample. By comparing these two decay rates, information about the sample's concentration can be deduced. Because the decay rate is being observed rather than the actual intensity, the system isn't affected by small fluctuations in laser stability, which improves its sensitivity. Additionally, because the light is being circulated within a high finesse cavity, the relative path length of interaction with the sample increases dramatically. Recall that one limiting factor of DAS is that it required a very long path to be effective at lower concentrations; CRDS can achieve an effectively long path length with a relatively small physical cavity. The downside of this system is that, as mentioned, it requires an extremely low loss cavity. A CRDS system based on Continuous Wave (CW) laser has been developed where a monochromatic source is tuned to a particular absorption line [18].

Finally, Intra Cavity Absorption Spectroscopy (ICAS) will be described. ICAS is the technique which most closely resembles the system in this work. Just as with CRDS, the effective path length of the sample is dramatically increased in ICAS, however unlike CRDS this is not due to a pulse being introduced into a high finesse cavity, but because the sample itself is contained within the resonant cavity of a laser [19]. In ICAS, the gas cell is used inside a laser cavity and thus no external laser is required, which is an important distinction from CRDS. Further, in a CRDS system a high finesse cavity is

required, but in the case of ICAS the cavity loss is not as important as the gas sample is inside the laser cavity, and the gain in the cavity compensates any losses. Details concerning what the laser cavity is and how it is integrated into the system will be discussed in Section 1.2. The ICAS technique was adopted and modified to work within the system described throughout this work due to the fact that it provided the ability to introduce a small form all fiber gas cell which would have a loss too high for CRDS. [20]. The system can be utilized for several different gas species by choosing a gain medium with wide bandwidth, which coincides with absorption lines.

1.2 Optical Fiber and Fiber Based Systems

Typical optical fibers are concentric cylindrical dielectric waveguides (the 'core' is contained within the 'cladding'), which propagate light at varying degrees of attenuation depending on the material. The mass-produced silica optical fibers which we are familiar with today were developed by Bell Labs in 1973, where they were able to produce extremely low loss optical fiber via a vapour deposition method [21]. Optical fibers have played in incredibly important role in the advancement of the telecommunications industry, allowing data to be sent securely at an incredibly high speed worldwide. They are not only limited to telecommunications, however, and find a niche in medical imaging and sensing, while also being used for both decoration and illumination. Most relevant to this work is the application of speciality optical fibers in spectroscopy (e.g., Hollow-Core Photonics Crystal Fiber- HC-PCF), and the ability for fibers to act as amplifiers when doped with particular rare earth elements (e.g., Erbium-doped fiber).
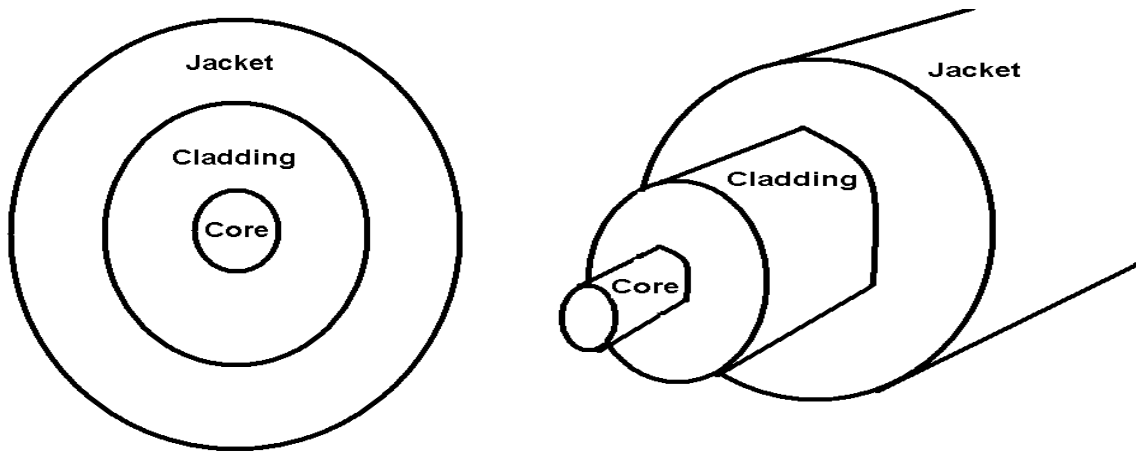
Figure 1.1: On the left is a front facing view of a fiber optic strand, on the right is a skewed cut-out view. Each diagram has the concentric cylinders which make up the fiber, namely the core, cladding, and protective jacket layer.

Generally speaking, one can consider the propagation of light within an optical fiber under two different approaches. The first of which is the relatively simple ray optics approach, which is valid when the diameter of the fiber is large compared to the wavelength of light being propagated. This approach however has its limitations, and it is often necessary to describe in detail the properties of the optical fiber by introducing the concept of modes or modal analysis [22].

In the ray optics approach, one can consider the classic example of a fiber optic strand; a cylindrical dielectric constructed out of fused silica, with a 'core' refractive index (n_1) slightly larger than the cladding refractive index (n_2), known as a step index fiber. Snell's law dictates that when light is incident (Θ) at the core-cladding interface at an angle

greater than the critical angle (Θ_{crit} = arcsin(n_2/n_1)), it will be confined within the fiber due to total internal reflection [23]. Figure 1.2 illustrates the ray optics representation of light propagating through fiber, note that any ray within the cone angle will propagate through the fiber due to multiple total internal reflections at the core-cladding interface.
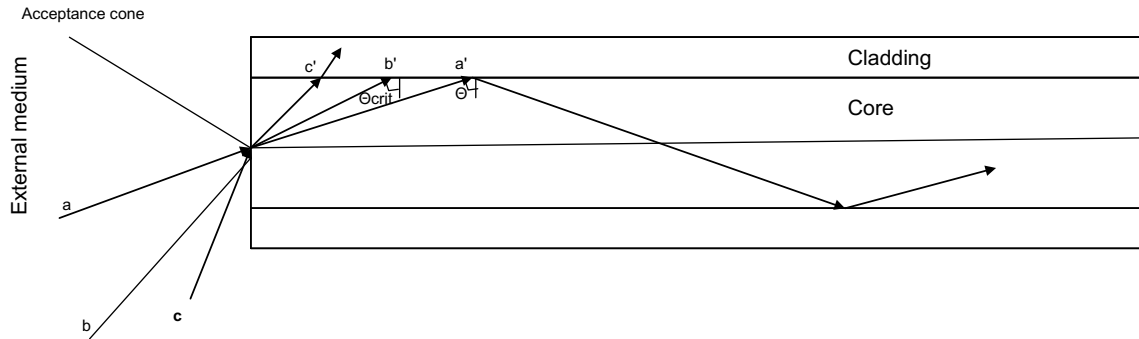
Figure 1.2: Schematic of an optical fiber with the acceptance cone shown on the left (including ray 'b'). Ray a is an incident ray within the acceptance cone striking the core-cladding interface and angle φ_{crit}, ray b is a ray at the critical angle which is incident along the edge of the acceptance cone, striking the core-cladding interface at angle φ_{crit} , ray c enters the fiber outside of the acceptance cone and is refracted into the cladding.

The numerical aperture (NA) of a fiber can be obtained using Snell's law:

$$NA = \sqrt{n_1^2 - n_2^2} \qquad (1.1)$$

The concept by which rays are propagated through the fiber, however, is more complex than whether or not a ray is simply within the acceptance cone. One must also consider the fact that light is coupled into the fiber in a discreet set of modes, where a mode is a

9

way in which the electromagnetic radiation may propagate through the fiber; it can be thought of as a particular distribution of the electromagnetic field within the core/cladding. One could consider rays entering the fiber at different angles being coupled into different propagation modes, however this is where the ray optics approximation begins to break down, and a more detailed and fundamental definition is required to explain the propagation of light in modes through the fiber [22].

In order to more completely understand these concepts, one must solve Maxwell's equations for optical fiber. One important parameter is the propagation constant β which describes how light in a particular mode will propagate in the medium:

$$\beta = k = 2\pi/\lambda = 2\pi n_1/\lambda_0 \qquad (1.2)$$

where k is the axial wavevector component and λ_0 is the wavelength of light in vacuum. The light propagation follows the following condition:

$$n_2 k \leq \beta \leq n_1 k \qquad (1.3)$$

If the propagation constant of a particular mode is less than $n_2 k_0$ then it will be a 'leaky' mode (i.e. it will not be completely contained within the core and will be significantly attenuated).

Another important parameter to consider is the 'V' parameter, which is indicative of the number of modes supported by a particular fiber:

$$V = \frac{2\pi a}{\lambda} NA \qquad (1.4)$$

where a is the radius of the core. The V parameter relates to the number of supported modes by the following relationship:

$$M = \frac{V^2}{2} \qquad (1.5)$$

Cut-off condition is met when the V parameter is less than 2.405 and under this condition the fiber supports only fundamental mode, and the fiber is known as a single-mode fiber (SMF), when the V parameter is larger than 2.405 the fiber can supports many modes, and as such it is known as multi-mode fiber (MMF).

Up until this point the discussion has centered on classic optical fibers, made of fused silica and operating under the principles of total internal reflection. There is another type of optical fiber, known as photonic crystal fiber (PCF) which also couples and propagates electromagnetic radiation. However, PCF couples light by a completely separate mechanism. PCF was developed in the mid 1990s by the P. Russel group [24] who demonstrated that an optical fiber could be constructed with a pattern of hollow tubes (creating a photonic crystal) in the traditional cladding region of the fiber. A photonic crystal is a highly ordered macroporous material which may confine and control the propagation of light through the photonic band gap (PBG) effect under specific conditions [25;26]. Solid core PCF shares a common trait with traditional fiber in that the confinement of light is mostly controlled by total internal reflection due to the small

11

difference in the refractive index of the core, and the effective refractive index of the photonic crystal cladding. HC-PCF, however, confines the light to the core by a process known as the photonic band gap. The photonic band gap essentially stops the propagation of light of a particular wavelength in a particular direction forcing it to remain confined to the core by a system of diffraction and scattering events within the crystal structure [27]. Figure 1.3 shows a schematic of PCF. The dark circles in the schematic represent the hollow portions of the fiber, while for HC-PCF the center region would also be hollow. When light transitions between two mediums with different refractive indices it is partially reflected; this leads to both forward and backward propagating light. In HC-PCF the light is transitioning between the hollow core and the silica structure, and the silica structure and the hollow tubes making up the cladding. Each time light transitions between silicon and air there is a partial reflection of the signal, it is the sum of these partial reflections which create a backward propagating wave. These forward and backward propagating waves interfere, forming a standing wave for wavelengths fulfilling the Bragg condition depending on the structure and composition of the material causing the partial reflection. By modifying the structure of the HC-PCF, one can control the 'band gap'; in other words one can control which wavelengths fulfill the Bragg condition and are excluded from the cladding and confined to the core [28;29]. This process is not dissimilar to how Fiber Bragg Gratings (FBGs) operate, however the dimensionality of the problem is higher in the case of HC-PCF. The crystal structure of the cladding is where PCF gets its name, and is typically constructed out of silica, similar to the classical fibers previously discussed; the major difference comes from the method of signal confinement. PCF has found uses in a wide variety of fields, from fluorescence

microscopy [30], creating oscillators and amplifiers [31;32], metrology [33;34], and optical coherence tomography [35;36].
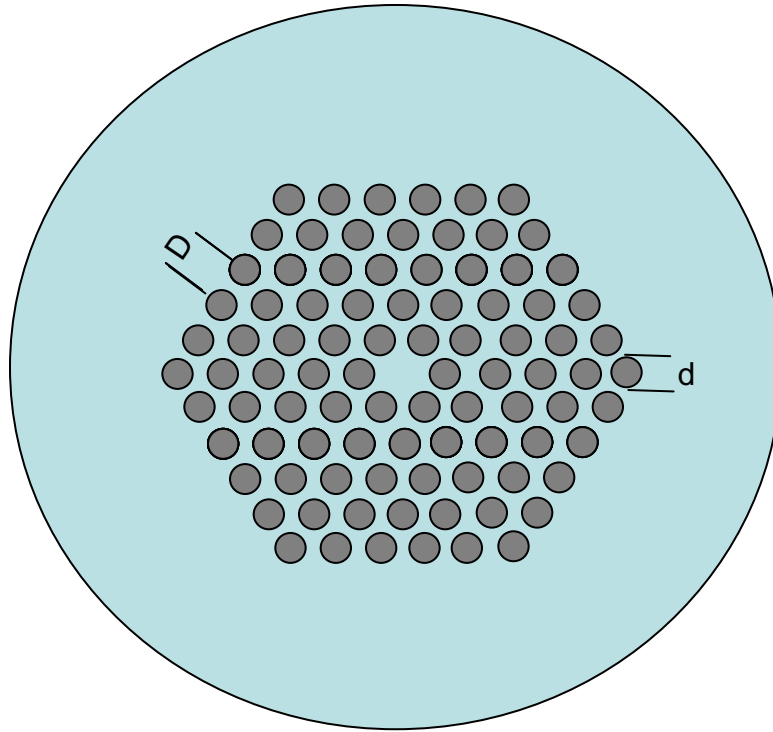
Figure 1.3: Hexagonally patterned PCF, where the small solid grey circles are hollow tubes extending into the fiber, the solid blue background is silica, D is the separation between the hollow tubes, and d is the diameter of the hollow tube.

The archetypal form of PCF can be seen in Figure 1.3, with a hexagonal pattern of hollow tubes separated by a distance D, and having diameter 'd'. The light is confined and propagated within the central region of the fiber (which in the case of solid core PCF is typically made of silica) primarily due to the effective refractive index of the periodic air-silica pattern which is analogous to the cladding region of a typical optical fiber.

One major advantage of PCF is that the hole separation and diameter can be tuned to affect the properties of the fiber, such as the dispersion. In the telecommunications industry, dispersion shifted fiber (Zero dispersion at 1550 nm) was designed by modifying the core refractive index distribution. PCF however can achieve minimum dispersion at any desired wavelength including the visible region by modifying its aforementioned parameters, opening up the possibility for a wide variety of all-fiber laser applications which would not be feasible with traditional fiber [37].

When the V parameter is calculated for PCF, the cladding refractive index is replaced by the effective refractive index of the air-silica micro-pattern (the photonic crystal).

$$V = \frac{2\pi a}{\lambda} \sqrt{n_c^2 - n_{pc}^2} \qquad (1.6)$$

Where n_c is the refractive index of the solid core and n_{pc} is the effective refractive index of the photonic crystal lattice (effectively the cladding).

Interestingly, this effective refractive index is heavily dependant on the wavelength (much more so than when one considers the wavelength dependence of a traditional material such as silica) along with the aforementioned PCF parameters D and d which is calculated via a vectorial approach rather than a numerical model by Zhu et al. [38] where they perform this vectorial method by defining a modal magnetic field which has both a transverse and longitudinal (z) component. This modal field is then substituted into the wave equation where the transverse component of the magnetic field is found to be expressed in terms of both the x and y component of the field. In order to decouple the x and y components, a complex calculation done through redefining both the dielectric

constant profile (which is a function of x and y as well) along with the transverse component of the field in reciprocal space, which reduces the system down to an eigenvalue problem. The results of Zhu et al. indicate that shorter wavelengths of light will raise the effective refractive index of the photonic crystal, thus decreasing the V parameter. Additionally, the ratio of the wavelength to the hollow tube spacing (D) as well as the ratio of the diameter of the hollow tubes (d) and D are both inversely proportional to the refractive index. In general, the V parameter is inversely proportional to the wavelength of light, which means that in traditional fibers lower wavelength would result in a larger V parameter, taking it over the cut-off condition and resulting in multi-mode propagation. However, in PCF, these two competing wavelength dependencies result in PCF being capable of sustaining single-mode propagation at much lower wavelengths than traditional fiber.

As the discussion has surrounded the traditional PCF case where the core has a larger refractive index than the effective index of the photonic crystal, the method of propagation was similar to that of traditional fiber, namely total internal reflection. However, in HC-PCF (Figure 1.4) total internal reflection cannot occur [39-42]. The light propagates following the photonic band gap process [43]. Essentially, the photonic crystal structure operates by Bragg reflection, in which for some particular wavelength (and wavevector (**k**)) the cladding acts as a two dimensional photonic crystal, and allows propagation only for a limited number of wavelengths (dependant on the HC-PCF design) within fairly narrow 'band gaps' (when β<k) [41]. For other values of β where one would expect to find propagating modes, one instead finds 'gaps'. The number of allowed modes is limited which means there is a very limited range of wavelengths which can be

confined within the hollow core. While this may at first come across as a limitation, the fact that the zero-dispersion point can be so conveniently shifted by manufacturing a PCF with a modified crystal structure makes up for the smaller window in which light may propagate through the fiber. PCF, as previously stated, may operate across an incredible range of wavelength ranges which fall significantly outside the operational range of traditional optical fiber.

HC-PCF has several interesting characteristics, namely it has the ability to deliver extremely high power due to the fact that the light propagates within an air core as opposed to a silica core [40]. Additionally HC-PCF could potentially reach transmission losses lower than that of traditional fiber (air has a significantly lower transmission loss than silica), however there is still much ground to cover as optical fiber has been on the market facing many rounds of optimization which has brought its transmission loss down to 0.15 dB/km (near the theoretical limit) whereas PCF is relatively new, and as such there is a lot left to optimize in its manufacturing and design process [41]. One research group has shown that HC-PCF could potentially reach a transmission loss of 0.1 dB/km , and have concretely shown a current loss of 1.2 dB/km [44]. More specific to this work HC-PCF allows gas/liquid to enter the fiber and act as the propagating medium, which allows for the conception of novel gas sensors such as the system developed previously by other members of the Photonics Research Group at Lakehead University [39;45;46]. The previous work based on HC-PCF done within our research group was impressive in that it was able to detect sub ppm concentrations within the traditional telecommunications band, however it required several hours of evacuation/filling time in order to empty/fill the fiber with gas sample. As such this technique was limited to

16

measurements which required a very low temporal resolution. The main focus of this research was to address this problem by developing a new gas cell based on HC-PCF, as will be discussed in future sections, and allow it to operate at a much higher frequency.

SU70 10.0kV 16.2mm x1.00k SE(M)   50.0um
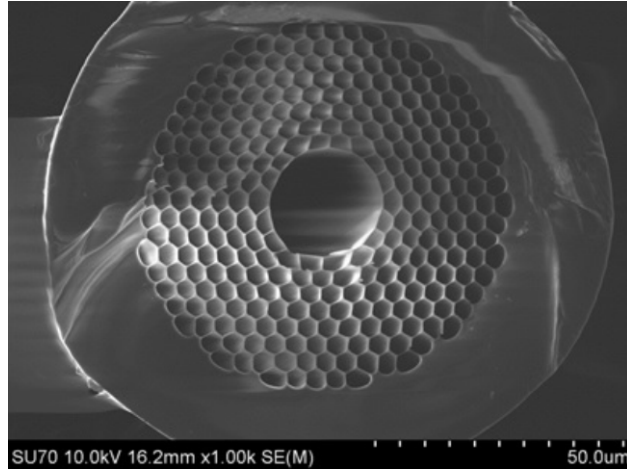
Figure 1.4: A SEM image of the HC-PCF used in this work, note the honeycomb structure similar to the schematic for PCF shown in Figure 1.3.

It should be noted that HC-PCF is not the only possibility when it comes to the design of a fiber which operates via the photonic band gap mechanism. Further, one could also dope a solid silica core with rare-earth elements in order to lower the refractive index of the core, and as such be in a situation where once again total internal reflection is no longer possible and the photonic band gap dominates the confinement and propagation of light. Such fibers have shown promise in the design of new fiber lasers and amplifiers due to their ability to contain rare earth ions as a dopant, and thus have the ability to operate as a gain medium or saturable absorber [47;48]. The photonic crystal structure of the cladding is typically required in these setups; however work has been done to even

remove these air pockets by replacing them with doped silica rods while still confining light by the photonic band gap effect [49].

One of the main objectives of this research is to develop a low cost and compact spectroscopic device, and one of the main ways of accomplishing this is to utilize an all fiber design and operate in the telecommunications band (1550 nm). Optical components designed to operate in this band tend to be cheap and relatively easy to procure as they are mass produced in order to satisfy the vast and ever - expanding telecom industry. Classic silica based optical fiber, as discussed in the previous section, operates optimally in the 1550 nm band, additionally HC-PCF can be tuned through manipulating the crystal lattice structure, as previously discussed, in order to operate in this region as well.

Another significant component of this research work involves developing a laser in a ring cavity configuration, which incorporates an Erbium-doped fiber as the gain medium. The doped fiber produces Amplified Spontaneous Emission (ASE) light when pumped with a 980 nm pigtailed diode laser (150 mW). The developed gas cell was inserted inside the laser cavity, resulting in an Intra Cavity Laser Absorption Spectroscopy (ICLAS) system, which imprints the absorption spectra of the gas sample upon the ASE spectra.

In the traditional view, an all-fiber laser would resemble a linear cavity (Figure 1.5) in which two reflectors (Fiber Bragg Gratings, or 'FBGs') reflect spontaneously emitted photons through the gain medium (Erbium Doped Fiber: EDF). These multiple reflections result in stimulated emission of photons. In the case of EDF pumped at 980 nm, the erbium ions are excited to the pump band ($^4I_{11/2}$), from which the ions relax to a metastable state ($^4I_{13/2}$) via a non radiative process [50]. The pump band ions decay

extremely quickly (within approximately 7 micro seconds) compared to the metastable state ions which can last on the order of milliseconds [51]. Once the metastable state ions decay back to the ground state, a photon is emitted with energy corresponding to a 1550 nm wavelength [52]. When trying to induce lasing action one is typically interested in the stimulated emission of photons, which dominate over the spontaneously emitted photons. Many of the spontaneously emitted photons will also be confined within the cavity, and will then stimulate the emission of congruent photons thus building the power of that wavelength.

Gain medium (doped fiber)

Fiber Bragg Gratings
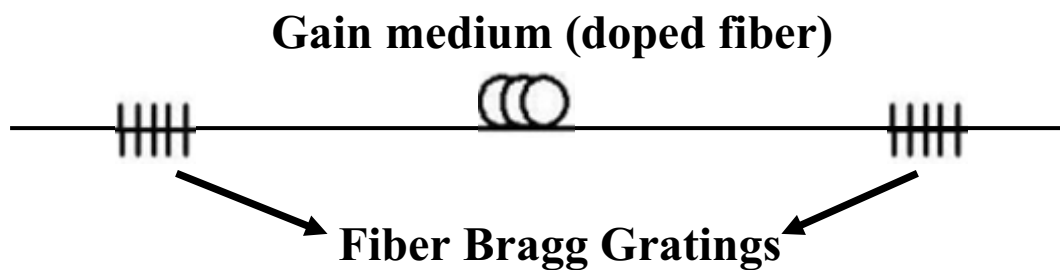
Figure 1.5: Linear cavity configuration of a fiber laser cavity consisting of two fiber Bragg grating reflectors and a central gain medium.

The alternative to a linear cavity configuration is the ring cavity, where ASE light propagates unidirectionally through the gain medium. Figure 1.6 shows a ring cavity, where a WDM coupler was used to couple the pump laser, and an optical isolator to force the ASE spectra produced in the gain medium to propagate in the clockwise direction. The resonance condition in the cavity decides the emitted laser wavelength. Output of the laser was monitored using an Optical Spectrum Analyzer (OSA).
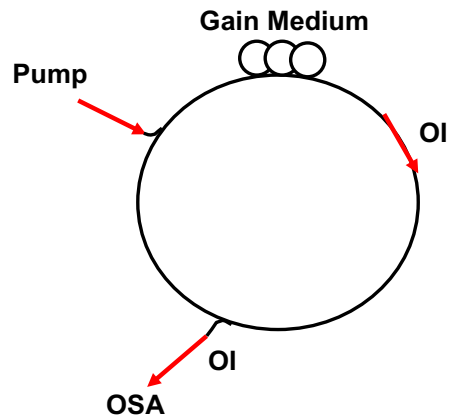
Figure 1.6: Ring cavity configuration of a fiber laser cavity consisting of an optical isolator to ensure unidirectional propagation, a gain medium, a pump source coupled into the ring, and a fused fiber coupler which allows one to obtain a fraction of the power from the cavity, analyzed by an Optical Spectrum Analyzer (OSA).

Usually, the ASE (Figure 1.7) is considered to be a detriment to the system, as a stable laser beam is what is required in most applications. However, in the case of gas spectroscopy, one can take advantage of the ASE by making use of its broad wavelength coverage to sample multiple absorption lines. When using a single laser beam one can only view the effects of an absorption line at that wavelength, however when there is a broad range of wavelengths circulating through the gas cell (GC) an imprint is formed across the whole 'field of view' [53]. The wavelength range and power contained within the ASE depend chiefly on the dopant used and the structure of the silica it is embedded in.
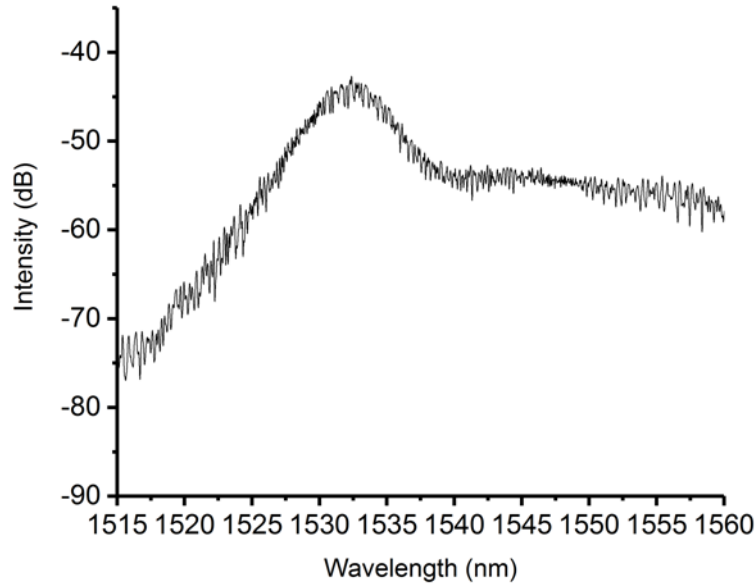
Figure 1.7: ASE spectra produced by the erbium doped fiber pumped by a 980 nm laser in a ring cavity configuration.

An important component to the linear cavity configuration which is notably absent from the ring cavity is the FBG. In the case of a typical ring cavity a FBG is not required, as the light propagating within the fiber simply loops through the gain medium without the need for reflection, and the resonance condition of the cavity determines the emitted wavelength.

An FBG is a small all fiber reflector which can be designed with a high degree of sensitivity and with very low loss outside of the intended reflection band [54]. It has found use in many sensing applications, from the detection of humidity, temperature, and even strain [55-57]. The first FBG was developed in 1978 by Ken Hill et al. [58], however the first modern FBG, constructed by exposing the fiber to ultraviolet light at

periodic intervals, was developed in 1989 by Gerald Meltz et al. [59]. As the name suggests, FBGs function based on a 'grating' of periodic refractive indices which was developed by exposing a portion of the core to UV light (Figure 1.8). The periodicity of the refractive index is tuned depending on the wavelength of light which is required to be maximally reflected. As a general rule the grating spacing should be approximately half of the desired wavelength (Bragg wavelength) to be reflected, which is known as the Bragg condition.

$$\lambda_{Bragg} = 2n_1\Lambda \qquad\qquad (1.7)$$

A major benefit of FBGs is that it allows for the efficient filtering of a particular signal. As is evident from the above equation, the Bragg wavelength is dependant on the refractive index of the core, as such any external parameters which would affect the refractive index will affect the reflected wavelength; this is the principle of how FBGs can function as a sensor. As the Bragg wavelength shifts, the percentage of light which it reflects and transmits will also change. For example, by actively monitoring either end of the FBG one can model how temperature or strain affects its performance [60].
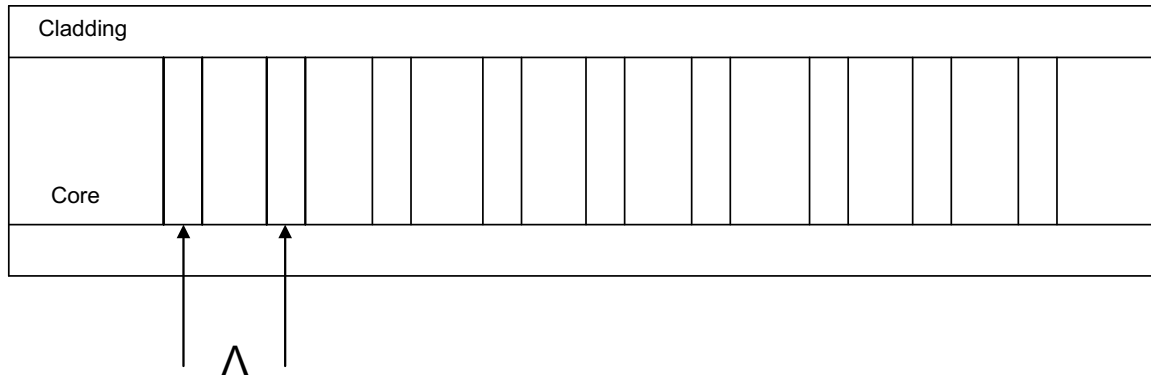
Figure 1.8: Schematic of a FBG where Λ is the grating spacing

Beyond the traditional FBG which has been discussed, variants exist which fulfill particular niche requirements such as: chirped, tilted, and sampled FBGs. Chirped FBGs have a varying periodic separation, which results in a broader reflection band than a traditional FBG (up to tens of nanometres) [61]. Tilted FBG have a 'tilt' in the periodic structure of the grating, rather than being perfectly perpendicular to the core axis they are tilted by some angle. This tilt results in many reflected wavelengths in the counter-propagating cladding modes. The unique structure of tilted FBGs allows for the simultaneous measure of temperature and strain [62]. Finally, sampled FBGs have a periodic grating period. The periodic structure has gaps in it, and by tuning these gaps one can effectively create the effect of chirped or phase shifted gratings [63].

The next fiber - based component to be discussed is the saturable absorber (SA). Generally speaking, a SA is an intensity dependent attenuator constructed from an unpumped rare-earth doped fiber. In the current research work an erbium-doped fiber was used as the saturable absorber (SA) to stabilize the laser wavelength [64]. It is reasonable to think of the SA as being constructed of absorbing ions scattered throughout. As these ions absorb the incoming radiation they are elevated to an excited state, and as more ions

are elevated there are fewer ions available to absorb the remainder of the incoming radiation. The net effect of this is that at higher intensities the SA will 'saturate' and it will become transparent.

Excited State

ΔE

Incoming Photon With
Matching Energy
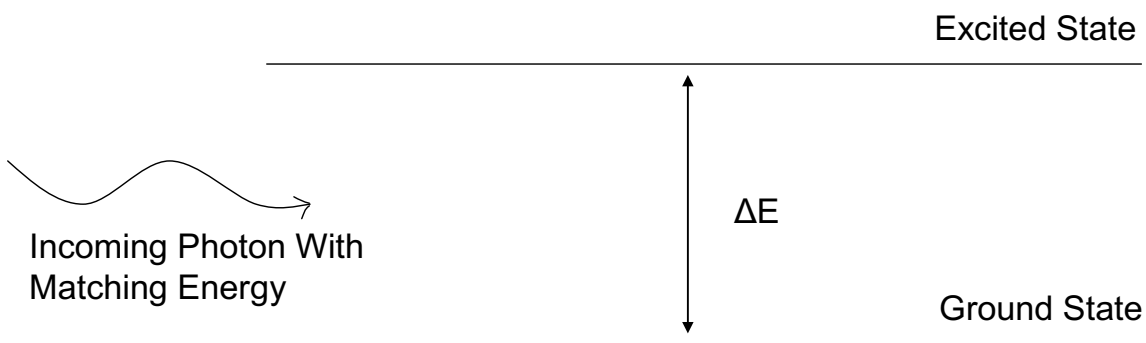
Ground State

Figure 1.9: Pictographic representation of a photon stimulating an absorption transition between an arbitrary ground and excited state.

As has been suggested in the introductory statements of this work, transitions between energy levels for a particular molecule correspond to quantized energy levels, in other words:

$$\Delta E = hc/\lambda \qquad (1.8)$$

Where c is the speed of light, lambda is the wavelength, and h is Plank's constant. Describing the situation pictographically, refer to Figure 1.9 which shows an incoming photon which matches the energy separation between two states of an arbitrary molecule which can result in the absorption of the photon, increasing its energy level.

In general, when a molecule is exposed to a particular wavelength of light, the absorption is dictated by the Beer-Lambert Law:

$$I(\lambda) = I_0(\lambda)e^{-\alpha(\lambda)CL} \hspace{2cm} 1.9$$

Where I_0 is the incident intensity of light at a particular wavelength λ, I is the intensity of the light after absorption, α is the absorption coefficient for a particular wavelength (also known as the absorption cross section), C is the concentration of the sample, and L is the path length along which the light is interacting with the sample. In practice this can be visualized in Figure 1.10.

Gas Cell

Incident Radiation → Concentration: C / Absorption coefficient: α / Length: L → Output

I_0

I
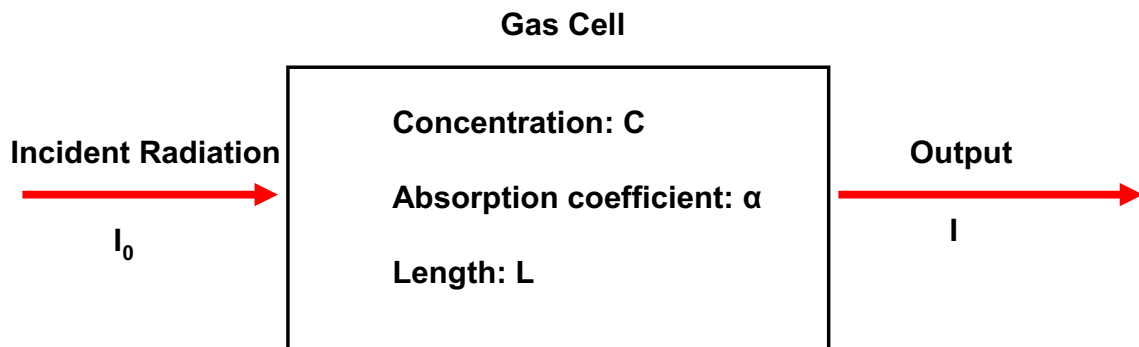
Beer-Lambert's Law: $\dfrac{I}{I_0} = exp(-\alpha CL)$

Figure 1.10: Beer Lambert law with the variables visualized, α is the coefficient of absorption for the particular sample under investigation.

The simplest way to observe absorption spectra is via Direct Absorption Spectroscopy (DAS) [16]. The meaning of direct in this case is that the light enters one end of the gas cell, travels a particular path length L, and the output enters the OSA where the absorption lines are visible. While this method is practical for high concentrations of gas, or gas which has a particularly strong absorption coefficient at the measured wavelength, anything outside of this regime would require a long path length to be practical. This wouldn't be an issue if the data to be taken could be in an open-air setting with a laser simply passing through the atmosphere to a detector some hundred(s) of meters away, however in a laboratory or industrial setting this simply isn't practical for the species of gas under investigation and for the space requirements. Gas cells have been developed with a long effective path length, such as the Herriot cell, which has a multi-pass design allowing for the laser to make multiple reflections through the length of the cell thanks to the precise alignment of mirrors on either end of the cell [65]. This solution however remains limited, as even a thirty - meter path length Herriot cell will cost tens of thousand dollars, and is not scalable once purchased. Another solution, known as Intra Cavity Absorption Spectroscopy (ICAS), includes a gas cell within the laser cavity itself [66]. This means that as the laser resonates within the cavity the absorption lines of the gas sample are imprinted upon the spectra each time the light passes through it. This results in an 'effective' path length which can be much longer than the original physical path length included in the system.

Chapter 2 will describe the fundamentals of laser spectroscopy and spectroscopic data. It will go into the detail of where a characteristic absorption spectrum comes from and the mathematics behind calculating the expected absorption spectra. Chapter 3 will cover

the process of developing the gas cell using HC-PCF and its components, as well as the experimental results based on acetylene gas. Finally, Chapter 4 will cover the application of the developed system and future works.

This work details the development of a unique gas cell based on hollow core photonic crystal fiber (HC-PCF) improving its ability to be used in measurements which require higher temporal resolution. This new gas cell was incorporated into an ICAS system. Benefits of this new gas cell include the ability to create a true all-fiber gas sensor due to the fact that the input and output of the HC-PCF, which would normally have to remain unobstructed to allow gas to enter the fiber, can now be coupled directly to the fiber laser system, removing the need for three axis micrometer stages to align the input and output through quartz windows in the containing cell. This benefit is only possible by allowing gas to penetrate the HC-PCF through some other means than the ends of the fiber, this was done by systematically segmenting the fiber. This system will be significantly compact and cost effective due to its all - fiber design and operation in the telecom band respectively. Additionally, the absorption lines examined over the course of this work were off resonance with the laser line produced by the system, showcasing it's flexibility when detecting gasses outside of the Bragg wavelength.

Chapter 2

Molecular Spectra of Acetylene (C_2H_2) using HITRAN (High-resolution Transmission Molecular Absorption) Database and Ro-Vibrational Spectroscopy

2.1 The HITRAN Database

The concepts discussed in the previous chapter regarding absorption spectroscopy of a particular gas sample works to give a general idea of the magnitude of absorption at a particular wavelength, it does not give information about the 'shape' of the absorption line. In order to understand what is meant by this it is necessary to go through the process for calculating the absorption coefficient, by using the HITRAN (High-resolution Transmission Molecular Absorption) database. HITRAN compiles and references spectral data for many molecules and allows one to query and receive tabulated data with a custom output for a chosen range of wavelengths. By taking this tabulated raw data, one can then calculate the line shape function by [67]:

$$f_L(\nu;\nu_{ij},T,p) = \frac{\gamma(p,T)}{\pi\gamma(p,T)^2 + [\nu - (\nu_{ij} + \delta(p_{ref})p)]^2} \quad (2.1)$$

Where f_L is the normalized line shape function which describes the 'shape' of the absorption coefficient in terms of a Lorentz profile across the spectrum. The Lorentz

profile is assumed when dealing with gas at atmospheric pressure, as collision broadening is the dominant force; the alternative Doppler-broadening regime is dominant at low pressure however it is not considered here due to the terrestrial nature of our experiments [68]. p is the pressure of the gas, ν is the wavenumber of the laser line or the absorption line, ν_{ij} is the wavenumber of a spectral line (in vacuum) denoted by its subscript. This subscript denotes the transition energy levels i and j where j is the upper state energy and i is the lower state energy (as such, the photon absorbed will be of energy $\Delta E = E_i - E_j = hc\nu_{ij}$), $\delta(p_{ref})$ is the pressure shift, and γ (p, T) is the pressure-broadened half width half maximum for a gas at pressure p and temperature T, and is itself the result of the following equation:

$$\gamma(p,T) = (\frac{T_{ref}}{T})^{n_{air}} (\gamma_{air}(p_{ref},T_{ref})(p - p_{self}) + \gamma_{self}(p_{ref},T_{ref})p_{self}) \quad (2.2)$$

This pressure-broadening function is the result of both the pressure broadening due to the air (γ_{air}) at standard pressure and temperature (p_{ref} and T_{ref} are 1 atm and 296 K, respectively) and itself (γ_{self}) where p_{self} is the partial pressure of the gas. $\delta(p_{ref})$ is the pressure shift with respect to spectral line ν_{ij}. Finally, n_{air} is the coefficient of the temperature dependence of the pressure broadening due to air. The parameters described in this paragraph are directly measured by researchers and collected in HITRAN for easy access, the work done by Devi et al. is an example of such a measurement [69]. Devi et al. utilized a Fourier transform spectrometer to measure the parameters of water vapour in the ν_1 and ν_3 vibration band by taking measurements at three temperatures (268, 296, and 353 K) for both a pure water vapour sample, as well as water – air mixture. There were

18 samples, each of which was prepared with a different gas pressure and in the case of the air – water mixture, a different volume mixing ratio of air and water. Measurements of the pure water vapour sample are required to determine the self pressure broadening values, whereas the water vapour – air samples are used to determine the pressure broadening due to air. They took precautions to ensure the temperature was constant, and that no contaminants could enter their experimental setup. The raw data clearly shows how the line shape is modified by changing pressure, and by feeding their data into a multi-spectrum analysis software utilizing a nonlinear least squares fitting method, they retrieved a self consistent set of line parameters [70].

The line shape function can be applied to calculate the spectral absorption coefficient. The absorption coefficient was utilized when describing Beer-Lambert's law, and it was given as a constant. This new definition reveals the dependence of the wavelength of light on the absorption coefficient:

$$\alpha(v,T,p)=S_{ij}(T)*f_L(v;v_{ij},T,p) \quad (2.3)$$

where S_{ij} has been introduced, and corresponds to the spectral line intensity. The spectral line intensity, as the name implies, is the intensity of the transition between two states weighted by the probability of transition, the isotope fraction (on earth) and the temperature, among other constants [71]:

$$S_{ij}(T) = I_a \frac{A_{ij}}{8\pi c v_{ij}^2} \frac{g_i e^{\frac{-hcEj}{k_BT}}(1-e^{\frac{-hcv_{ij}}{k_BT}})}{Q(T)} \quad (2.4)$$

Where k_B is Boltzmann constant, c is the speed of light, A_{ij} is the Einstein coefficient, and Q(T) is the internal partition sum. Q(T) is a factor which takes into account that at higher temperatures the ground state becomes increasingly depopulated. One expects Q(T) = 1 at absolute zero (the excited state is completely depopulated), and as T approaches infinity, so does Q(T). The ratio of $Q(T)/Q(T_{ref})$ provides a scaling factor which helps convert the expected line intensity at a temperature other than the reference as will be discussed below. Internal partition sum values are calculated and available through projects such as TIPS (Total Internal Partition Sum) for all available HITRAN molecules and isotopologues in intervals of 1-2 K up to 5000 K (typically, however the upper limit varies by molecule) [72].

HITRAN spectral line data are provided at T_{ref} which has been defined previously as 296 K. These reference lines are directly measured to a high degree of accuracy by groups such as Nakagawa et al [73] and complied into the database. If a measurement is to be taken at a temperature other than the reference temperature, a conversion from the reference line intensity must me made. The Einstein coefficient is calculated based on this reference intensity and is the means by which this conversion can be made:

$$A_{ij}^{-1} = I_a \frac{S_{hit}}{8\pi c v_{ij}^2} \frac{g_i e^{\frac{-hcEj}{k_B T_{ref}}} (1 - e^{\frac{-hc v_{ij}}{k_B T_{ref}}})}{Q(T_{ref})} \quad (2.5)$$

Where S_{hit} is the spectral line intensity at T_{ref} reported in the HITRAN database, and $Q(T_{ref})$ is the internal partition sum at the reference temperature. As can be easily seen, if one is taking measurements at the reference temperature, the result would be:

$$S_{ij}(T_{ref}) = S_{hit} \qquad (2.6)$$

Which means that the line intensity at $T = T_{ref}$ is equivalent to the line intensity tabulated in the HITRAN database as one would expect.

Looking back to the internal partition sum as described by Gamache et al [72], it is defined as:

$$Q_x(T) = d_i \sum_s d_s e^{\frac{-hcF_s}{k_B T}} \qquad (2.7)$$

Where Q_x is the internal partition sum of a particular quantized motion (rotational and vibrational in the case of this work), d_i and d_s are degeneracy factors, hcF_s is the energy of the particular state [74]. In general, the total partition sum of a ro-vibrational energy structure would be

$$Q(T) = Q_{vib}(T) x Q_{rot}(T) \qquad (2.8)$$

It should be noted that care must be taken when taking the product of the Q_{vib} and Q_{rot} while summing across all energy states as there may be combinations of vibrational and rotational states which are not physical, if this is the case then it must be done piecemeal.

Finally, after having examined all terms which must be taken into account when describing the absorption coefficient one can see how complex the prediction of the absorption of a photon is, even at the surface level. It is fortunate that a resource such as HITRAN exists in order to provide easy access to a significant number of common molecules. By importing a custom line by line output from the HITRAN database's web portal (which is constructed from hundreds of independent measurements made by researchers across the world) [75] it was possible to write a custom program which could provide the expected theoretical lines one would observe at a particular temperature (Figure 2.1).

Once these parameters have been imported into LabVIEW from the text file exported by the HITRAN web portal, they can be used to calculate the predicted absorption for a given pressure and temperature, modified for a particular concentration which is provided by the user (Figure 2.1). In order to calculate $f_L(v; v_{ij}, T, p)$ (equation 2.1), γ (p, T) (equation 2.2) is required first. The required parameters are taken from the HITRAN and user data, and the resultant γ (p, T) is then used to calculate $f_L(v; v_{ij}, T, p)$, along with v_{ij} and $\delta(p_{ref})$. $f_L(v; v_{ij}, T, p)$ is then multiplied by the spectral line intensity (which is also provided in the HITRAN data) to calculate the absorption coefficient (equation 2.3). The program will then iterate across the defined wavelength range with the defined resolution and calculate the absorption coefficient at each point. An example of such a calculation can be seen in Figure 2.2 where the results of our program utilizing the raw HITRAN data are compared to a supplemental HITRAN database used to make peripheral calculations upon the raw data [76]. For the data range used in this work, the program did not need to be optimized to stop calculating the absopriton coefficient when the

contribution of the surrounding absorption lines essentially reached zero, it simply continued until the dataset ended for each iteration; however for larger datasets it should be modified to do so.
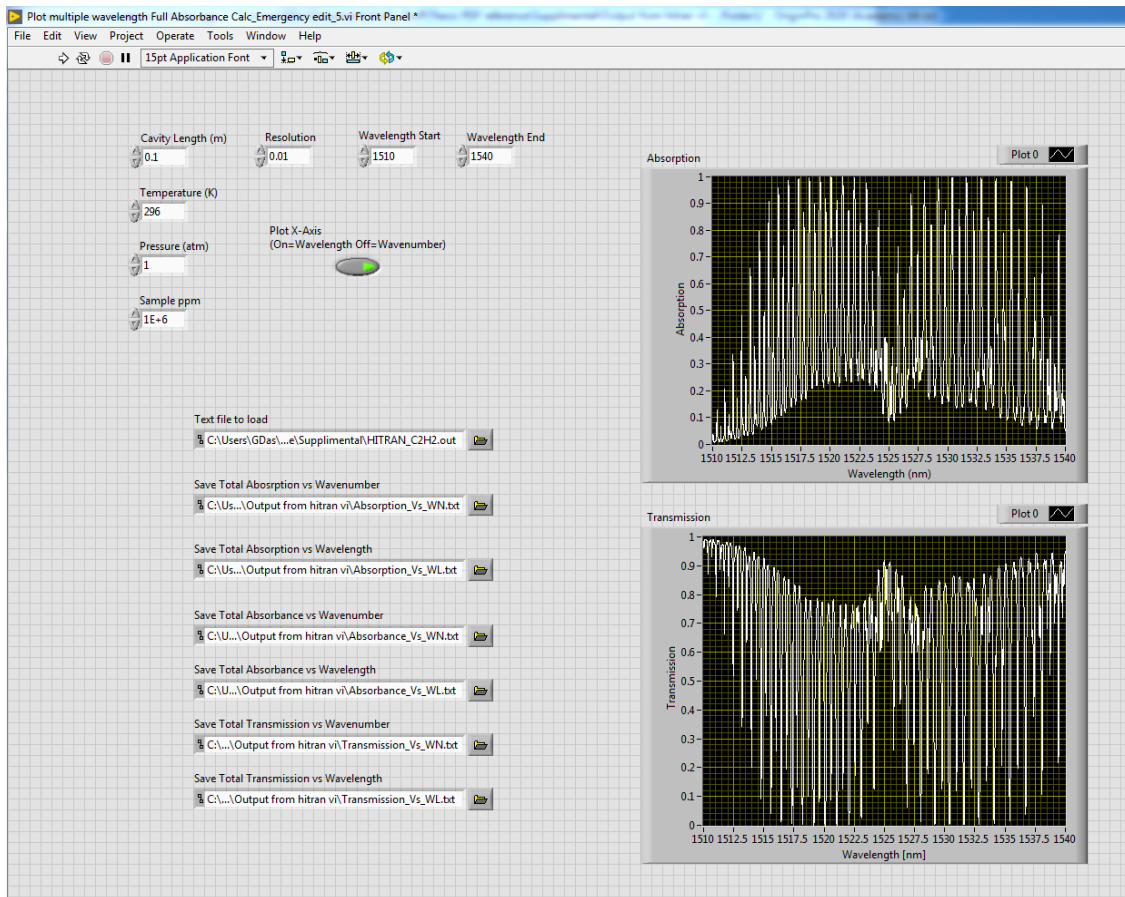
Figure 2.1: LabVIEW VI designed to intake raw HITRAN data and output absorption and transmission data for given temperature, pressure, and concentration given in ppm.
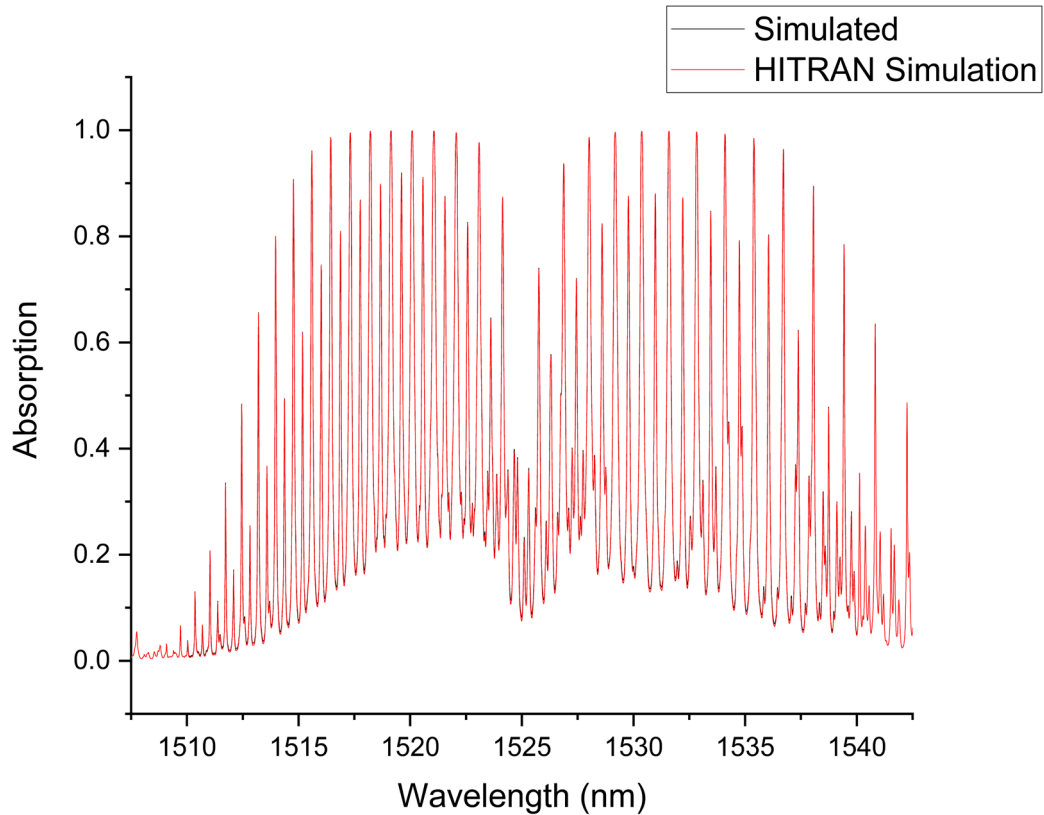
Figure 2.2: The absorption spectrum obtained from HITRAN data for C_2H_2 (100% concentration, 0.1 m path length at standard temperature and pressure) using LabVIEW VI (black) and from HITRAN computational tools (red) [76].

It is difficult to differentiate the two spectra obtained using LabVIEW VI and HITRAN computational tools in Figure 2.2 as they coincide almost exactly, with very slight variations in peak height and valley depth as can be seen in Figure 2.3, which is a close - up view of a particular absorption line simulated in Figure 2.2.
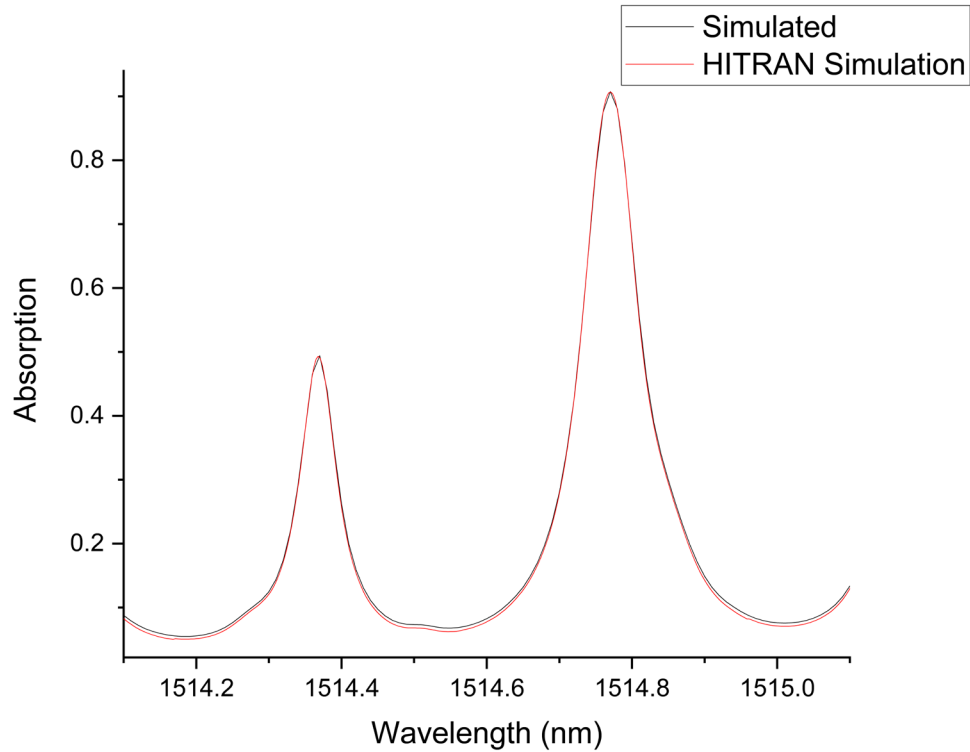
Figure 2.3: An expanded spectra of two absorption lines to show the variation with the simulation from our LabVIEW VI and the HITRAN computational tool.

2.2 Characteristics of Ro-Vibrational Absorption Lines

Now that the details on how absorption for a particular gas species can be simulated for a given temperature and pressure have been examined, it is practical to go into more detail about the structure of the absorption peaks. From a more advanced perspective, this change in molecular energy which results in the observed absorption lines is the result of the sum of the rotational-vibrational (ro-vibrational) energy, as the rotational and vibrational quantum numbers are changing [77].

C_2H_2 (Acetylene) will be taken as the primary example when discussing this topic as it is the primary gas species studied over the course of this work. Acetylene has seven primary modes of vibration (including four degenerate modes), labelled v_1 to v_5 (this v differs from the variable representing wave number seen previously). Because it is a linear molecule it has $3*N-5$ vibrational degrees of freedom, each corresponding to a particular vibrational mode. This expression for vibrational degrees of freedom comes from the following: $3*N$ for each direction in three dimensional space for each atom, subtracting two degrees of freedom for each axis the molecule can rotate (in a non-linear system there are three degrees of rotational freedom), and subtracting an additional three for each dimension of translational freedom [78]. These five fundamental modes of vibration can be seen in Figure 2.4. For Acetylene, $N = 4$ as it has two carbon and two hydrogen atoms, therefore $3*(4)-5 = 7$ modes of vibration as expected.
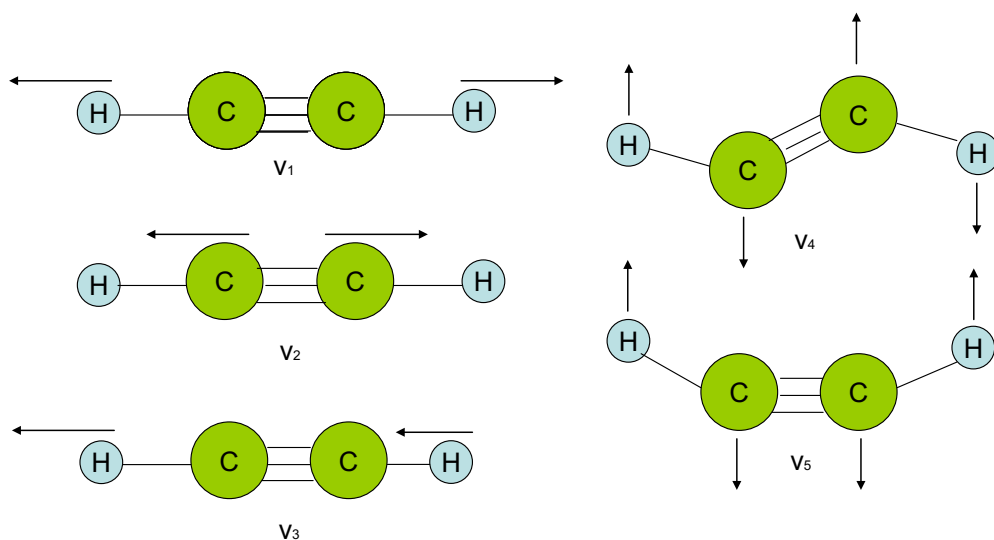
Figure 2.4: Fundamental vibrational modes of Acetylene (v_4 is degenerate and v_5 is degenerate)

Where v_1 corresponds to a symmetric C-H stretch at 2963.8 nm, v_2 corresponds to a symmetric C-C stretch at 5065.9 nm, v_3 corresponds to an antisymmetric C-H stretch at 3040.4 nm, v_4 corresponds to a symmetric C-H bend at 16339.9 nm, and v_5 corresponds to an antisymmetric C-H bend at 13698.6 nm [79]. The symmetric stretch/bend modes are not infrared active; this is due to the fact that there is no change in the dipole moment of the molecule:

$$\Delta p = \sum_k q_k \Delta d_k \qquad (2.9)$$

Where p is the dipole moment, q is charge, and d is the separation between atoms (length of the bond). Additionally the v_4 vibrational mode is degenerate, and so is the v_5 vibrational mode. One may question why a vibrational mode cannot be observed via infrared spectroscopy when its resonance frequency is clearly within the same range as other vibrational modes which are easily observed. A more qualitative way to address the question of whether or not a particular vibrational mode in a simple molecule such as acetylene is infrared active is by imagining it is placed within a spatially uniform electric field. The field from the laser used to stimulate a vibrational mode can be considered spatially uniform when one considers the incredible size difference between the stimulating wavelength (thousands of nanometres, typically) and the size of the simple molecule (perhaps several dozen angstroms at most). The magnitude force acting on a charged particle in an electric field within this thought experiment is given by the simple equation F = Eq, where E is the electric field strength, q is the charge on the particle, and

F is the force experienced. When observing v_1 in Figure 2.4, would it then be possible for a uniform field, E, to produce a stretch in opposite directions on identical particles with identical bonds, which therefore must have identical charges, q? This cannot be the case, and the same logic can be applied to the other examples of symmetric stretching seen in Figure 2.4. The exact opposite result is found when v_3, an antisymmetric stretch is considered in the same thought experiment. It is clear that the hydrogen atoms could be induced to move in the same direction by a uniform electric field if they were of the same charge, resulting in an antisymmetric Δd. Applying this knowledge to the change in dipole moment expressed above, it becomes clear that if the change in distance is symmetric, and the charge is the same, then the change in dipole moment will sum to zero, however this situation is not possible under the conditions of infrared absorption. In the other situation, where the change in Δd is antisymmetric, it is clear that the change in dipole moment will not sum to zero.

These fundamental modes of vibration lay far beyond the typical range considered when dealing with the telecom wavelength band. Additionally, the region in which these fundamental modes inhabit is quite crowded with absorption lines of other gas species (Fingerprint zone), making accurate readings of the absorption of a particular gas species when it is in atmosphere difficult. For these reasons a combination band of the fundamental modes has been considered for this work. For example, the $v_1 + v_3$ vibrational mode is centered at 1525 nm, which is within the telecommunications band. This combination band location is approximated by summing the inverse of the primary bands: $1/v_{1+3} = 1/v_1 + 1/v_3$. Although the absorption cross section of the combination

band is significantly lower than the primary vibrational modes (Figure 2.5), the benefits of examining this region outweigh the costs.
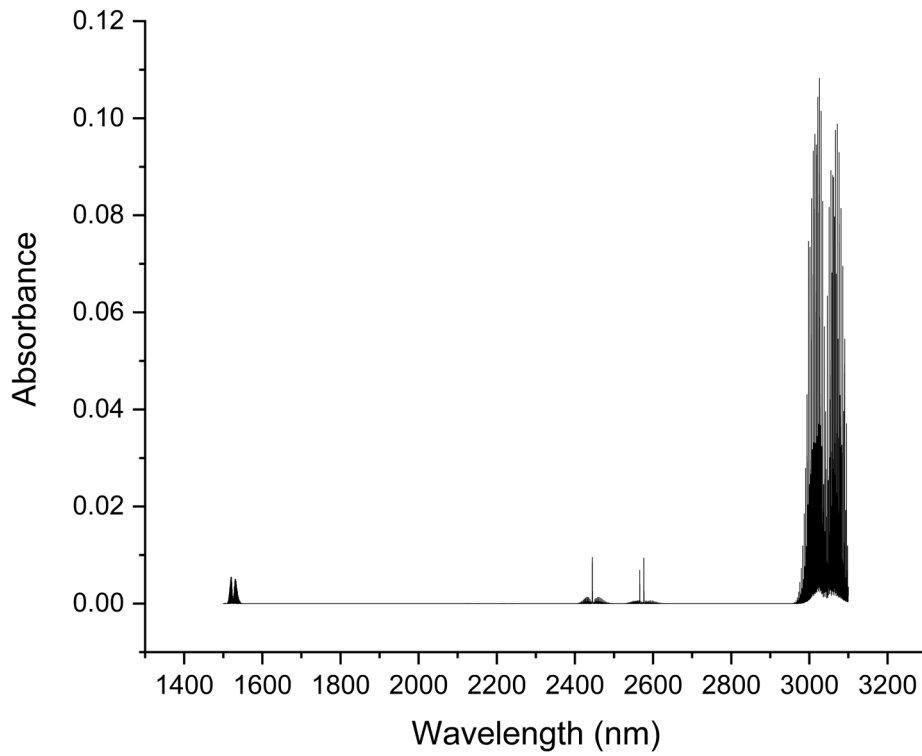
Figure 2.5: Absorption of Acetylene from at standard temperature and pressure 1500 - 3100 nm for a 100 ppm concentration and a 1 m path length simulated in LabVIEW.
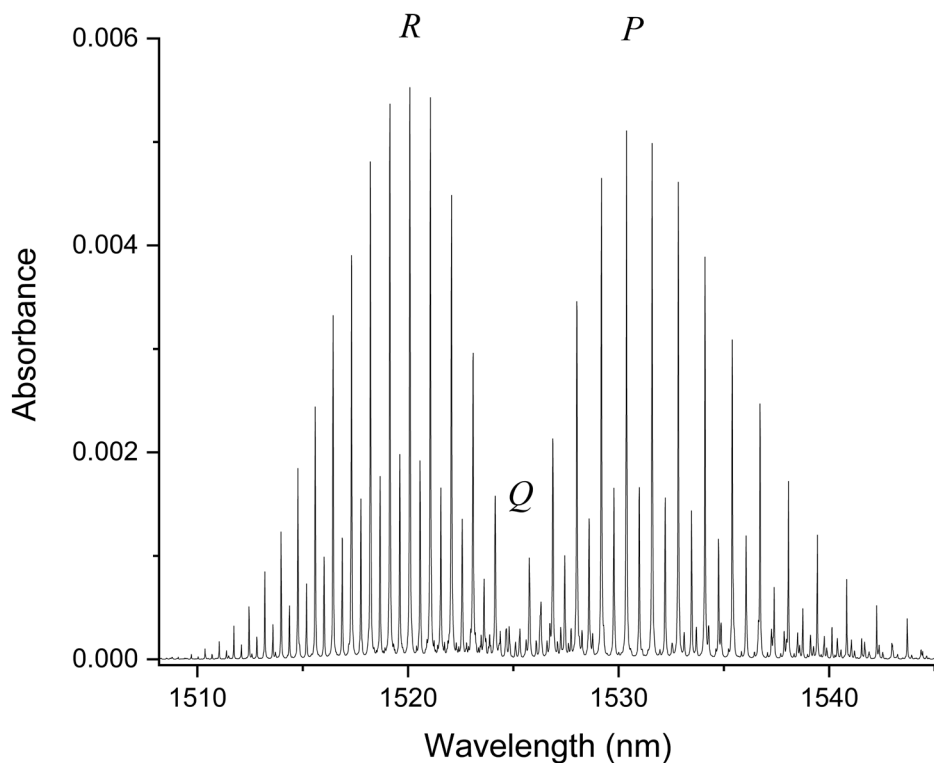
Figure 2.6: The $v_1 + v_3$ combination band of acetylene simulated in LabVIEW with a concentration 100 ppm, path length of 1 m, with labelled ro-vibrational features.

The structure of the $v_1 + v_3$ combination band is characteristic of most vibrational bands in that it has three distinct structures. The three main structures seen in Figure 2.6 indicate the 'branches' of the vibration (in this case the $v_1 + v_3$ vibrational mode). These branches are a result of the quantum nature of the transitions. To begin this discussion, an introduction to the quantum numbers involved must be made. J is the quantum number representing the total angular momentum of the system. The Q branch represents a transition where the change in total angular momentum between two states is zero, the R

branch represents the transition where the total change in angular momentum is 1, and finally the P branch represents the transition where the total change in angular momentum is -1. These three distinct regions form the skeleton of a particular vibrational mode [78].

One of the foundational principles of Physics is that momentum, or in this case specifically angular momentum, must be conserved. Photons have a particular quantized unit of angular momentum, and when one imagines a photon being absorbed by a molecule, inducing a vibration, the angular momentum cannot simply disappear, it must go somewhere. This is easy to visualize for the R and P branches, where the angular momentum is incremented either up or down by one unit of J respectively, however it is less intuitive when it comes to the Q branch. In order for the $\Delta J = 0$ transition to occur, there must be an alternative sink for the angular momentum of the photon. This is the case when the vibration is non-parallel to the primary axis, which can be expressed through another quantum number K, the rotational quantum parameter [78;80]. For a linear molecule whose vibration is parallel to the primary axis K=0, and the Q branch is forbidden, as can be observed in Figure 2.6. Vibrations which are increasingly non-parallel to the primary axis will have K>0 integer values, allowing $\Delta J = 0$ transitions. An example can be found in the $v_1 + v_5$ combination band of acetylene seen in Figure 2.7, where the Q branch transitions are allowed.
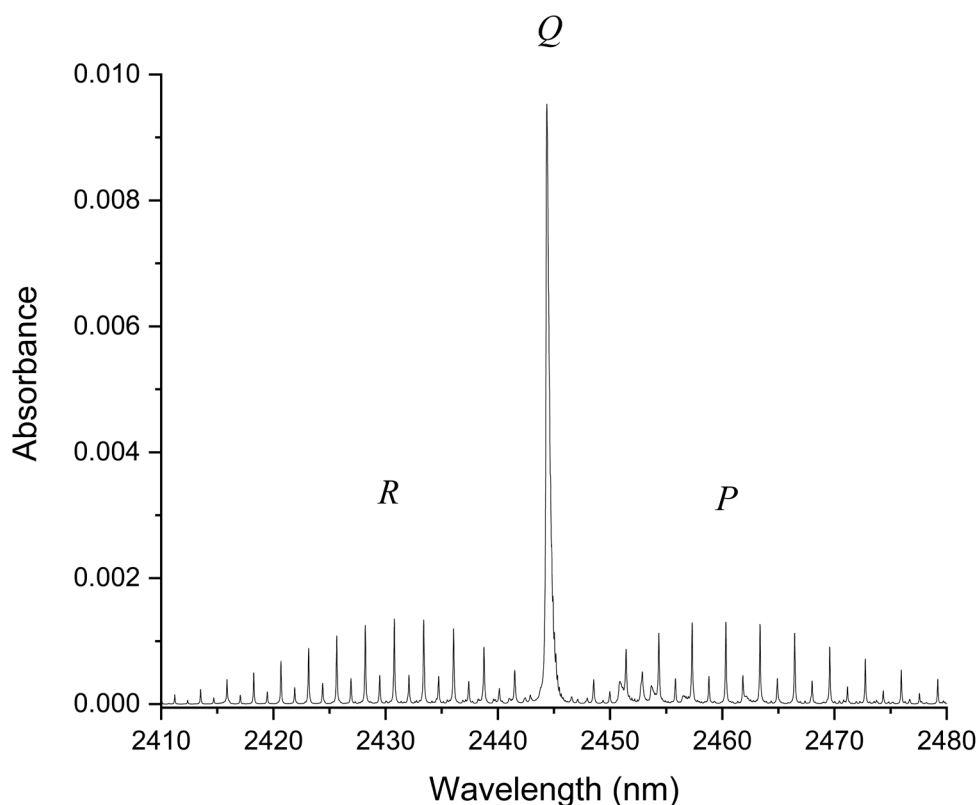
Figure 2.7: The $v_1 + v_5$ combination band of acetylene simulated in LabVIEW with a concentration of 100 ppm, path length of 1 m, with labelled ro-vibrational features.

The next characteristic features of the branches of a ro-vibrational spectrum are the intensities and separation of the rotational lines seen for a particular vibrational mode. These rotational lines make up the structure of the branches, and in both Figure 2.6 and Figure 2.7 they appear as alternating high and low intensity peaks wrapped in a typical Boltzmann distribution, with decreasing separation in the R branch and increasing separation in the P branch. The variance in separation is typical of all ro-vibrational spectra, however the alternating intensity depending on the parity of the lower J value in

a particular transition may not always be observed as it depends on nuclear spin statistics [81]. Taking on the latter point, when a linear molecule such as acetylene is examined, one must consider the number of nuclei present in the molecule along with their spin. If there are an even number of identical nuclei equidistant from the symmetric center of the molecule which have half integer nuclear spin, then the nuclei must be considered Fermi particles, and as such must follow Fermi-Dirac statistics, a condition which is met by acetylene whose hydrogen nuclei have half integer nuclear spins (hydrogen has spin ½). In order to understand the consequences of this on the ro-vibrational spectrum, diatomic hydrogen will be taken as a simplified example. The two hydrogen atoms which make up diatomic hydrogen must confine themselves to Fermi statistics as they are identical and indistinguishable particles with half integer spin, as such they must have anti-symmetric states (analogous to electrons requiring opposite spins to remain in the same orbital, as a result the overall system remains anti-symmetric). The total wave function of the system can be expressed as:

$$\psi = \psi_e \psi_v \psi_r \psi_n \qquad (2.10)$$

Where ψ_e is the wave function for the electronic state, ψ_v is the wave function for the vibrational state, ψ_r is the wave function for the rotational state, and finally ψ_n is the wave function for the nuclear spin. ψ_e in the ground state and ψ_v are considered symmetric in this molecule, ψ_r has symmetry related by $(-1)^J$, as such it will be antisymmetric for odd J and symmetric for even J (here we are taking J as the total angular momentum quantum number of the lower state in a particular transition). The wave function for nuclear spin

can have several forms. Firstly a new quantum number M_I must be introduced which may hold the values of +/- ½ (nuclear spin of hydrogen). Considering that either hydrogen may either hold the quantum number $M_I = +1/2$ or $M_I = -1/2$, there are four permutations of diatomic hydrogen which may be considered [81]:

$$H_1(M_I = +1/2)H_2(M_I = +1/2) \qquad (2.11)$$

$$H_1(M_I = -1/2)H_2(M_I = -1/2) \qquad (2.12)$$

$$H_1(M_I = +1/2)H_2(M_I = -1/2) \qquad (2.13)$$

$$H_1(M_I = -1/2)H_2(M_I = +1/2) \qquad (2.14)$$

It is clear that the first two permutations are symmetric, as an exchange of either M_I would not result in a change of the function; however the final two permutations are not. By taking a linear combination of the final two permutations, one receives both a symmetric and antisymmetric function:

Symmetric: $2^{-1/2}$ $(H_1(M_I = +1/2)H_2(M_I = -1/2) + H_1(M_I = -1/2)H_2(M_I = +1/2))$ (2.15)

Antisymmetric: $2^{-1/2}$ $(H_1(M_I = +1/2)H_2(M_I = -1/2) - H_1(M_I = -1/2)H_2(M_I = +1/2))$ (2.16)

Due to the fact that three out of four nuclear spin permutations are symmetric, one would expect the probability of the system being in a state that requires an antisymmetric rotational wave function to be 3:1, the only way to have an antisymmetric rotational wave function is to have an odd J integer, as such one would expect transitions from states with an odd J integer to have three times the intensity as they should have, statistically, three

times the population. This ratio is quite similar to what is observed in the more complex acetylene system's P and R branches in Figures 2.6 and 2.7.

Now, addressing the point made several paragraphs ago, that the separation between rotational lines varies depending on the location within the P and R branch. To begin, we will simplify a bond between two atoms down to a rigid rotor, then the energy of a particular vibrational state is defined as [80]:

$$E_v = \frac{hc(v+\frac{1}{2})}{\lambda} \qquad (2.17)$$

Where J has been previously defined as the total angular momentum quantum number, c is the speed of light, and v is the vibrational quantum number (may hold positive integer values starting from 0). The term hc/λ will be set to A. The energy of the rotational state is found by solving the Schrödinger equation for a rigid rotor [81]:

$$E_r = \frac{h^2}{8\pi^2 \mu r^2} J(J+1) \qquad (2.18)$$

Where the coefficient of J is set to B_v, the rotational constant, which is inversely proportional to the length of the bond (r) squared and the reduced mass of the system, μ. The total energy of the ro-vibrational state is then:

$$E_{ro-vib}(v,J) = E_v + E_r = A(v+\frac{1}{2}) + B_v J(J+1) \qquad (2.19)$$

If one accepts that the length of the bond tends to increase as the energy of the system increases, then it follows that $B_v > B_{v+1}$ as B is inversely proportional to r. So if the example is followed through by imagining a transition from the ground to the first vibration state (v = 0 to v = 1), and for the R branch (recall $\Delta J = +1$) we transition from J to J+1, then:

$$\Delta E_{ro-vib} = E_{ro-vib}(1, J+1) - E_{ro-vib}(0, J) \quad (2.20)$$

$$\Delta E_{ro-vib} = A(1 + \frac{1}{2}) + B_1(J+1)(J+2) - A(0 + \frac{1}{2}) - B_0 J(J+1) \quad (2.21)$$

By simplifying it is clear that:

$$\Delta E_{ro-vib} = A + J^2(B_1 - B_0) + J(3B_1 - B_0) + 2B_1 \quad (2.22)$$

As has been stated, $B_1 < B_0$, as such the coefficient on J^2 will be negative, which indicates that as J increases, the separation between the energies of adjacent rotational lines will decrease as the positive portion of the expression is out-scaled by the negative portion. It is important to keep in mind that the R branch increases in energy as J increases in R(J). When looking at either Figure 2.6 or 2.7, and beginning from the Q branch, it is clear that each ro-vibrational line encountered in the R branch occurs at decreasing wavelengths (increasing energy). So, if the separation between the higher and lower rotational lines occurs after a smaller change in energy, then the lines will occur closer together as J increases.

The same process can be done for the P branch where $\Delta J = -1$, as such the final state must be J-1 rather than J+1 as in the example illustrated for the R branch:

$$\Delta E_{ro-vib} = E_{ro-vib}(1, J-1) - E_{ro-vib}(0,J) = A(1+\frac{1}{2}) + B_1(J-1)(J) - A(0+\frac{1}{2}) - B_0(J)(J+1) \quad (2.23)$$

Once again, by simplification:

$$\Delta E_{ro-vib} = A + J^2(B_1 - B_0) - J(B_1 + B_0) \quad (2.24)$$

As before, B_1-B_0 must be negative, as such the coefficients on both J and J^2 are negative. It is important to note that the P branch decreases in energy with increasing P(J). Just as before, when observing either Figure 2.6 or 2.7 and beginning at the Q branch, it is clear that each P(J) ro-vibrational peak encountered is occurring at subsequently higher wavelengths. As such, each peak encountered is occurring at a lower energy. From the above equation, it is obvious that as J increases, the change in energy will be increasingly negative, resulting in increasing separation between adjacent ro-vibrational peaks.

Chapter 3

Gas cell based on Segmented Hollow-Core Photonics Crystal Fiber (HC-PCF)

3.1 Introduction

There is a growing demand for sensitive, compact, and affordable spectroscopic devices for sensing applications. Spectroscopy has already found many uses in medicine, environmental monitoring, and industrial processing [12-14]. Further, optical fiber technology is becoming increasingly common due to its low cost and robust nature. HC-PCF is ideal for a compact gas cell due to a very high degree of laser–sample interaction while requiring very little physical space and a small sample volume [82]. One of the disadvantages of HC-PCF is longer gas filling and evacuation times due to the small core size and longer length, thus greatly improved the response time. The gas cell based on segmented HC-PCF developed in this work eliminated the above drawback. The developed gas cell was placed inside a laser cavity, which formed an intracavity laser absorption spectroscopic system (ICLAS). The laser wavelength was selected using a fiber Bragg grating (FBG). The fiber Bragg grating wavelength was centered between the R (5) and R (4) rotational lines of the acetylene $v1 + v3$ combination band, at 1522.22 nm, and used to probe their absorption. We investigated the use of off-resonance laser wavelength to develop a highly sensitive detection system.

3.2 Experimental Design

Figure 3.1 displays a block diagram of the system, where each component plays an important role in the stability and function of the spectroscopic system. The pump laser (908 nm, 150 mW) is coupled into the ring cavity by use of a wavelength-division multiplexer (WDM) coupler. A WDM is a device which allows the coupling of multiple wavelengths of light into a single optical fiber [22]. As the pump laser excites the erbium ions within the polarization-maintaining Erbium-doped fiber (PM-EDF), both stimulated and spontaneous emission of photons occurs. Ideal silica single mode fiber is not birefringent. Birefringence is a material property where its index of refraction is different depending on direction. However, any anisotropy of the fiber geometry will introduce a source of birefringence in the fiber and will result in two polarization modes (along the x-axis and y-axis); this can be caused by bending the fiber itself or even through defects in manufacturing. Polarization-maintaining fiber introduces an extra component within the fiber; either in the form of stress rods, or by breaking the cylindrical symmetry of the core/cladding and forming an ellipse. By introducing stress into the fiber through either of these methods, a strong source of birefringence is introduced which preserves the polarization state of the light along a particular direction [22]. Including the PM-EDF in the laser cavity increases the stability of the laser wavelength compared to a circular core Erbium-doped fiber. The broad characteristic emission spectrum of the EDF is due to Amplified Spontaneous Emission (ASE). As stated previously, this broad range of ASE being produced within the system is traditionally seen as a detriment, but when one considers its use as a large canvas to capture the imprint of the absorption spectra of a

particular molecule, it can be turned into a benefit. The Polarization Controller (PC) in the cavity assisted in controlling the polarization state of the light inside the cavity. Optical isolators (OI) are included to ensure unidirectional propagation of light within the laser cavity, and where unidirectional propagation occurs an arrow is present to show the direction in the diagram.
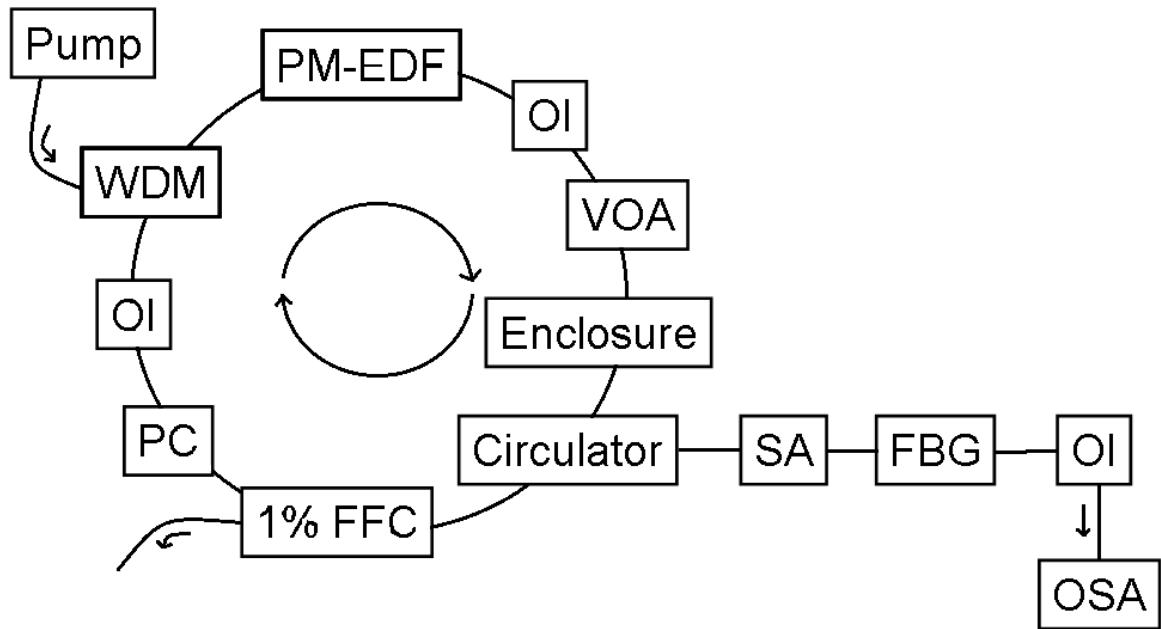
Figure 3.1: Block diagram of the full system used with arrows indicating the direction of propagation [45].

The Variable Optical Attenuator (VOA) is an electronic device which was included in order to accurately control the loss of the cavity. If one desired the system to lase at a particular input power, increasing or decreasing the attenuation introduced by the VOA would allow this to be possible (assuming the minimum attenuation of the VOA was not above the required loss of the cavity to lase).

The developed gas cell based on the segmented HC-PCF was placed inside an enclosure which was fitted with a gas inlet and outlet. An unpumped PM-EDF was used as the Saturable Absorber (SA). The FBG, in the configuration seen in Figure 3.1, reflects light at the Bragg wavelength, which results in bidirectional propagation of light through the SA. This bidirectional propagation creates a standing wave pattern which in turn creates a dynamic grating within the SA, this reduces mode hopping and improves overall system stability [83]. The Polarization Controller (PC) and Saturable Absorber (SA) are introduced to increase the stability of the laser with respect to small temperature fluctuations. An all - fiber PC consists of three plates, where several fiber loops were used to make either quarter or half wave plates. The bend – induced birefringence (a non-uniform change in the effective refractive index along the x and y axis of the fiber, where the z axis is the direction of propagation) alters the polarization state of the light as they propagated through the PC [84]. The 1% Fused Fiber Coupler (FFC) allows a small amount of power from the ring cavity to be sent to a detector, which allows for real time adjustment of the systems pump power or attenuation in order to reach the lasing threshold without requiring multiple scans using an optical spectrum analyzer (OSA), or a disruption of the output of the system to a power meter from the OSA. By observing the indicated power from the FFC the system can be precisely brought to the threshold condition where the gain and loss of the cavity are nearly equivalent, and a small gain would lead to system lasing.

The circulator is an optical device which passes inputs and outputs to predetermined ports [22]. For example, in a traditional three port circulator, an input at port one would output at port two, but not three. An input at port two would output at port three but not

one. This device operates utilizing a similar principle to the OI included within the system. By taking advantage of this component, light entering from the clockwise direction within the ring cavity (port one) will be output into the branch containing the SA and the FBG (port two). The light will then interact with these components, and the FBG, which has peak reflectivity at 1522.2 nm, will primarily reflect this wavelength back towards the circulator which then outputs the received reflected signal in the clockwise direction of the ring cavity (port three). Because the wavelength of light reflected by the FBG is determined by its peak reflectivity, this is the wavelength of light which is primarily circulating within the ring cavity. By the principle of stimulated emission, this becomes the primary wavelength of photon stimulating the emission of other photons, and thus becomes the wavelength of light the system lases at. When lasing, the peak wavelength spikes above the background ASE and it becomes clearly visible when the output of the system is taken. When the system is not lasing (the loss of the cavity is greater than the gain) there is a distinct dip observed at the location of the FBG wavelength. By introducing a FBG with a particular central wavelength within the range of the ASE, the lasing wavelength is forced to coincide with it. One can then tune the lasing wavelength to occur at the same position as an absorption line of a sample of interest, and when operated near threshold this has been shown to dramatically increase the sensitivity of the system which has been shown by past members of the photonics research group [46].

The wavelength range in which the system described above operates is at the telecommunications band (~ 1550 nm). This region was chosen due to the fact that optical components utilized in the telecom industry are mass produced, and as such are

significantly cheaper than specialty devices which would be required to operate optimally at different wavelengths. Additionally, detectors operating at this wavelength window do not require temperature stabilization and can be used at room temperature, which once again is a cost savings. The availability of optical components from the telecom industry makes the development of a cost effective and compact all fiber laser spectroscopy system possible. The downside of operating in this region is that the absorption cross section in this band is considerably lower when compared to that at the fingerprint zone (mid-IR range). Thus, spectra obtained from any gas sample will be significantly lower than the spectra obtained when operating at the mid - infrared (mid-IR) region. This is why a system with high sensitivity is required, to detect gas at lower absorption coefficients. Another advantage to working outside of the 'fingerprint' region (which spans from 600 to 1400 cm^{-1} or 7100 nm to 16666 nm [85]) is that the overlap of absorption bands for many atmospheric gases within this region is significant which can make it difficult to find an isolated absorption line for a particular gas sample. By moving down to the near - infrared region, absorption peaks become more easily isolated which makes determining the concentration of a particular gas in the atmosphere a simpler task. This assumes the relatively low absorption level can be detected in the first place.

Finally, the gas cell used in this gas detection system will be discussed in detail. Previous work done with HC-PCF as a gas cell has suffered from a particularly severe limitation, and that is the length of time required to fill the gas cell with a particular sample. In order to overcome this problem, the design of a segmented HC-PCF gas cell was undertaken. The segmented gas cell was developed following a number of steps: First, two pigtailed ceramic ferrules with single mode fiber (SMF) were prepared and

connected by a sleeve. The optimum separation between two ceramic ferrules was determined by series of experiments. One end of the SMF was connected to a 1522 nm laser and output was monitored by a power meter at the other end. In the beginning the coupling efficiency was quite unreliable: this was due to the fact that producing consistent separation between the ferrule ends was challenging. Figure 3.2 depicts the first results of coupling efficiency between single mode fiber using pigtailed ferrule segments (Figure 3.3). It should be noted that in real world applications when using single mode fiber in this way, one would simply push an excess amount of fiber through the ferrule filled with epoxy. The ferrule face would then be polished until smooth, and the two faces could then be mated together nearly perfectly. This is not an option when dealing with HC-PCF as the fiber core is hollow, and it would be far too easy for debris to enter the fiber, and certainly for epoxy to clog the end if it were pushed through in a similar manner. As such an alternative means of manufacturing had to be considered.

The HC-PCF was stripped of its protective polymer coating with a razor blade, and the end was cleaved such that the surface was uniform. The HC-PCF was then inserted into a ceramic ferrule until the tip of the fiber could be observed to have exited the other end. It is important to ensure that there is no bare HC-PCF visible outside the ferrule, as this portion of the fiber without support from the ceramic ferrule would be brittle and prone to breaking. Once two HC-PCF ends have been prepared in this way, they are aligned under a microscope such that the tip of the HC-PCF is visible. A quick cure epoxy is then applied to the HC-PCF, and the fiber is drawn back approximately 75% of the length of the ferrule, allowing the epoxy to coat the majority of the fiber, but not allowing it to come near the tip which would ruin the future connection. The fiber is then slowly

inserted back through the ferrule, and it is aligned such that the tip of the HC-PCF is hardly visible due to it being nearly flush with the face of the ferrule, which keeps the face of the HC-PCF in line with the face of the ferrule and prevents it from damage if the two ferrules were to collide during alignment. Once the epoxy cures the ferrules are inserted into a sleeve which holds them in line, and they are moved together until there is a micron order separation between them (Figure 3.4). At this point, fine adjustment can be done by coupling one end of the HC-PCF to a power meter and the other to a laser, and the overall power loss can be monitored to ensure it is in line with the previously determined experimental losses for the SMF. This process is repeated for each new HC-PCF connection that is made. The average coupling efficiency for an HC-PCF ferrule connection was 86.7 % (higher than that observed for the SMF connections displayed below).
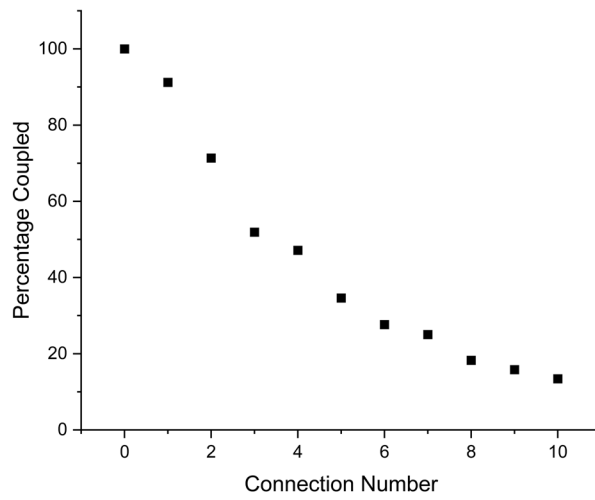
(a)
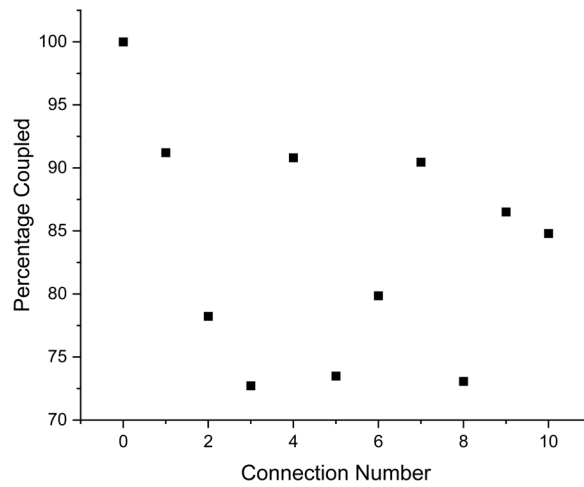
(b)

Figure 3.2: (a) Percentage of the power coupled compared to the original unsegmented 10 m strand of single mode fiber, (b) Percentage of the power coupled compared to the previous segment's output.

Figure 3.3: Ferrule connections using a sleeve, notable features include the epoxy seen on the far left and right-hand sides, as well as the black clamp which is used to hold the connection in place. The line near the center is where the two ferrule faces (micron order separation).
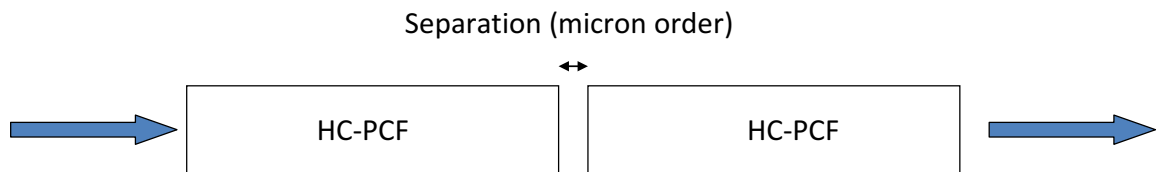

Figure 3.4: Schematic of the HC-PCF connections made using ferrules with a small gap in between to allow gas flow.

In order to improve upon the coupling efficiency of the connectors, a microscope was used when manufacturing each end of the ferrule connection, as well as when aligning the ferrule faces. In this way a more consistent product was made, and the fiber was able to be aligned nearly perfectly to the face of the ferrule. Additionally, epoxy was added along the length of the stripped fiber before it was inserted into the ferrule. Only approximately three quarters of the stripped surface were covered, leaving some buffer room for the delicate HC-PCF tip. Figure 3.5 displays the improved coupling efficiency obtained when using this method of manufacturing for SMF.
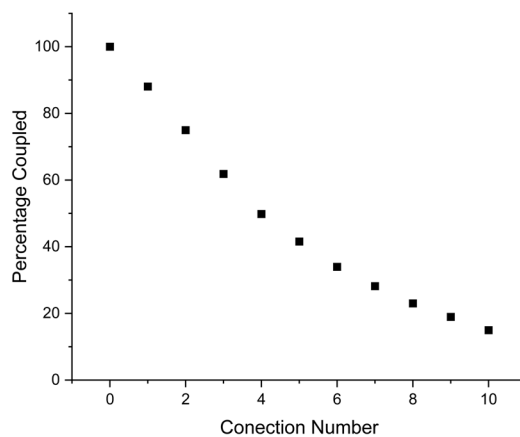
(a)
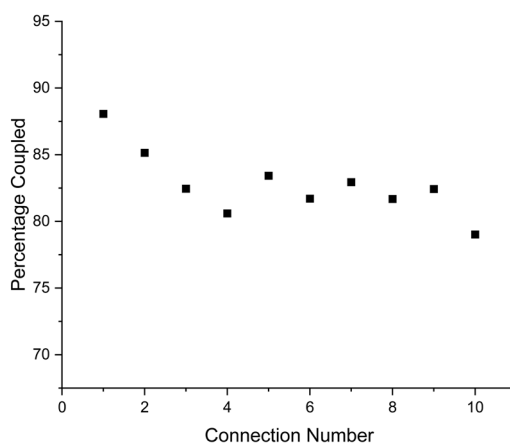
(b)

Figure 3.5: (a) Percentage of the power coupled compared to the original unsegmented 10 m strand of single mode fiber, (b) Percentage of the power coupled compared to the previous segment's output.

Once the process of creating segmented ferrule connections was completed, the effect of such connections on a HC-PCF gas cell needed to be examined. Acetylene gas (C_2H_2)

was used to test the functionality of the gas cell. The developed gas cell was placed in an enclosure as described earlier and incorporated in the ICLAS system. In order to take each measurement which will be displayed in the upcoming pages, a background scan of the system containing only nitrogen gas was taken (nitrogen gas is not infrared active, as should be clear by the arguments made in the previous section). The system was then evacuated for a particular amount of time (ranging from a constant flush of sample to a one-hour evacuation of the cell before the introduction of the sample) before a sample gas of a particular concentration was introduced. The resulting scan then had the background subtracted from it. By subtracting the two scans we obtained the absorption spectrum of the gas. Figure 3.6 displays a typical example of a background scan, as well as a scan containing sample, in addition to the result of their subtraction.
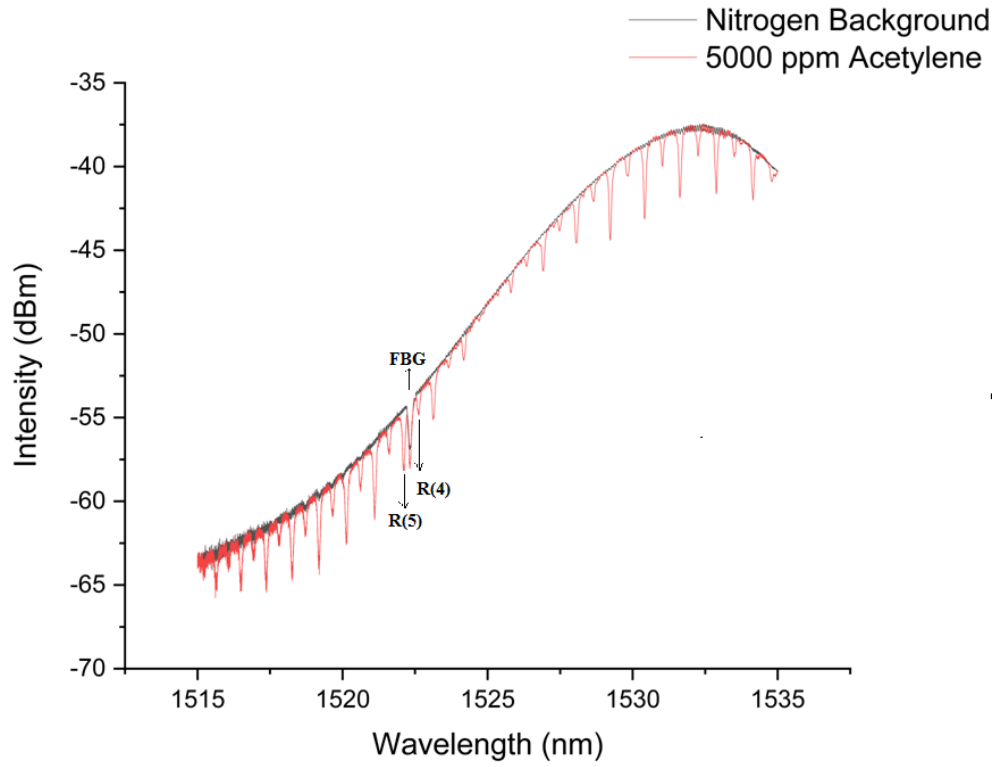
(a)
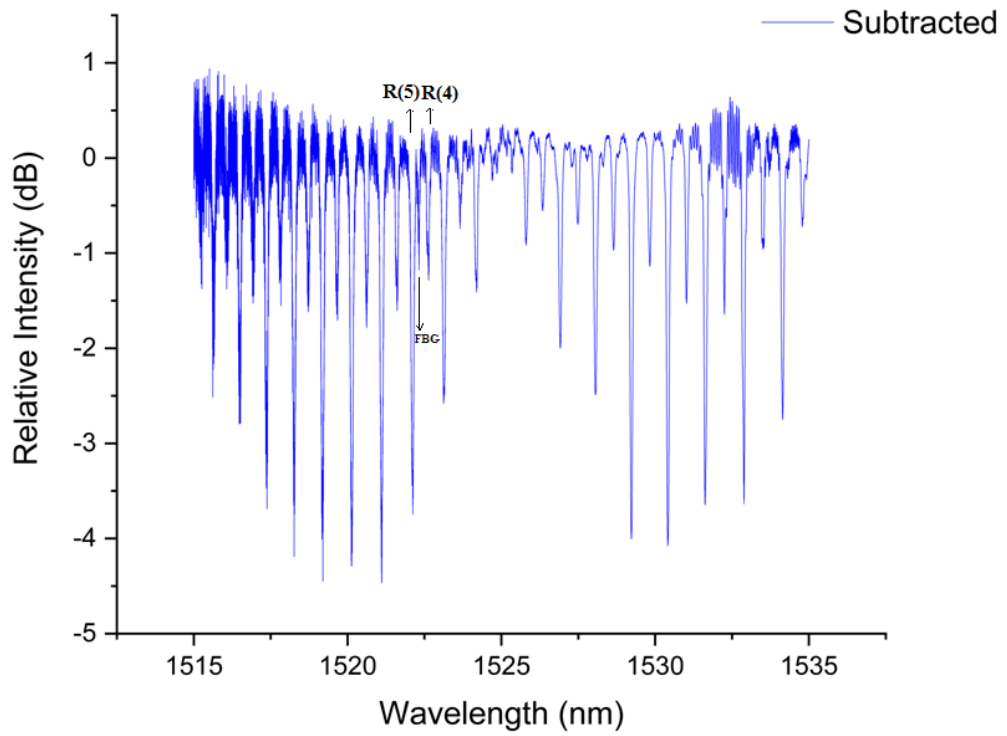
(b)
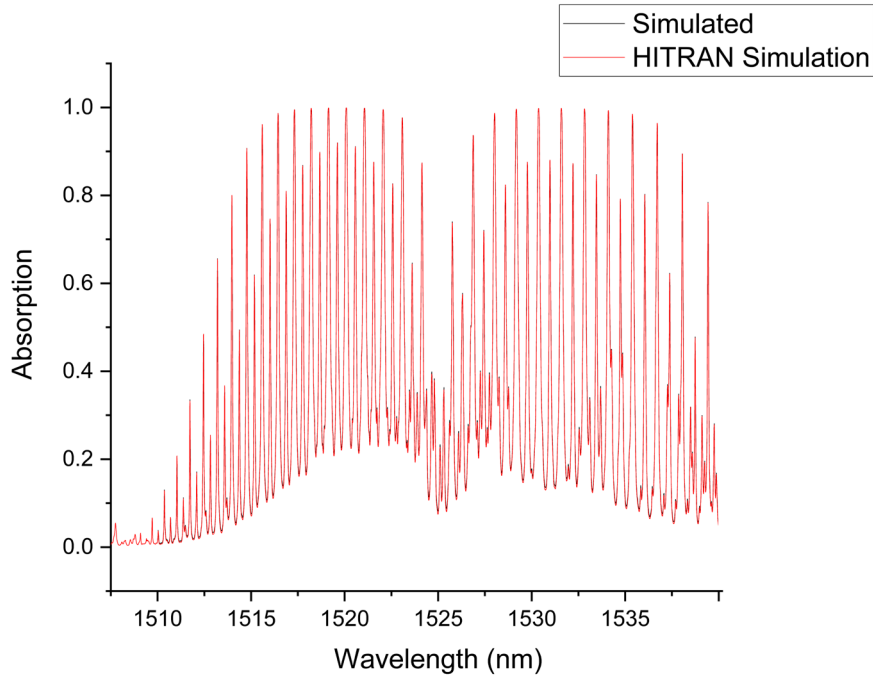
(c)

Figure 3.6: Output of the ICLAS system (a) the overlaid spectra of both the nitrogen background and acetylene sample (5000 ppm, within a 4 m HC-PCF gas cell evacuated for one hour), (b) the resultant spectra when the acetylene spectra has had the nitrogen background subtracted, and (c) the theoretical absorption lines.

As described earlier, the segmented HC-PCF gas cell was contained within a relatively large enclosure (10x12x5 inch) which was equipped with quartz windows to allow the laser to be passed into the container and coupled into the gas cell (Figure 3.7). The coupling of light into the chamber was achieved via a lens system mounted on a three - axis translation stage on the exterior of the enclosure for both the input and output of the system. The input and output ends of the segmented HC-PCF gas cell were mounted on two simple fiber holders and aligned with the center of their respective quartz windows.

The chamber size facilitated ease of access, and could easily be reduced in size to more closely fit the HC-PCF gas cell. One of the benefits of such a gas cell is that it requires significantly less sample than the alternatives. The enclosure also had a filtered gas inlet, and a gas outlet, in order to cycle sample through the chamber, and stops any dust particles to enter the HC-PCF core, which can clog the core of the fiber. This chamber was pumped out for a particular amount of time, detailed in the following section, before sample was allowed to enter, giving the HC-PCF time to evacuate in order to be filled again.
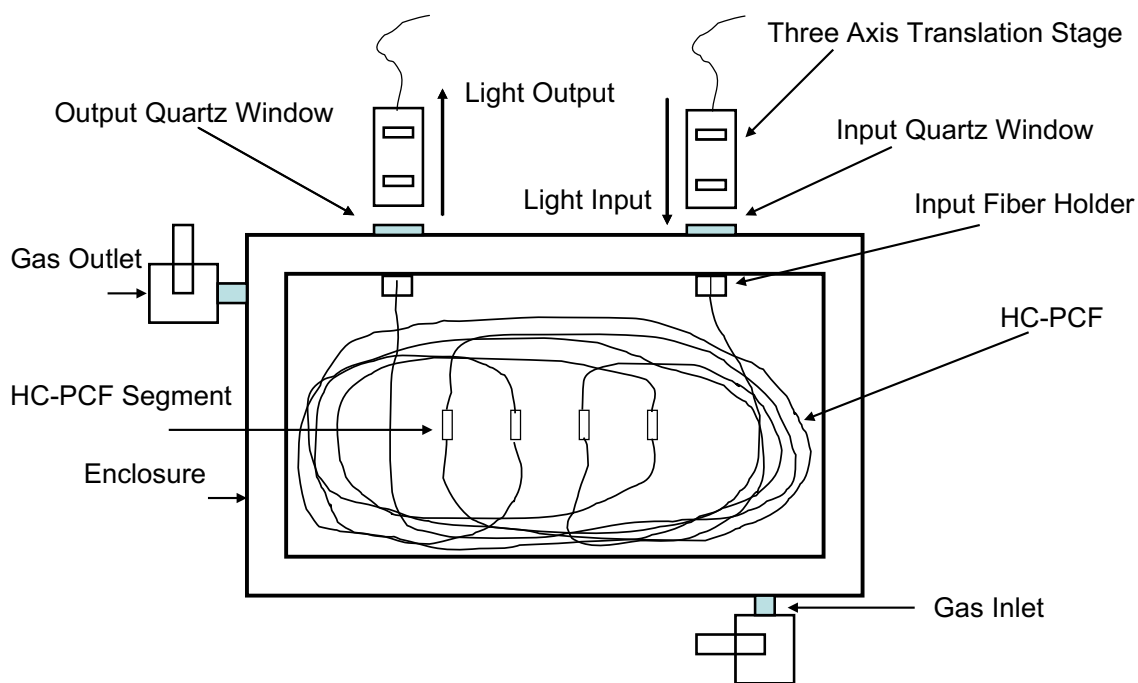
Figure 3.7: Schematic of the enclosure housing the HC-PCF gas cell.

The acetylene samples which were fed into the enclosure were prepared from a 0.5% (5000 ppm) standard purchased from Praxair Inc. This standard was diluted using a flow

controller (OMEGA Mass Flow Controller FMA5412) with nitrogen gas to the desired concentrations. The flow controller was controlled via a LabVIEW VI. The spectra were taken using an Anritsu MS9740A OSA, which was also controlled via LabVIEW with a custom VI, whose front panel is displayed in Figure 3.8.
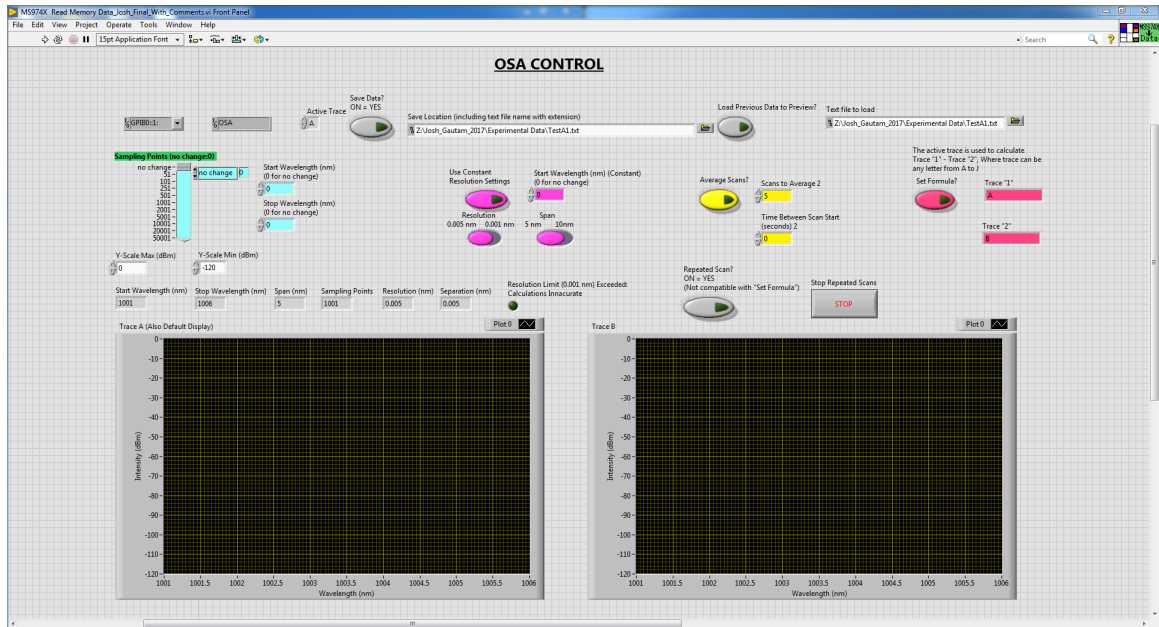
**Figure 3.8:** Front panel of the VI used to control the Anritsu Optical Spectrum Analyzer for all data collection.

3.3 Effect of Multiple Sample Flush

The core size of the HC-PCF used in this work was 20 microns (HC19-1550, NKT Photonics). As has been found through direct experimentation, as the evacuation time of the system increases, the observed absorption peak depth of a particular sample is

increased. In the following figures the R(5) absorption line (see Figure 3.6) is highlighted in order to have a consistent point of comparison between experiments. Additionally, it has been shown that if the system is flushed multiple times with identical sample, the absorption peak depth will decrease if the system has not already been saturated. To the latter point, Figures 3.9-3.12 showcase the effect of sequential half hour evacuations of an ICLAS system containing a 3 m HC-PCF gas cell with 0.5% acetylene. The legend notation indicates the number of half hour evacuations performed (f1, f2, and f3 correspond to one, two, and three flushes respectively), as well as the connection number (NoCon, 1con, 2con, and 3con indicate whether there were zero, one, two, or three ferrule connections present in the HC-PCF gas cell). The word 'thresh' indicates that the measurements were taken with the ICLAS system operating at the threshold condition (there was no laser line).
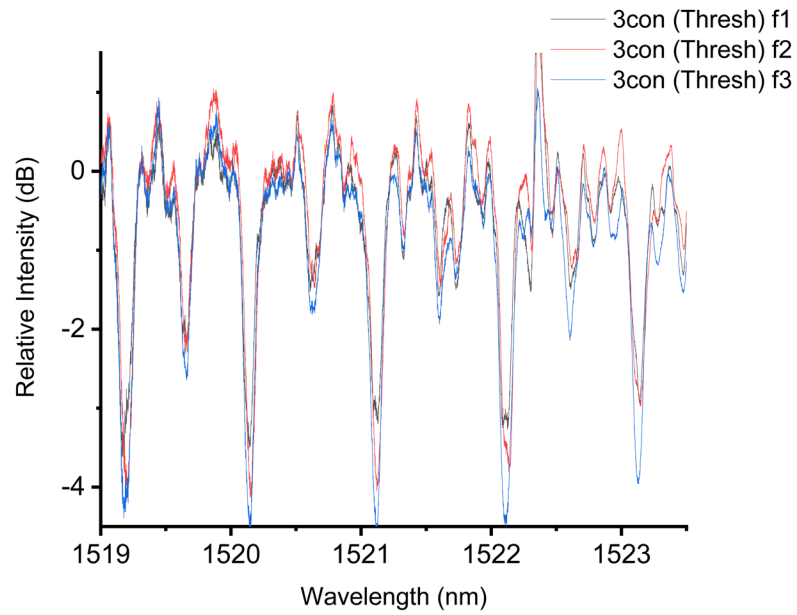
(a)
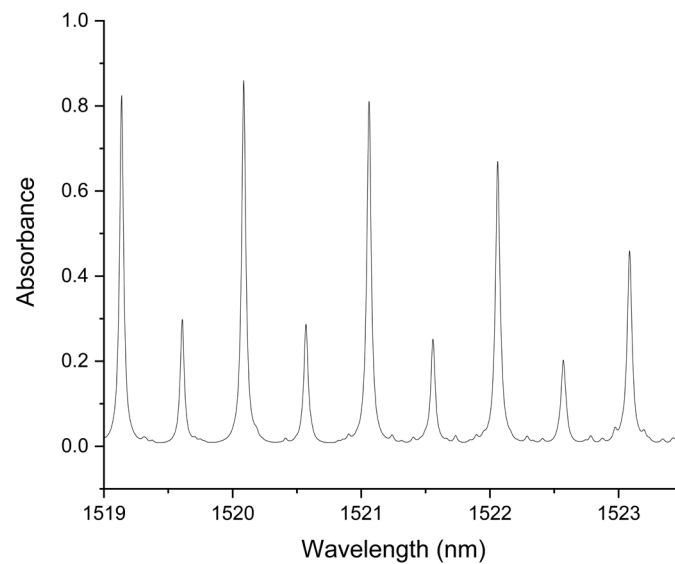
(b)

Figure 3.9: Absorption spectra of 0.5% (5000 ppm) acetylene (a) 3 m Segmented HC-PCF gas cell with three ferrule connections, and (b) simulated output assuming a 3 m path length.

66
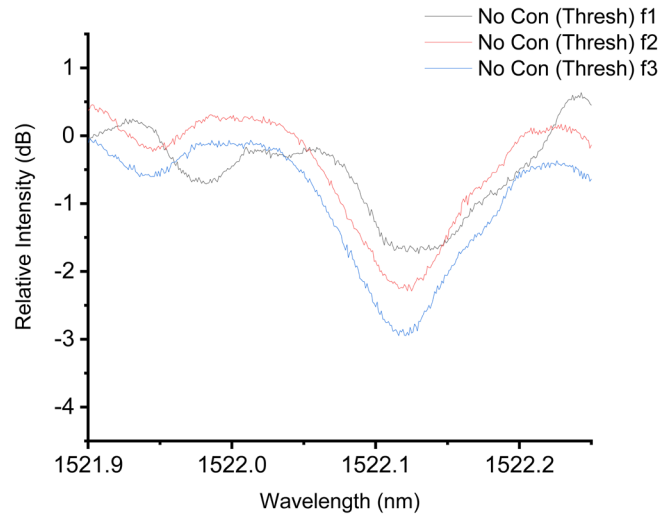
(a)
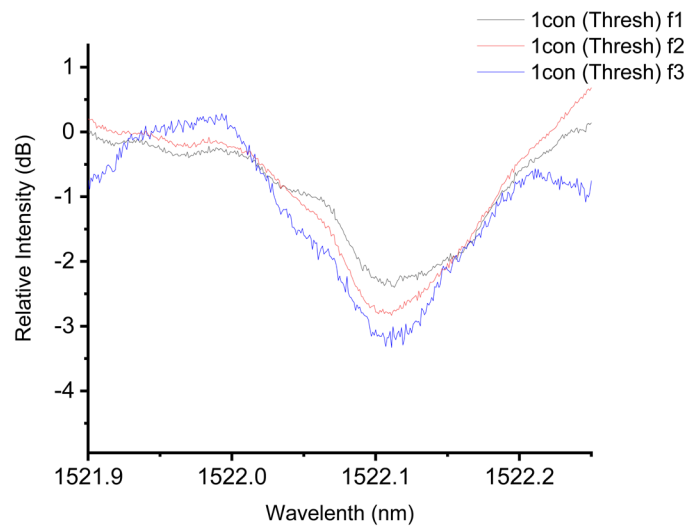
(b)
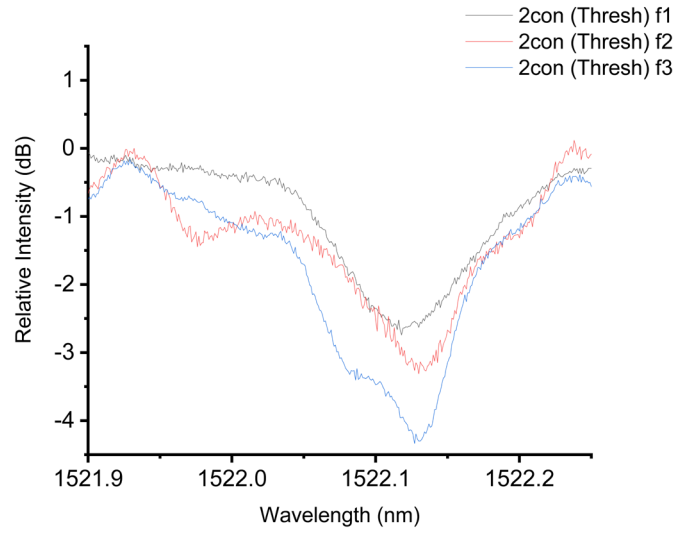
(c)
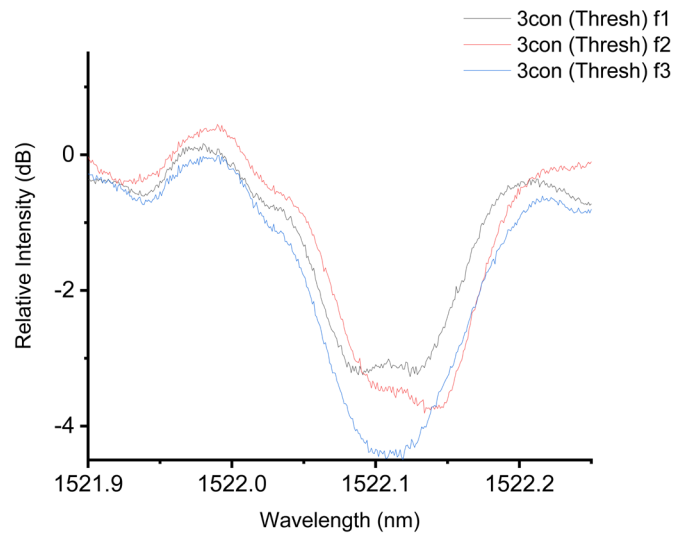
(d)

Figure 3.10: A particular ro-vibrational absorption line is highlighted for three consecutive flushes of 5000 ppm acetylene for a 3 m HC-PCF gas cell with zero, one, two, and three ferrule connections displayed in figures a, b, c, and d, respectively.
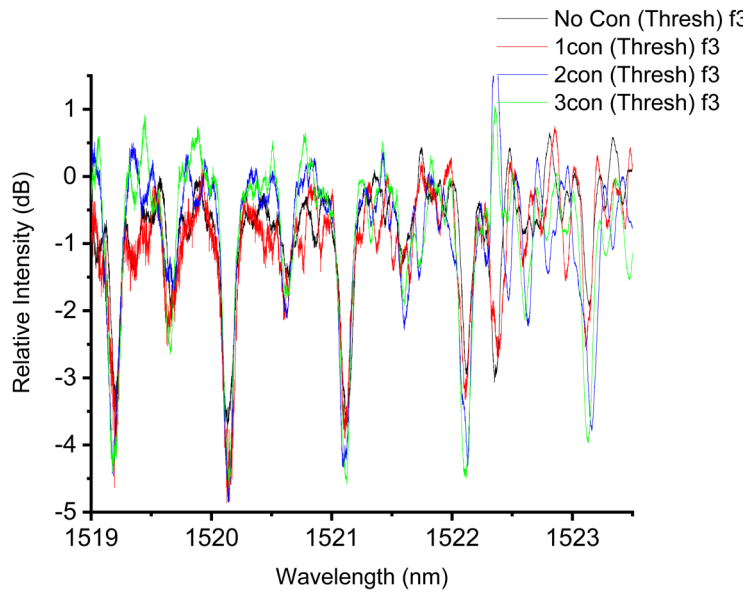
(a)
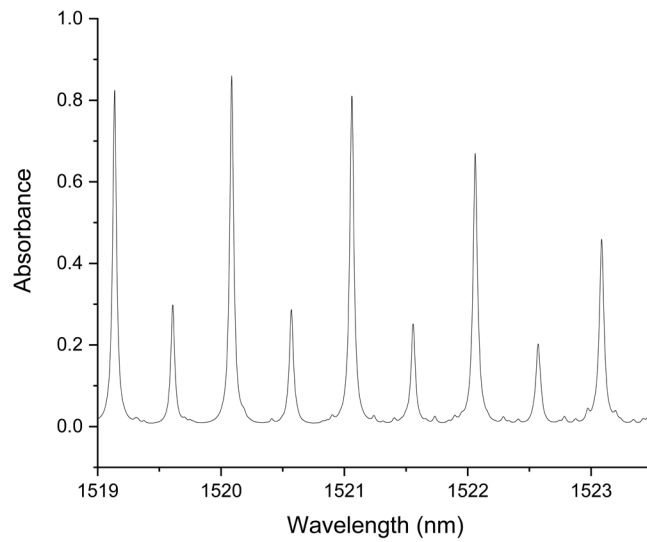
(b)

Figure 3.11: Absorption spectra of 5000 ppm acetylene (a) 3 m HC-PCF gas cell with either zero, one, two, or three ferrule connections, for the third half hour evacuation of acetylene, and (b): simulated output assuming a 3 m path length.
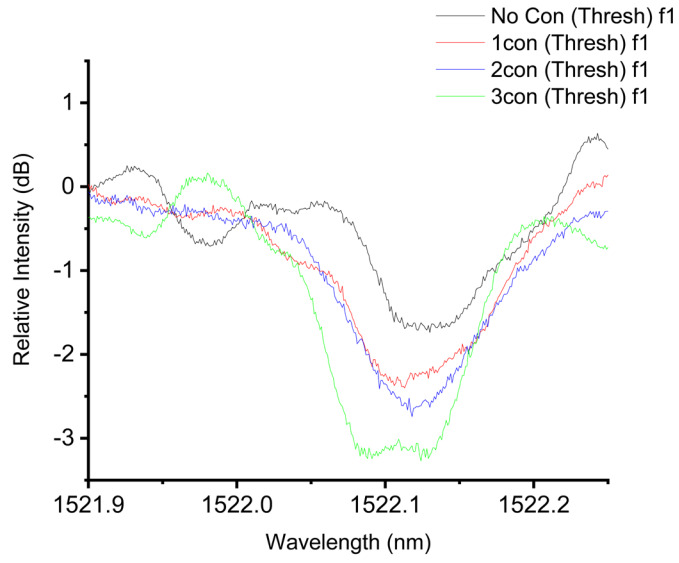
(a)
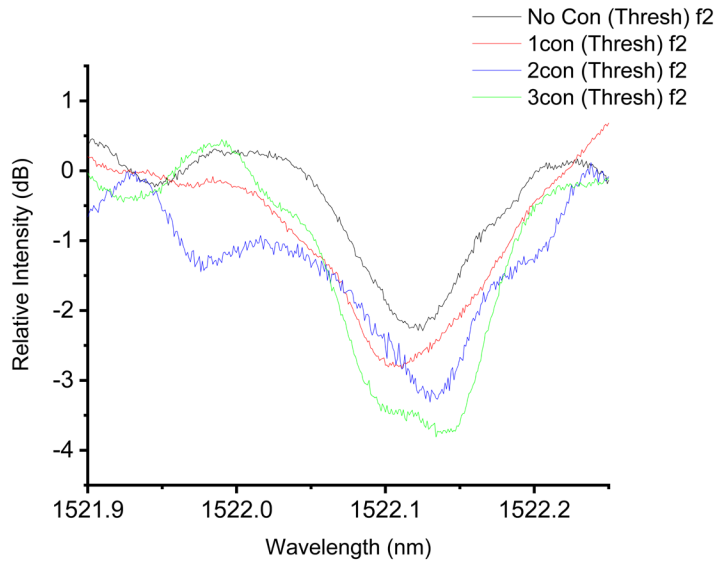
(b)
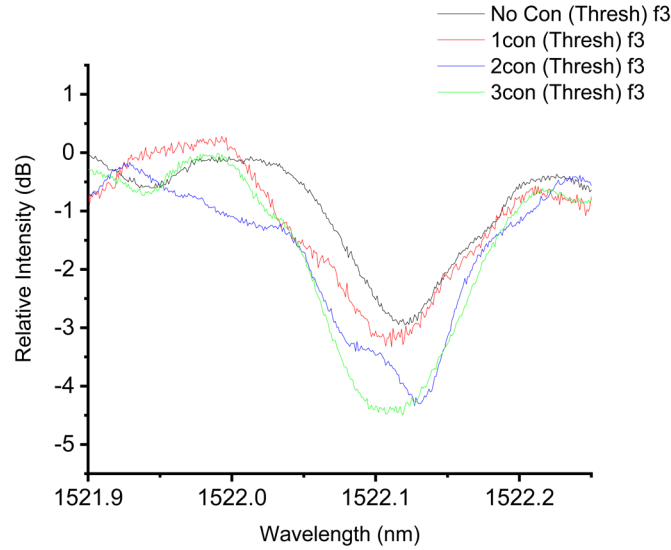
(c)

Figure 3.12: Absorption spectra of 5000 ppm acetylene gas in a 3 m HC-PCF gas cell with either zero, one, two, or three ferrule connections, displaying a particular ro-vibrational absorption line for the first, second, and third half hour evacuations (a, b, and c respectively).

It can be observed in Figures 3.9 and 3.10 that as the number of ferrule connections remains constant, and the number of sample evacuations increases, the overall absorption peak depth continues to improve. This implies that the HC-PCF gas cell has not been saturated with sample during the previous evacuation. In order to improve the responsivity of the system, a more efficient way of filling the gas cell is required. The effects of increasing numbers of ferrule connections can be observed in Figures 3.11 and 3.12. Generally speaking, as the number of ferrule connections increases, the overall absorption depth improves. As can be seen in the figures, the gas cell with no ferrule connectors has the shallowest absorption peak, and each subsequent connector provides

71

some enhancement. This enhancement continues until the third sequential evacuation with 5000 ppm acetylene, where the HC-PCF cell with both two and three ferrule connections appears to be nearing the same depth, even though the peak shape is malformed for the situation with two connectors. The argument for this is that the benefit of having multiple ferrule connectors decreases as the overall evacuation time increases. In other words, the benefit of having multiple access points for the gas to enter the system is mitigated when the gas has ample time to do so in any case.

3.4: Effect of Evacuation Time and Cell Length

In order to more completely investigate the benefits of this particular gas cell development another approach was investigated, where varying sample concentration with varying evacuation time. In the following section, sequential evacuations are no longer considered, as the purpose of designing this system is to reduce the overall time required to saturate the gas cell with sample. Instead, the effect of the particular number of ferrule connections is observed for a range of evacuation times, between each evacuation the system is flushed with nitrogen gas in order to get a clean background for the subsequent sample. Additionally, to ensure that there was no significant cross-contamination, samples with the lowest concentration were always tested first, with higher concentrations being taken in increasing order. The procedure used in order to investigate this was as follows: An eight-meter strand of HC-PCF was used as a gas cell, the absorption of several concentrations (50 ppm, 500 ppm, and 5000 ppm) were investigated across several evacuation times (flush, one minute, ten minutes, thirty minutes, and one hour). The evacuation time denoted as 'flush' indicates that the sample

gas was pulled into the gas chamber without a hard vacuum first being established. After the combination of each concentration and evacuation time was collected, the eight meter strand of HC-PCF was removed, and a two meter section was cleaved off of the end. The remaining six meters was re-coupled into the system, and the same procedure was repeated again. This continued until all that remained was a two- meter strand, which once again had all data collected while coupled into the system. After this, each two meter section which had been cleaved off was subsequently connected back into the system using the ferrule connection method described in a previous section. As each two meter section was connected, all data was once again taken. At the end, the original eight meter gas cell was reconstructed using four two meter segments of HC-PCF, each connected using ferrules as described earlier.

In the following section we will present several observations based on experimental results following the previously established parameters. The first set of figures to be discussed all hold the same length of the HC-PCF gas cell, and vary the evacuation time before sample is allowed to enter the system. The purpose of these figures is to show how the saturation point changes for each cell length, and lay the groundwork for analyzing the next set of figures, where the cells are plotted against each other to compare relative absorption peak depth. To begin with, Figures 3.13 to 3.16 display both an expanded view (1519 to 1523.5nm) for the 'whole' lengths of HC-PCF, in other words the HC-PCF was not segmented, as well as a view focused to one particular absorption peak for each whole length of HC-PCF, with an acetylene concentration of 5000 ppm.
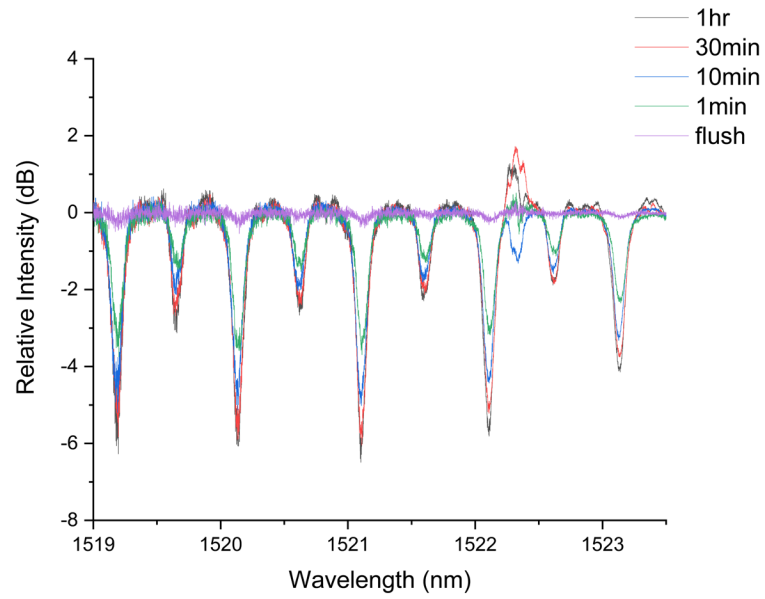
(a)
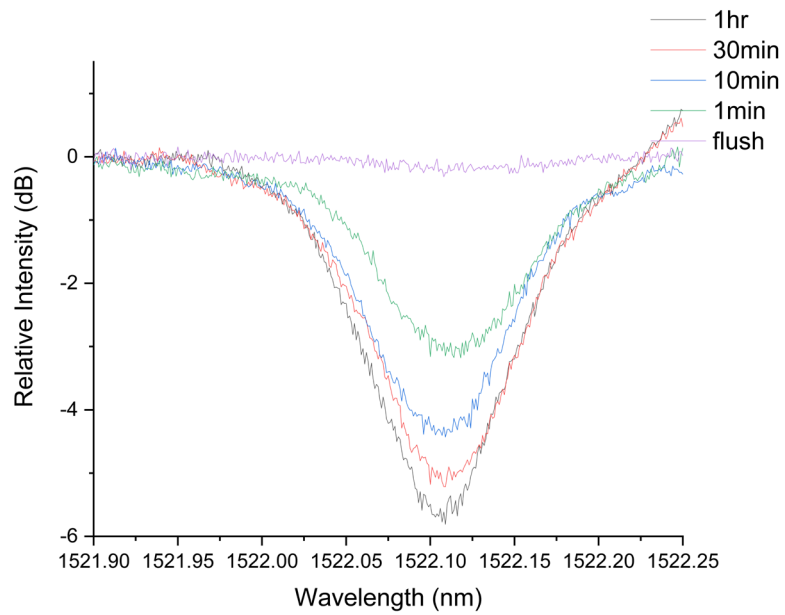
(b)

Figure 3.13: Absorption peaks obtained with an 8 m long HC-PCF gas cell, (a) over a range of wavelength, and (b) a particular absorption line, using acetylene at 5000 ppm as the sample.

(a)

(b)

Figure 3.14: Absorption peaks obtained with a 6 m long HC-PCF gas cell, (a) over a range of wavelength, and (b) a particular absorption line, using acetylene at 5000 ppm as the sample.

(a)

(b)

Figure 3.15: Absorption peaks obtained with a 4 m long HC-PCF gas cell, (a) over a range of wavelength, and (b) a particular absorption line, using acetylene at 5000 ppm as the sample.
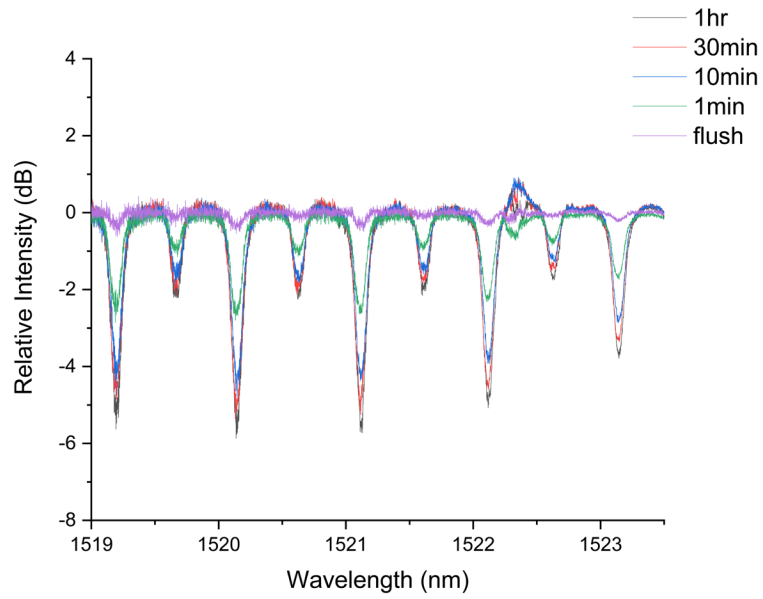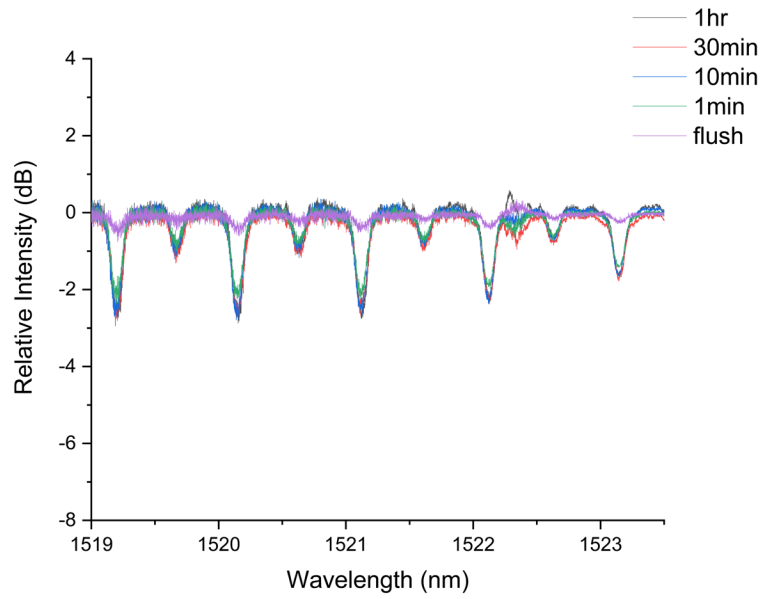
(a)
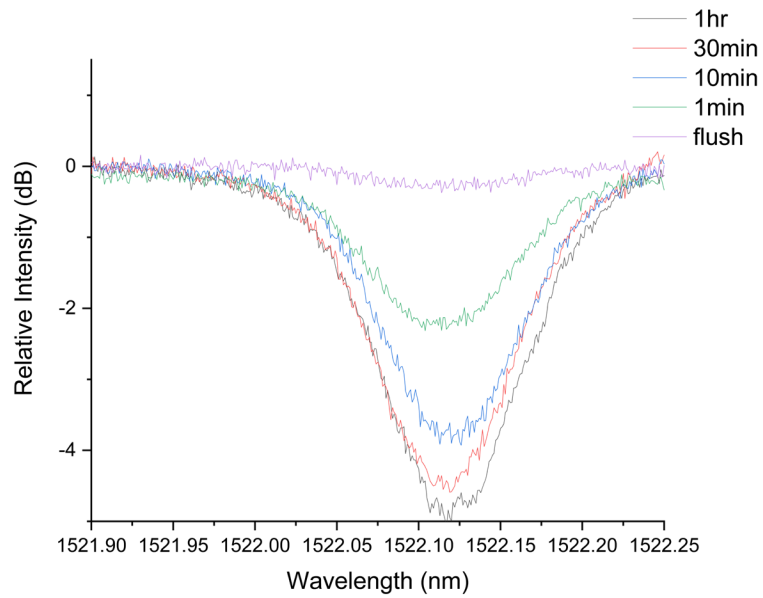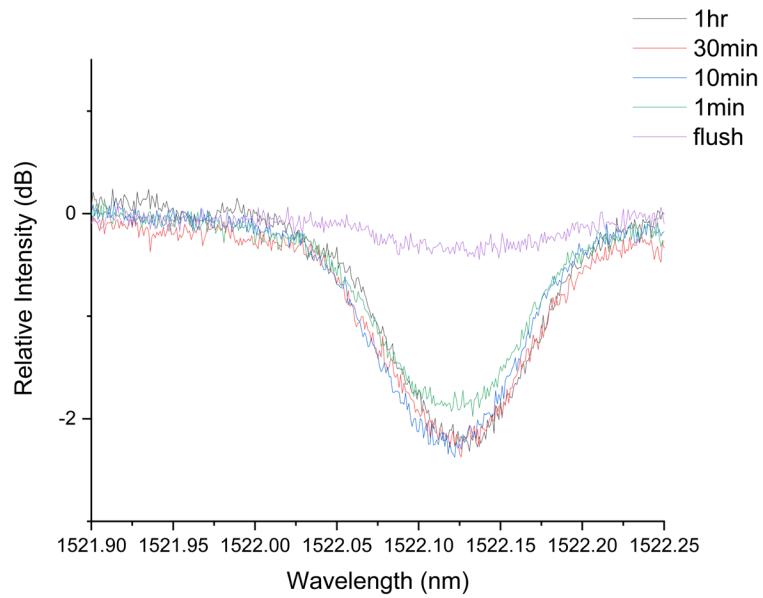

(b)

Figure 3.16: Absorption peaks obtained with a 2 m long HC-PCF gas cell, (a) over a range of wavelength, and (b) a particular absorption line, using acetylene at 5000 ppm as the sample.
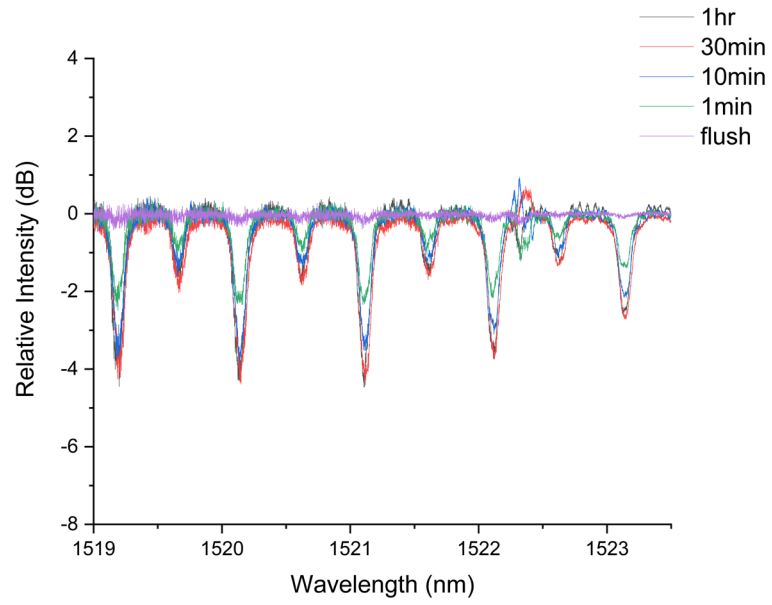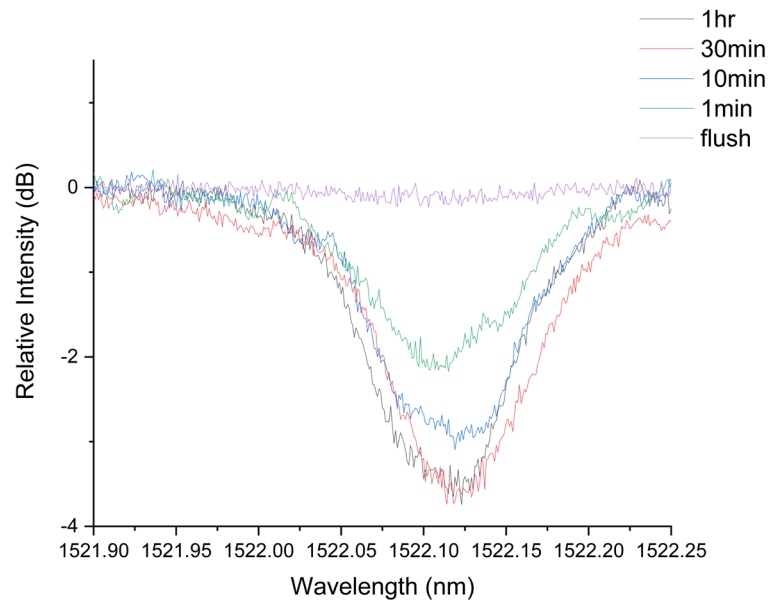
The wavelength range for the absorption spectra of the above figures has been kept consistent with those from the previous section in order to allow for an easy comparison between the different sets of results. As can be seen in both the expanded view provided in the above figures, and more clearly in the focused view of a particular absorption line, there is a clear relation between the absorption peak depths and the evacuation time when it comes to the 8 m HC-PCF gas cell length. As the evacuation time increases, the depth of the absorption peak improves. This relation holds for the 6 m HC-PCF gas cell as well. However, it can be observed that the relative difference between the absorption peak depths, especially for the 30 min and 1 hr evacuation times, decreases. This becomes even more apparent when observing the 4 m cell, where the 30 min and 1 hr evacuation times are essentially identical, and when one finally observes the 2 m cell, all three of the 1 hr, 30 min, and 10 min evacuation times coincide, with a clear separation from the 1 min evacuation time, and the cell flush (which was performed by simply allowing the sample to flow through the enclosure without creating a vacuum). What this implies is that for a segment length of two meters, an evacuation time of ten minutes should be the same as an evacuation time of one hour, which means that the overall system's responsivity should be greatly improved. In order to showcase this, Figures 3.17 to 3.20 display the wide view and close up view of the absorption spectra of acetylene under the same conditions as in the previous examples, the only difference being that the gas cells are constructed out of 2 m segments of HC-PCF to make up overall length of the gas cell.
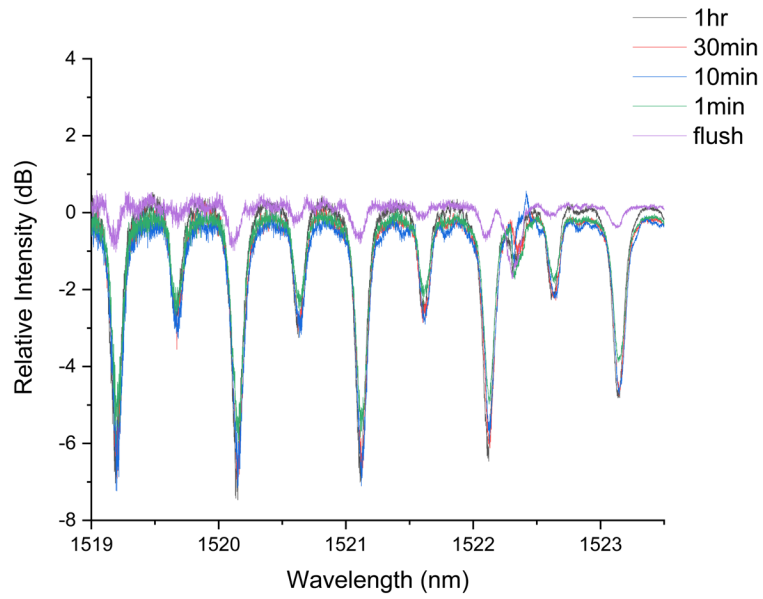
(a)
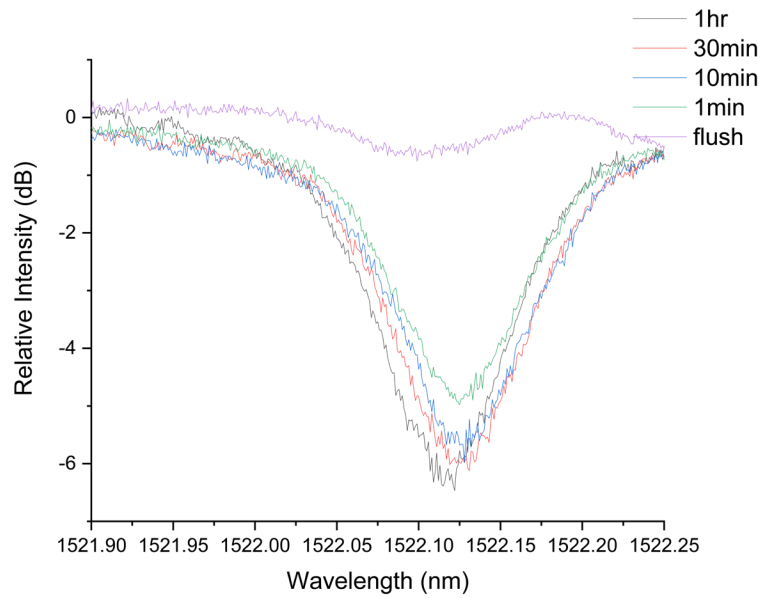
(b)

Figure 3.17: Absorption peaks obtained with 10 m (five 2 m segments) long HC-PCF gas cell, (a) over a wide wavelength range, and (b) at a particular absorption line, using 5000 ppm acetylene gas.
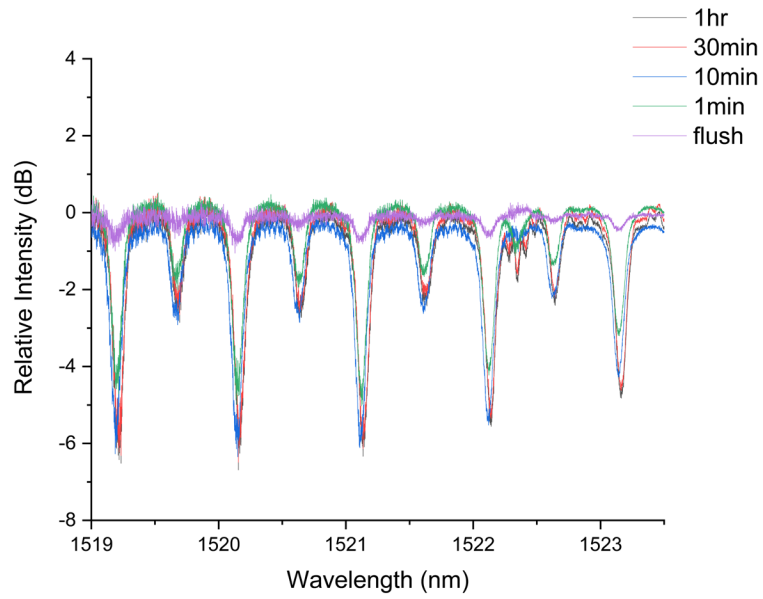
(a)
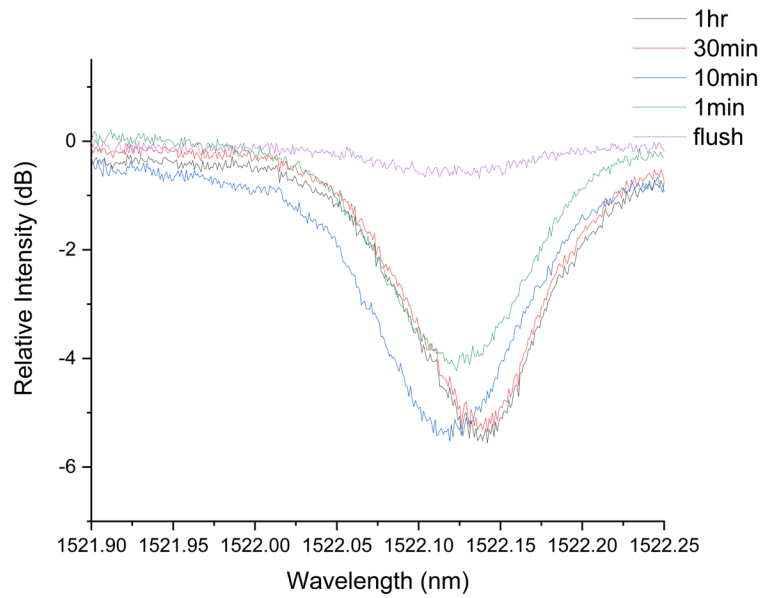
(b)

Figure 3.18: Absorption peaks obtained with 8 m (four 2 m segments) long HC-PCF gas cell, (a) over a wide wavelength range, and (b) at a particular absorption line, using 5000 ppm acetylene gas
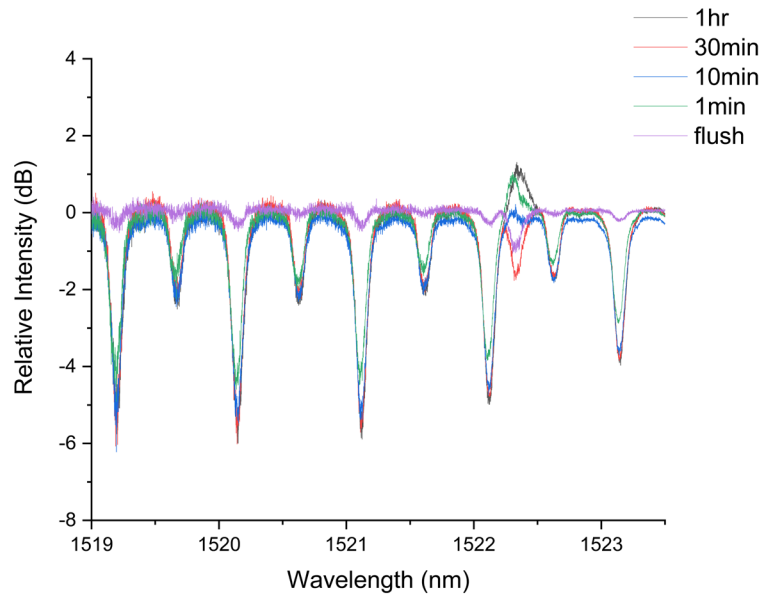
(a)
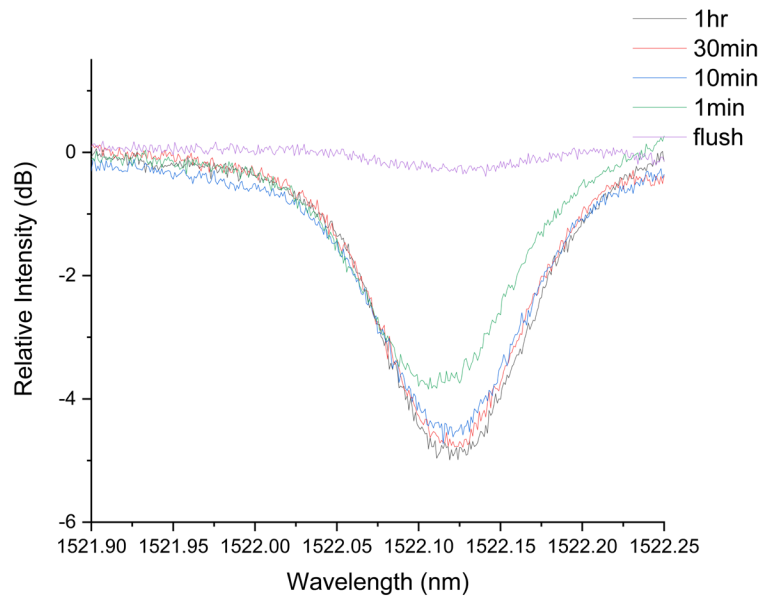
(b)

Figure 3.19: Absorption peaks obtained with 6 m (three 2 m segments) long HC-PCF gas cell, (a) over a wide wavelength range, and (b) at a particular absorption line, using 5000 ppm acetylene gas.
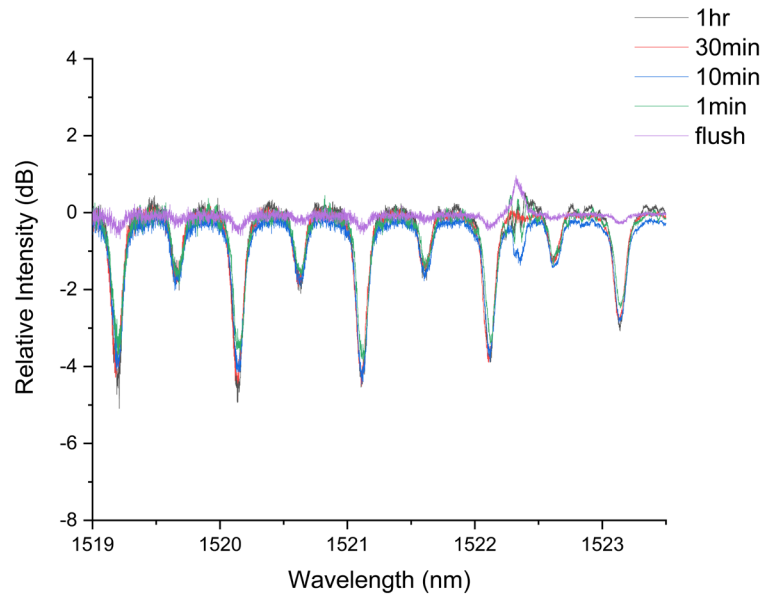
(a)
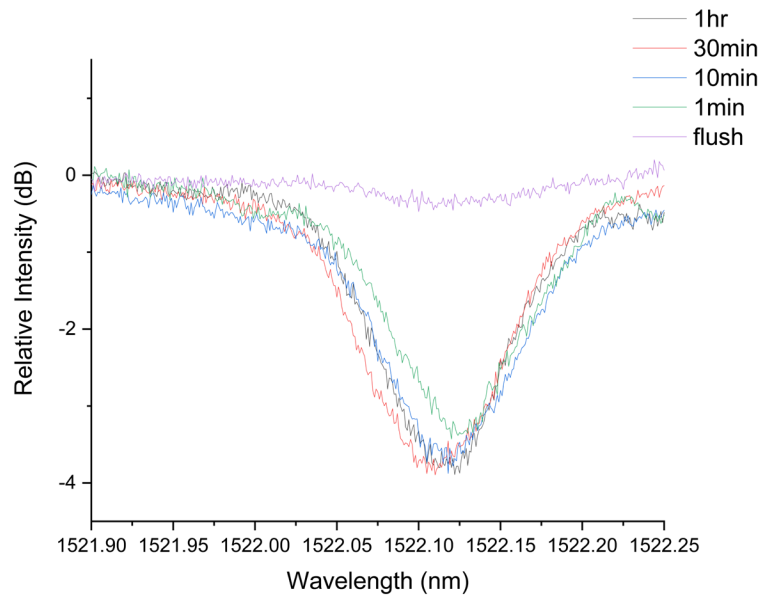
(b)

Figure 3.20: Absorption peaks obtained with 4 m (two 2 m segments) long HC-PCF gas cell, (a) over a wide wavelength range, and (b) at a particular absorption line, using 5000 ppm acetylene gas.

As can be observed in the above Figures (3.17 to 3.20), the segmentation has caused the absorption peak depths to come together for evacuation times of 1 hr, 30 min, and 10 min, the largest disparity between these times is seen for the 10 m, 4 connectors HC-PCF cell seen in Figure 3.17, however even these small variations in intensity are a significant improvement upon the whole length HC-PCF examples shown in Figures 3.13 to 3.16. The 1 min evacuation time remains separated, just as was observed previously, implying that a 2 m length of HC-PCF is still not fully evacuated after 1 min. Smaller segment lengths would lead to a lower evacuation time, however the relative loss of power in each segment would result in large insertion loss when it comes to constructing a longer gas cell out of many connectors. In order to directly compare the benefits of the segmented gas cells, Figures 3.20 to 3.25 will display an expanded view and a focused view of the absorption peak depth for each cell compared to a particular evacuation time.
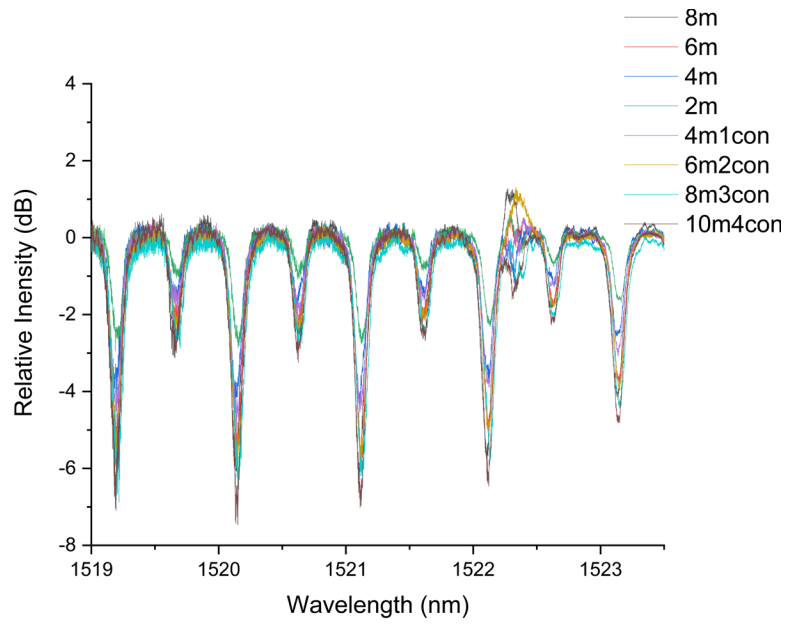
(a)
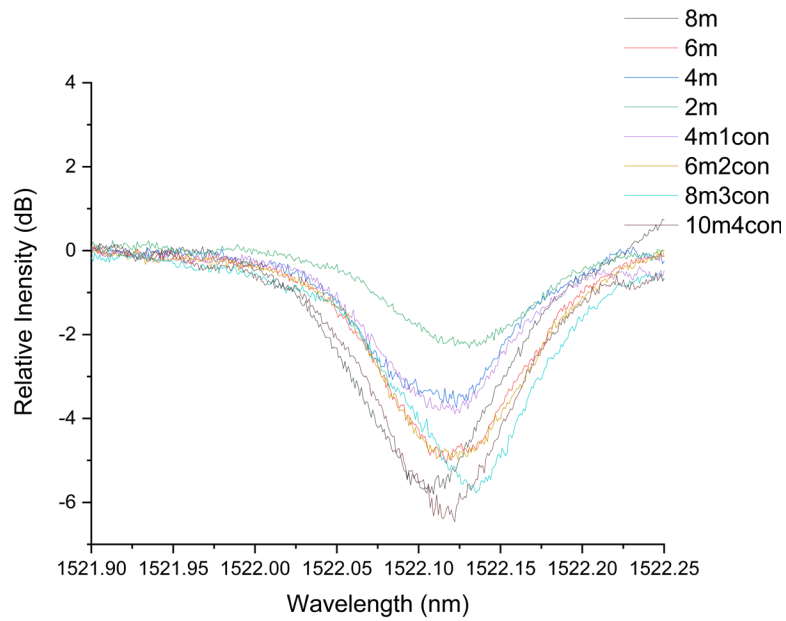
(b)

Figure 3.21: Displaying range of absorption peaks along with a particular absorption peak for HC-PCF gas cells with varying lengths for an evacuation time of 1 hr in (a) and (b), respectively, using 5000 ppm acetylene gas as the sample.
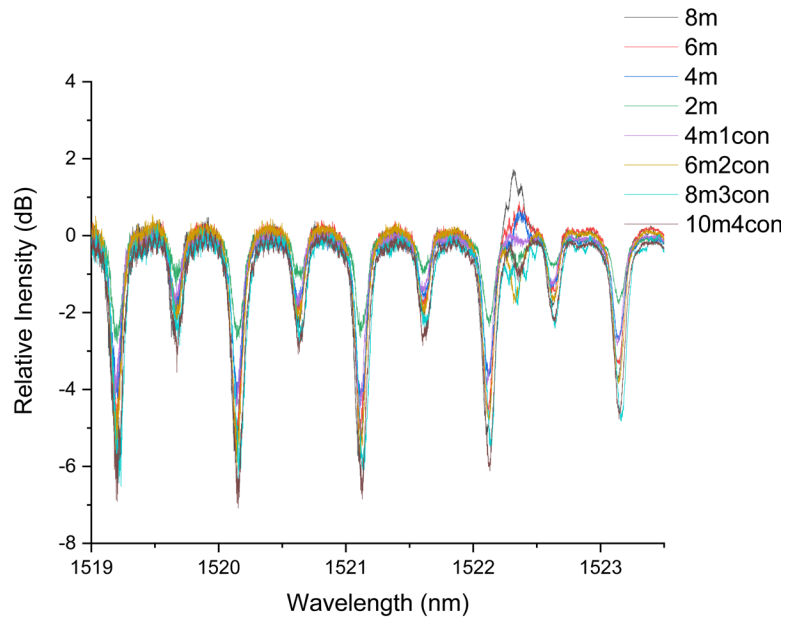
(a)
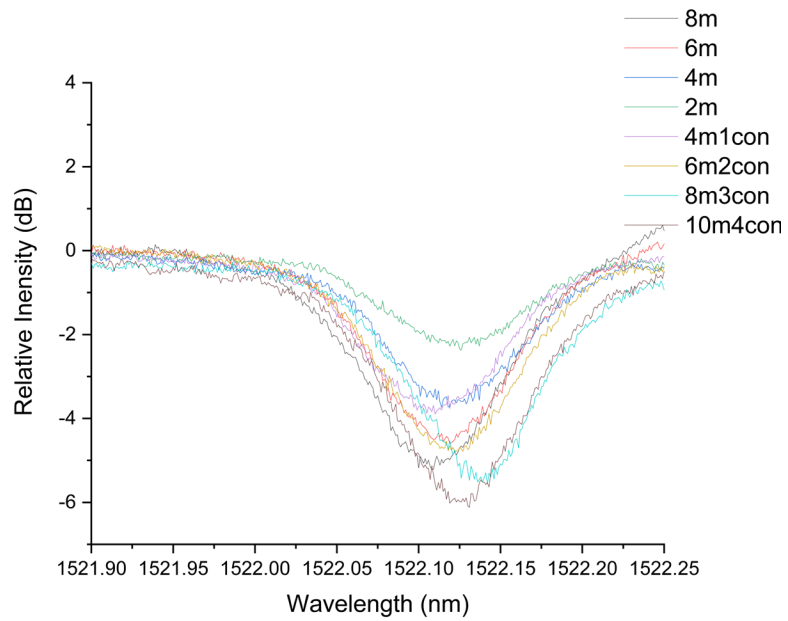
(b)

Figure 3.22: Displaying range of absorption peaks along with a particular absorption peak for HC-PCF gas cells with varying lengths for an evacuation time of 30 min in (a) and (b) respectively, using 5000 ppm acetylene gas as the sample.
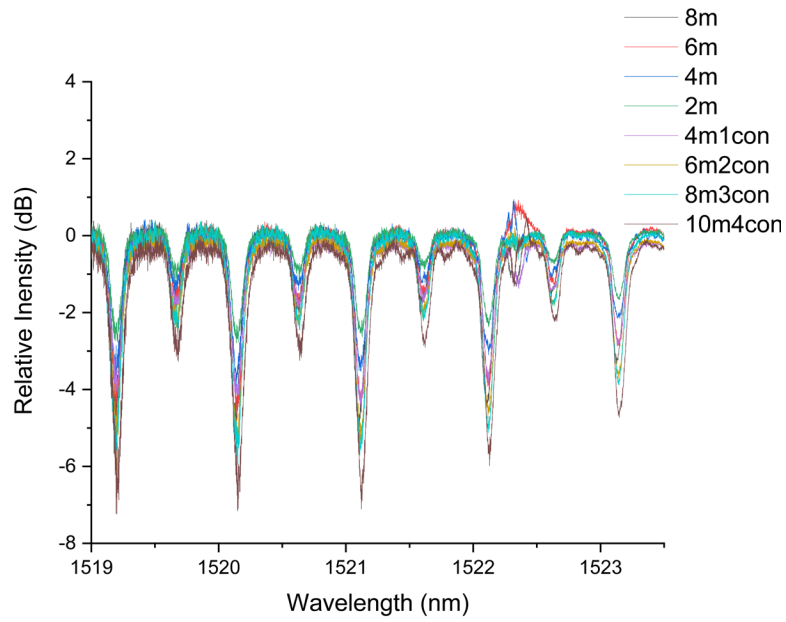
(a)
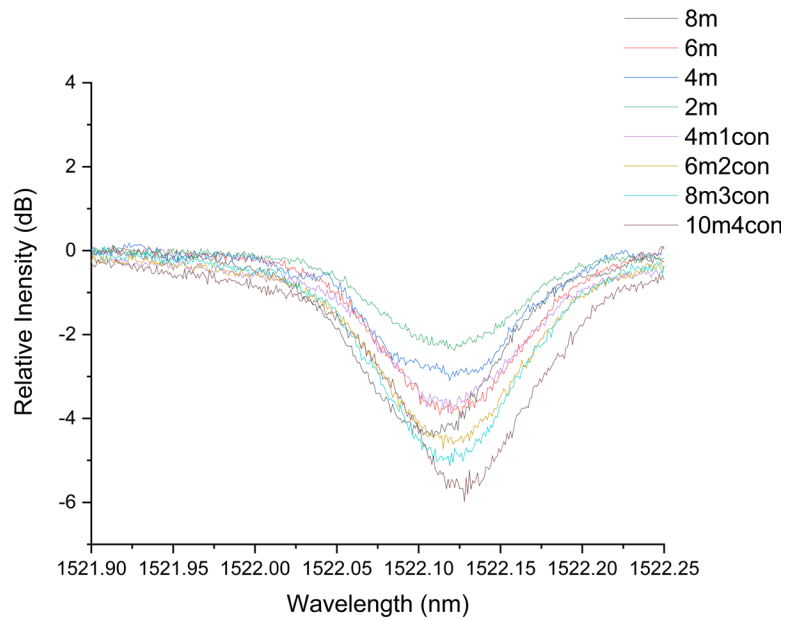
(b)

Figure 3.23: Displaying range of absorption peaks along with a particular absorption peak for HC-PCF gas cells with varying lengths for an evacuation time of 10 min in (a) and (b) respectively, using 5000 ppm acetylene gas as the sample.
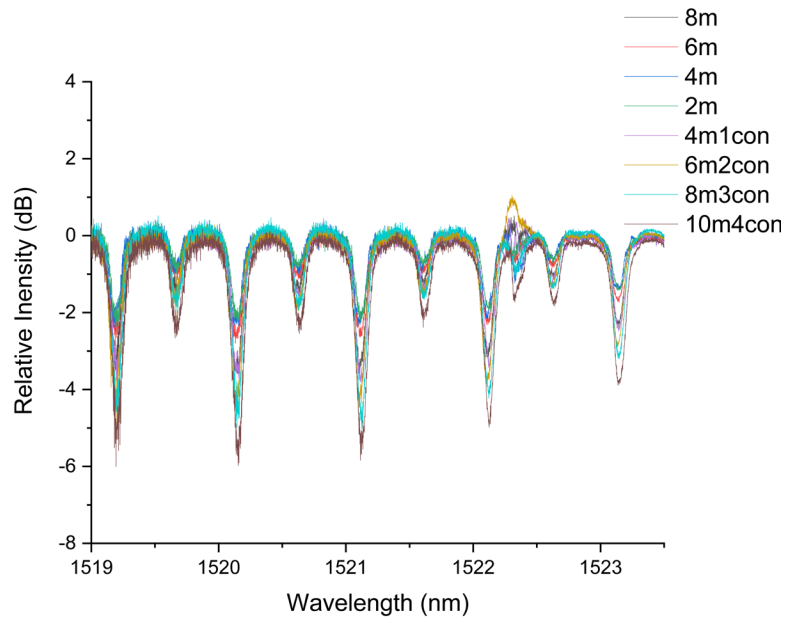
(a)
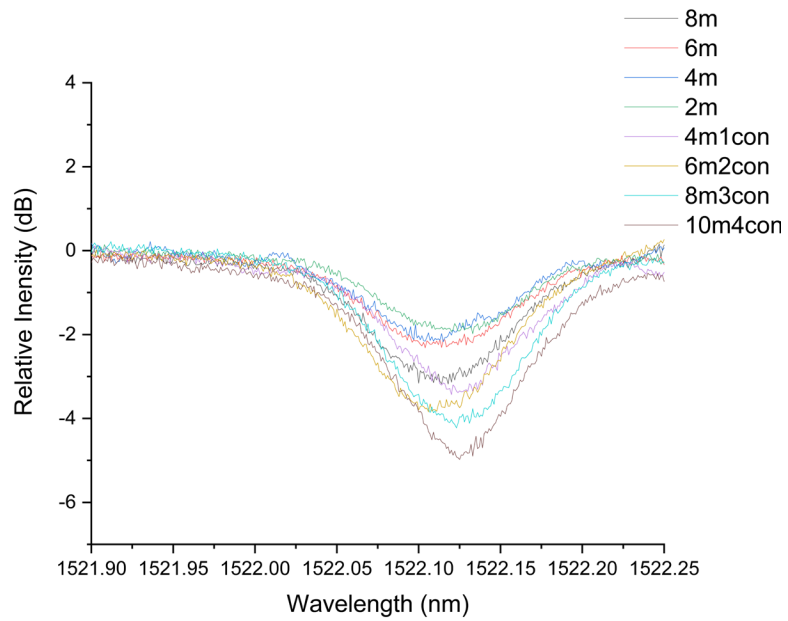
(b)

Figure 3.24: Displaying range of absorption peaks along with a particular absorption peak for HC-PCF gas cells with varying lengths for an evacuation time of 1 min in (a) and (b) respectively, using 5000 ppm acetylene gas as the sample.
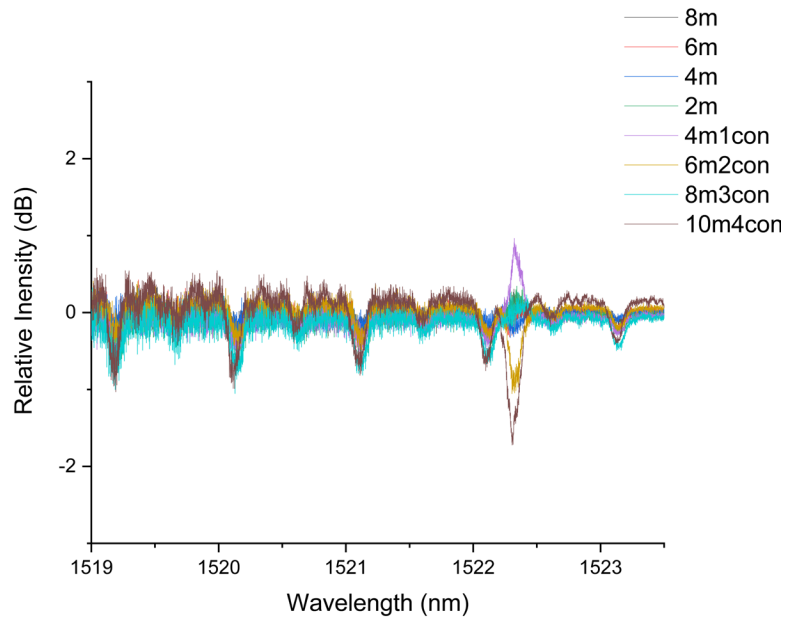
(a)
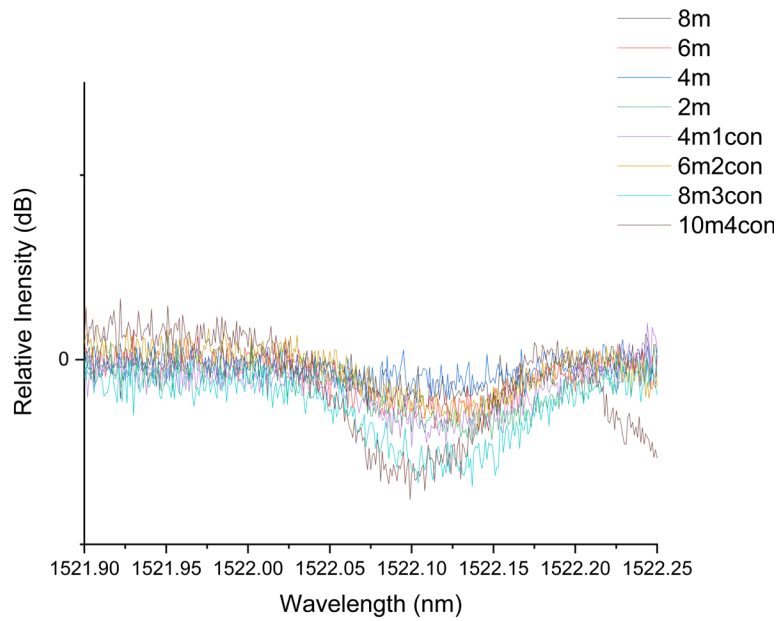
(b)

Figure 3.25: Displaying range of absorption peaks along with a particular absorption peak for HC-PCF gas cells with varying lengths flushed with sample (no extended evacuation) in (a) and (b) respectively, using 5000 ppm acetylene gas as the sample.

As can be seen in the above Figures (3.21 to 3.25), the absorption peak depth is directly dependant on both the length of the gas cell used, as well as the evacuation time of the either un-segmented or segmented HC-PCF. As was expected, at higher evacuation times the relative difference between the segmented and un- segmented HC-PCF cells of the same length had very little difference (Figure 3.21), however the overall cell length played a key role in determining the depth of the absorption peak. As the evacuation time decreased however, the relative peak intensity of the segmented vs un-segmented fibers of the same length began to show a disparity in their respective absorption peak depths (Figure 3.22 to 3.25). Speaking generally, as one decreases the evacuation time, the benefit of segmentation becomes more readily apparent, with a large deviation between what is observed from the un-segmented HC-PCF and the segmented HC-PCF. Investigating Figure 3.22, one can see a small difference between the segmented and un-segmented gas cells of the same length, and as the evacuation time decrease further this separation becomes significant. Speaking specifically about Figure 3.24, which showcases the 1 min evacuation time of the HC-PCF gas cells, one can observe that even a 4 m cell composed of two 2 m segments has a deeper absorption peak than the 8 m un-segmented gas cell. These figures clearly show the benefits of segmentation when it comes to building a more responsive system. Though the segmentation does nothing for improving the sensitivity if evacuation time is not a concern, when a faster response is required, it is invaluable. Another good example can be found in Figure 3.25, and although the spectra is messy due to how low the signal is, it is still clear that when the system is simply flushed with gas, the only HC-PCF gas cells which show significant signal are the larger segmented ones, where all the others are close to the noise level.

The following section will display the benefits of HC-PCF segmentation by showcasing how the limit of detection improves when the evacuation time is limited. The concentration of acetylene was decreased by a factor of ten to 500 ppm, and results were tabulated in the same format as has been seen in the previous figures. A selection of these results will be displayed in Figures 3.26 to 3.30 in order to demonstrate that the trend observed for 5000 ppm concentration holds at 500 ppm.
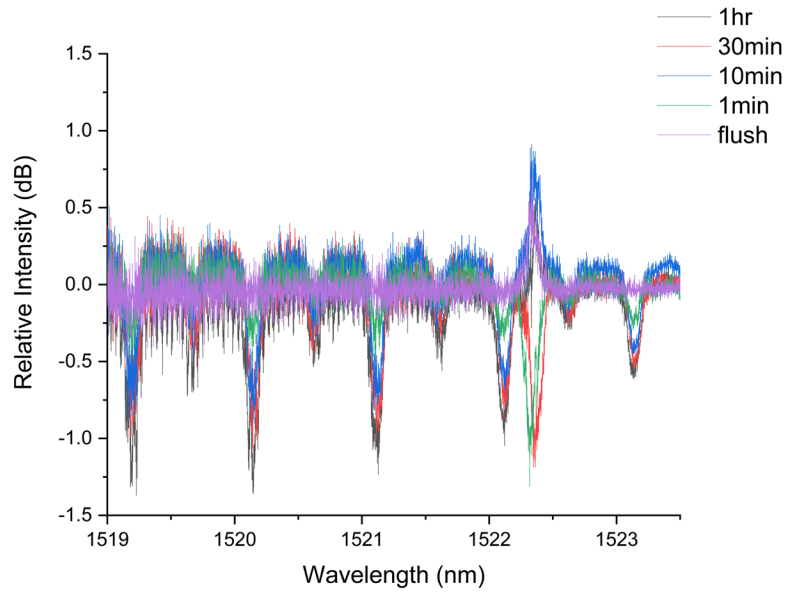
(a)
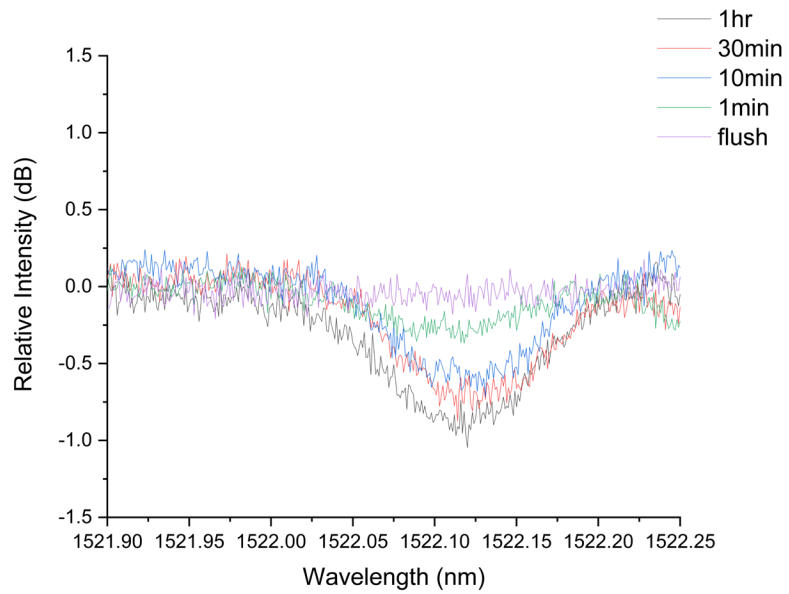
(b)

Figure 3.26: Displaying a range of absorption peaks for a 8 m long HC-PCF gas cell as well as a particular absorption line in (a) and (b) respectively, using 500 ppm acetylene gas as the sample.
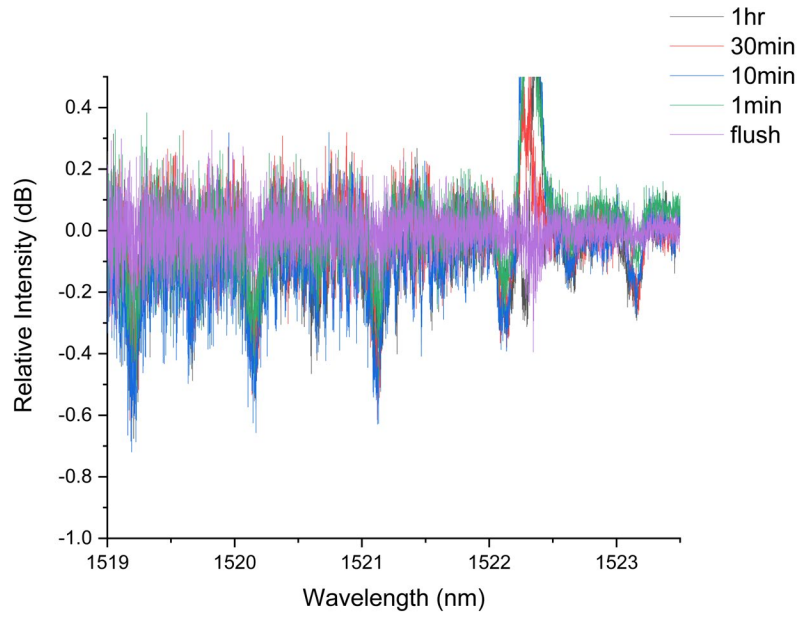
(a)
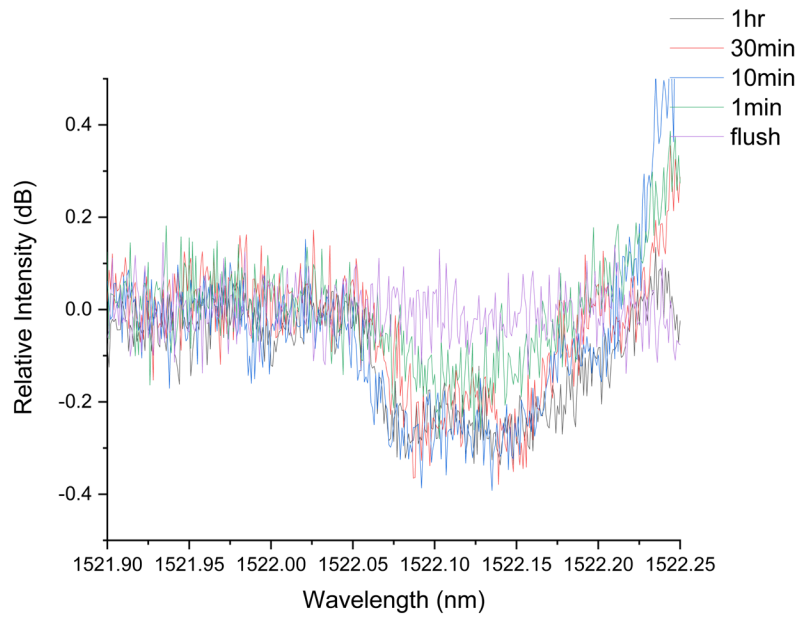
(b)

Figure 3.27: Displaying a range of absorption peaks for a 2 m long HC-PCF gas cell as well as a particular absorption line in (a) and (b) respectively, using 500 ppm acetylene gas as the sample.
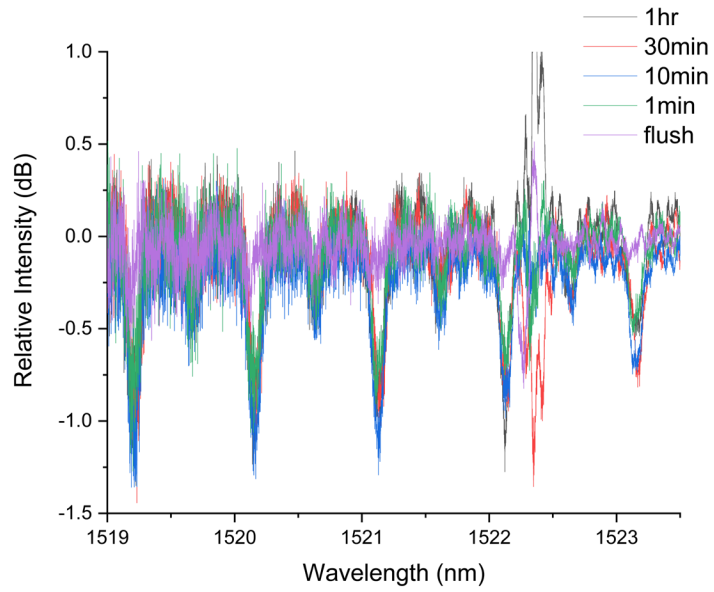
(a)
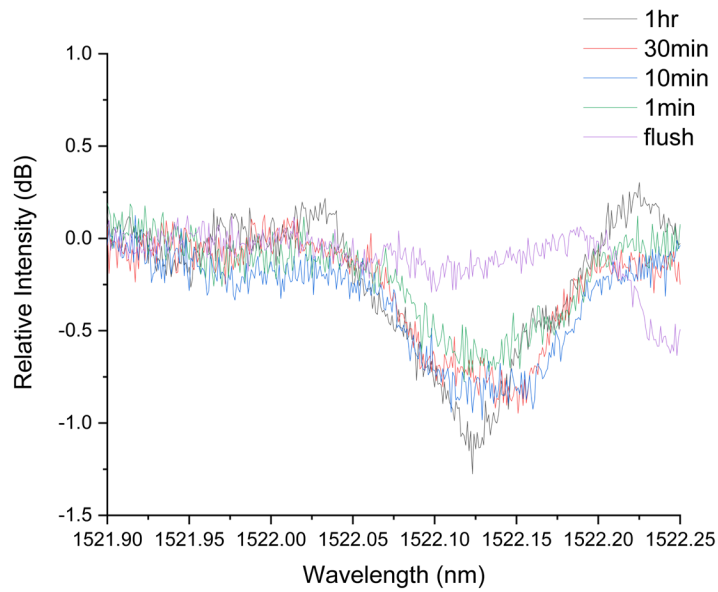
(b)

Figure 3.28: Displaying a range of absorption peaks for a 10 m (made of five 2 m segments) long HC-PCF gas cell as well as a particular absorption line in (a) and (b) respectively, using 500 ppm acetylene gas as the sample.
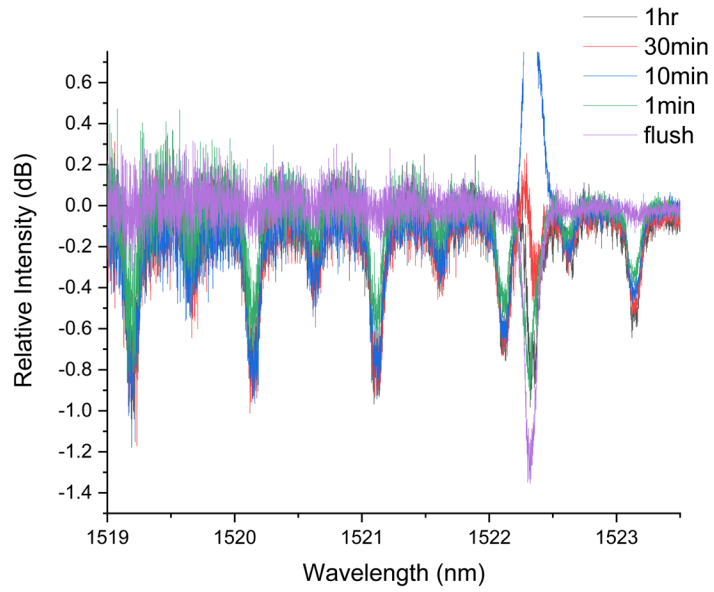
(a)
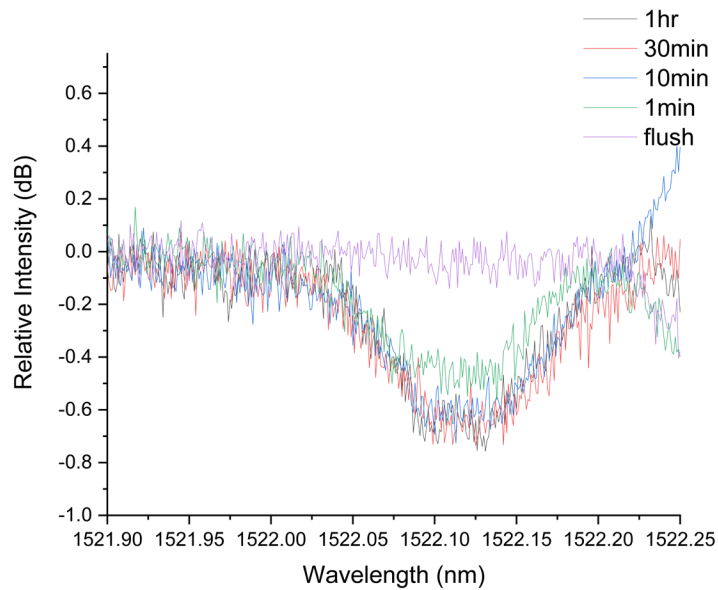
(b)

Figure 3.29: Displaying a range of absorption peaks for a 6 m (made of three 2 m segments) long HC-PCF gas cell with length 6 m as well as a particular absorption line in (a) and (b) respectively, using 500 ppm acetylene gas as the sample.
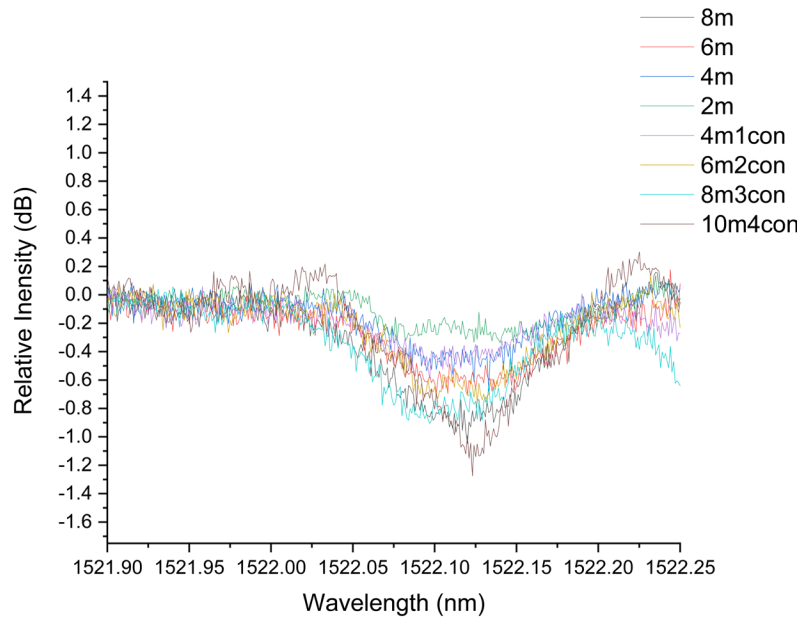
(a)
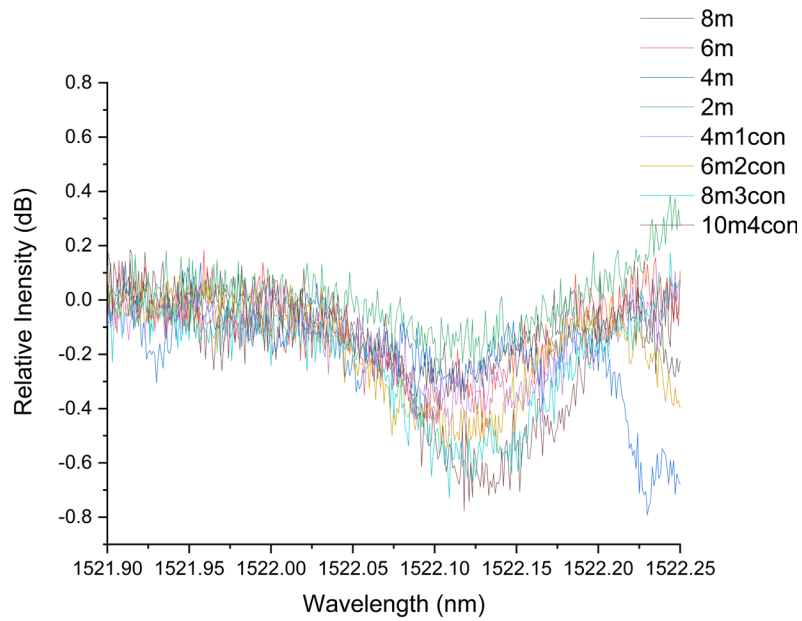
(b)

Figure 3.30: Displaying a specific absorption peak for both 1 hr (a) and 1 min (b) evacuations of all HC-PCF gas cell lengths for 500 ppm concentration of acetylene.

Figure 3.26 shows that for a longer un-segmented length of HC-PCF, the relative absorption peak depth continuously improves as the evacuation time is increased, without converging within this time frame. Figure 3.27 shows once again that at a length of 2 m, the relative absorption peak depth becomes the same for an evacuation time at or above 10 min, with 1 min still not fully evacuating the HC-PCF gas cell. Figures 3.28 and 3.29 both show that the segmented fiber behaves in the same manner as was observed previously, in that the observed absorption peak depth comes to the same level for evacuations at or above 10 min, just as was observed for the 2 m HC-PCF in this section, and as was seen in the results for 5000 ppm acetylene in the previous section. Figure 3.30 (a) once again shows how cells of similar length have similar absorption peak depth whether they are segmented or un-segmented when the evacuation time is high (1 hr), and Figure 3.30 (b) shows that there is a significant disparity between the segmented and un-segmented fibers of the same length when the evacuation time is low (1 min).

Once again, the concentration was reduced by a factor of ten to 50 ppm, and the data was tabulated in the same was as has been seen previously. The difference in this section is that the only cell capable of detecting this particular concentration was the 10 m cell made up of five 2 m segments.
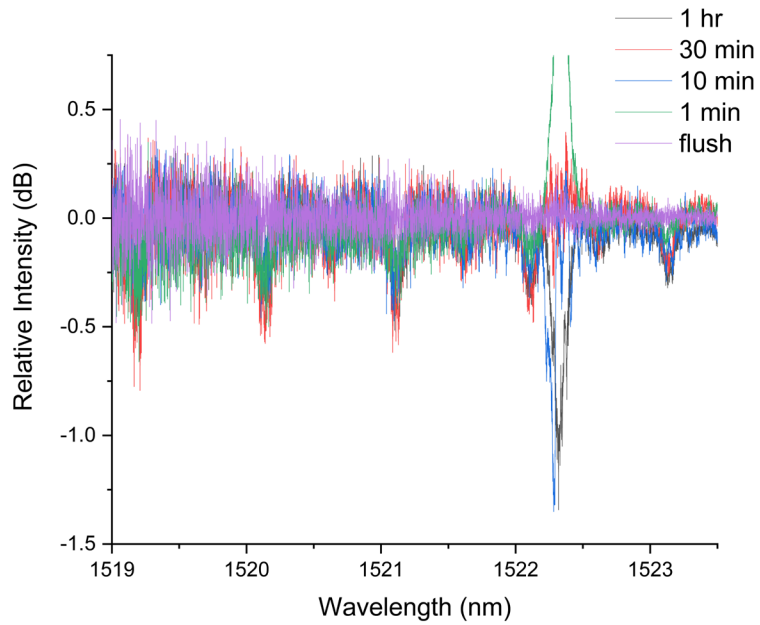
(a)
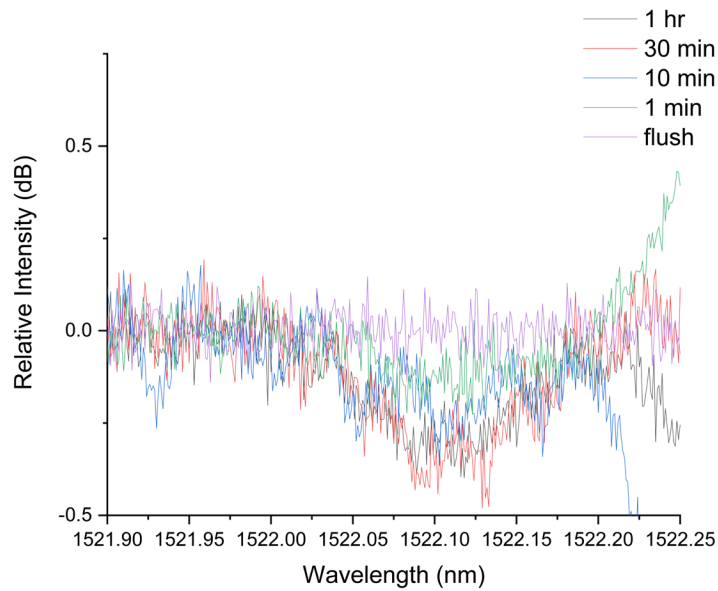
(b)

Figure 3.31: Displays (a) a wide view and (b) a particular absorption peak for a 10 m (made of five 2 m segments) HC-PCF gas cell collected for 50 ppm acetylene gas.
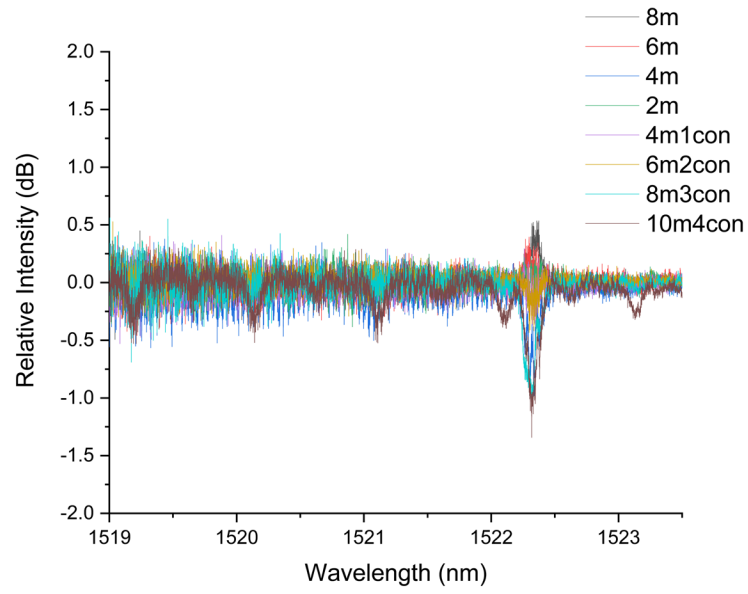
(a)
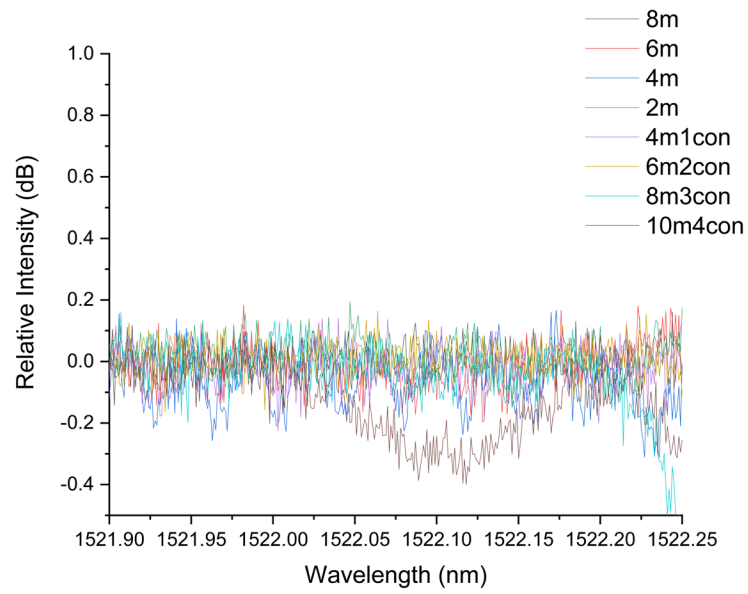
(b)
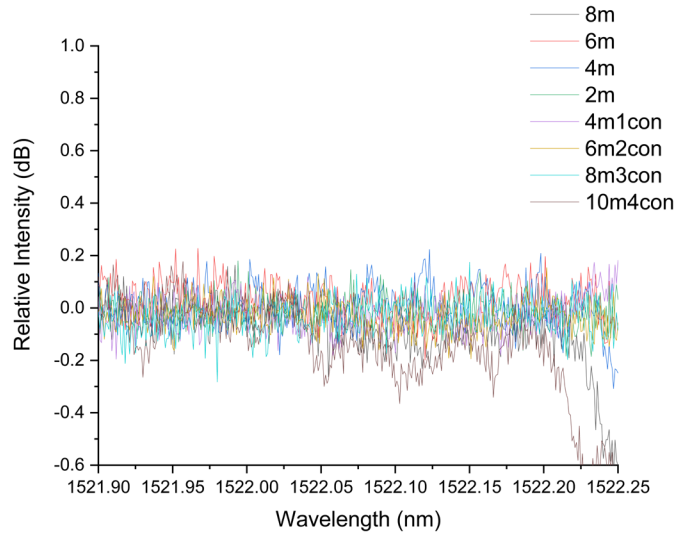
(c)
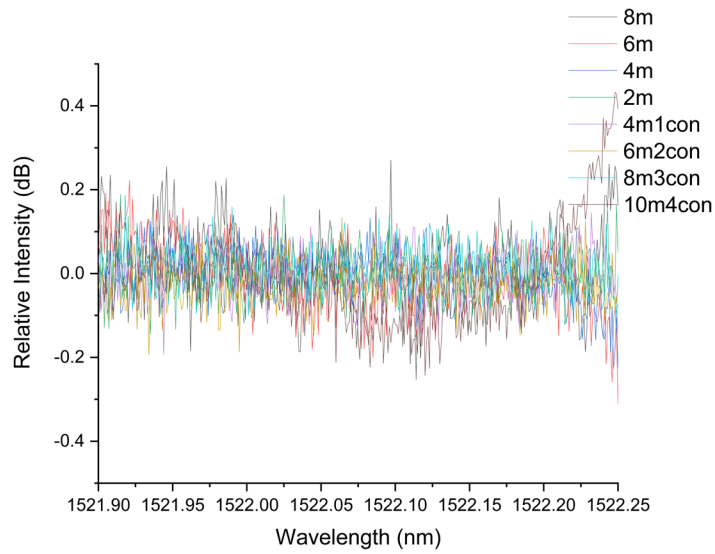
(d)

Figure 3.32: Displaying a wide view of several absorption peaks for a 1 hr evacuation time of each HC-PCF gas cell in (a), and a close up of a particular absorption peak in (b). Additionally, displaying a particular absorption peak after a 10 min and 1 min evacuation in (c) and (d) respectively. All data was collected for 50 ppm acetylene gas.

Figure 3.31 (a) and (b) show that 50 ppm acetylene can be detected by a 10 m segmented HC-PCF gas cell whereas it is undetectable by the cells with a smaller length. The benefit of this particular type of cell is that it is modular, and if a more refined detection limit is required, another segment or segments of HC-PCF can be added. This is important due to the current cost of HC-PCF, which is by far the most expensive component contained within the system, excluding the laser source and the detector of course. Figure 3.32 showcases the detection limit of the HC-PCF gas cell in terms of the evacuation time. Although some signal may be observable after 1 min (Figure 3.32 (d)) it is not easily differentiated from the background noise observed in the other lengths of HC-PCF plotted within the same figure.

Figure 3.33 highlights the effect of segmentation more quantitatively by utilizing an asymptotic fit on the relation between the relative peak depth of a particular absorption line and the evacuation time of the cell. As can be seen when comparing Figure 3.33 (a) and (b), there is a clear saturation of the cell in the case of the segmented fiber, whereas the unsegmented cell shows a steady improvement in the absorption line depth for each increase in evacuation time. This implies that the cell was never completely saturated in the unsegmented case, and an even longer evacuation time would be required if system saturation was to be achieved. In other words, by utilizing the segmented gas cell we don't need to evacuate and fill the gas cell for hours in order to saturate it (as with an unsegmented cell of a similar length); it can be done in a matter of minutes. This is an excellent advantage of the cell, as one can increase the number of connectors and thus lower the response time.
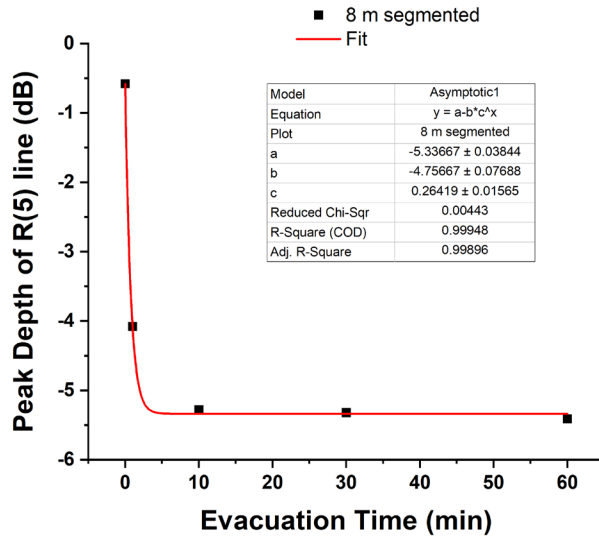
(a)
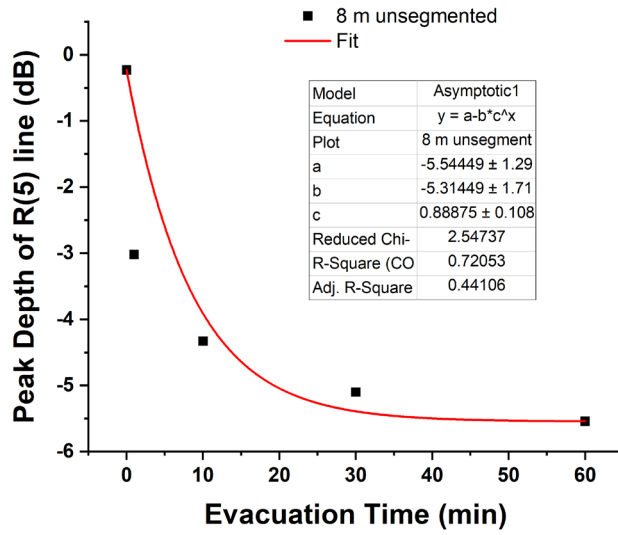
(b)
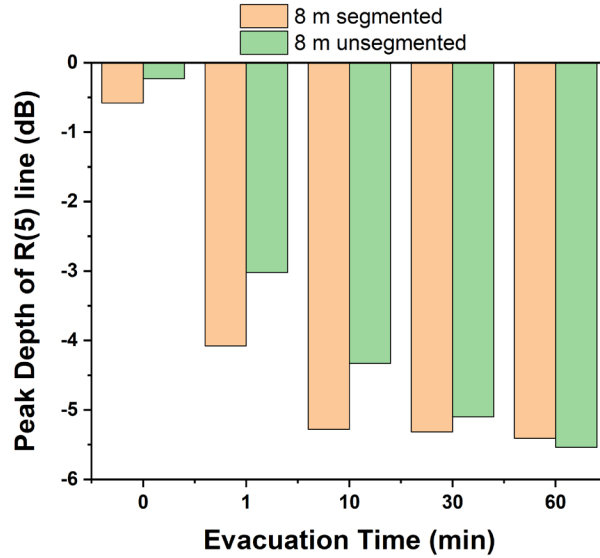
(c)

Figure 3.33: Variation of the R (5) absorption line depth and evacuation time for a 5000-ppm sample of C_2H_2 within (a) 8 m segmented HC-PCF gas cell, and (b) 8 m unsegmented HC-PCF gas cell. (c) the bar graph compares the absorption depths of R (5) line (where an evacuation time of 0 minute represents the scenario where the gas was allowed to flow through the gas cell by running the pump continuously for 30 seconds).

Further, Figure 3.33 indicates that as the evacuation time approaches one hour, the benefit of utilizing the segmented HC-PCF gas cell diminishes. Initially there is a stark difference between the two cells with the absorption line depth of the segmented gas cell achieving 2.52 times that of the unsegmented cell, this diminishes to 1.35 times that of the unsegmented cell at an evacuation time of 1 min, dropping further to 1.21 times the unsegmented cell at a 10 min evacuation. After evacuating for one hour the cells perform nearly the same, with the segmented cell providing 0.98 times the line depth of the unsegmented cell. Figure 3.34 shows a comparison between cell lengths for two evacuation times (1 minute and 1 hour). The 1-minute evacuation data clearly indicates

an improvement when the segmented cell was utilized compared to the same (and even greater) cell length of unsegmented HC-PCF, and with a 4 m segmented cell outperforming the 8 m unsegmented cell. After a 1-hour evacuation however it is clear that the HC-PCF cells have reached saturation as the segmented and unsegmented lengths show comparable absorption line depths (the R (5) line was taken as an example). Both Figure 3.33 and Figure 3.34 highlights the benefit of the segmentation of HC-PCF when a faster response time is required. Additionally, by adding more segments to the cell the overall detection limit could be improved, as it is clear that the absorption line depth of the tested concentrations of C_2H_2 improves with cell length.
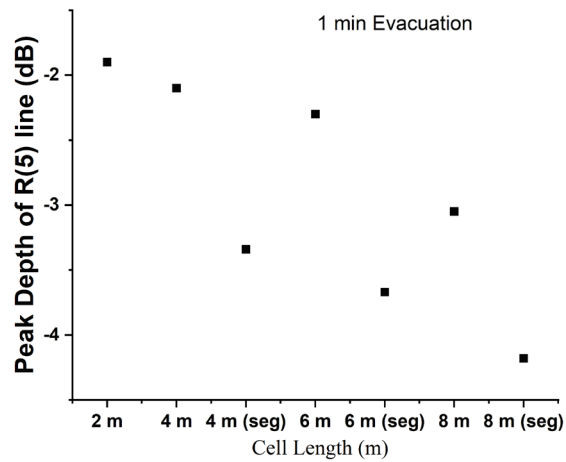
(a)
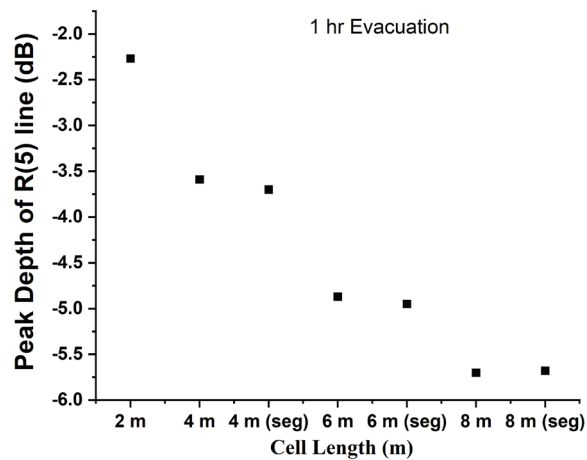
(b)

Figure 3.34: Absorption depth for the R (5) line obtained from 5000 ppm C_2H_2 utilizing a variety of cell lengths (with and without segmentation as indicated by the 'seg' classifier) (a) 1 minute evacuation time; and (b) 1 hour evacuation time.

As discussed previously, in an ICLAS system the physical length of the gas cell is not the 'effective path length' which one would use to calculate the absorption from Beer-

Lambert's law. One may simply use Beer-Lambert's law to back-calculate the effective path by utilizing the background spectra as the initial intensity, and the sample spectra as the output intensity [19]. By calculating the absorption coefficient as detailed in the previous section, and finding the effective path length for each particular absorption peak observed in Figure 3.32 (a), the average effective path was determined to be 13000 cm, or 130 m. A thirteen fold increase upon the segmented ten meter length of HC-PCF used to perform the experiment. If one were to observe an absorption line directly overlapping with the lasing wavelength of the system, in order to determine the effective path length one must consider the ratio of the input and output power of the system, which again can be taken as the measurement made of the background, and measurement made for a particular sample respectively. Arsad et al. developed the mathematical expression for this ratio when one considers a low concentration of gas taken near threshold of the ICAS system [86]. This could significantly improve the limit of detection without having to increase the physical cavity length by operating at threshold. In order to re-fit the system to detect a particular gas using this method the FBG would simply have to be shifted to a particular absorption line, which would stimulate the system to lase at that location.

Finally, once the parameters for the HC-PCF based gas cell are optimized one can remove the quartz windows and translation stages, making an all-fiber system. It will be easy to splice the SMF in the laser cavity to the HC-PCF and keep the segmented section in an enclosure. Currently, the HC-PCF is coiled with a diameter of 12 cm, however the minimum possible radius has not been investigated. It will make the system more compact for practical applications.

Chapter 4

Applications of the Developed System and Future Work

One of the primary applications of the developed system is to function as a sensor for detecting hazardous or detrimental gasses at lower concentration such as greenhouse gasses (GHG). GHG emissions have had a significant impact on the Earth, and they are a major contributor to climate change. Many different industries fuelling our society contribute to climate change including: the energy sector, the transportation sector, the agricultural sector, and waste management. The agricultural sector is of particular interest to this work, and is reported to contribute between 10-12% of anthropogenic GHG emission. This does not even include emissions due to fuel consumption in harvesting, fertilizer production, or the clearance of forest land [87;88]. When one considers all of the secondary factors to the agriculture industry this jumps to 17-32% of all global anthropogenic GHG emissions [88]. Additionally, based on the worlds rapid population growth which is on target to reach nine billion within the next four decades, it is projected that food production must increase by 70% [87]. The agricultural industry also faces potential negative impacts due to climate change, making it a vicious cycle of requiring more farmland and more fertilizer to offset the effect of a changing climate.

The most potent gases contributing to the greenhouse effect other than carbon dioxide (CO_2) are nitrous oxide (N_2O) and methane (CH_4), which are primarily emitted from land based sources [89]. Additionally, waste products from fertilizer such as ammonia gas (NH_3) are of great importance to measure due to the fact that wasted nitrogen cannot be taken up by plants. By tracking the by-products of fertilization one can more efficiently apply it in order to reduce waste and harmful environmental effects. Accurate measurement of agricultural GHG emissions as well as fertilizer by-products will provide a better understanding of the driving mechanisms and parameters affecting GHG flux.

The primary benefit of the segmented HC-PCF gas cell developed in this work is that the temporal resolution of the spectroscopic system can be significantly increased, as has been described in detail in the previous chapter. Another benefit of this system is that the ASE covers a wide range of wavelengths within the telecommunications band, and as such it can detect absorption lines for a number of gas species. Additionally, having a wide range of absorption lines to potentially focus on allows for one to select a particular line which does not have significant overlap with other highly concentrated atmospheric gases, such as water or carbon dioxide (Figure 4.1). Figure 4.1 shows the line strength of the aforementioned GHG as well as water over the same wavelength range as the ASE produced by the EDF laser used in this work. By taking advantage of the broad range one can isolate absorption lines for a gas of interest which are not significantly overshadowed by other atmospheric gases, or other gases which may be produced concurrently. This system, as has been stated, operates within the telecommunications band, where sensors and fiber components are readily available and operate at room temperature, reducing the

cost and power consumption required to operate at other regions of the spectrum, making

a portable detector more viable.
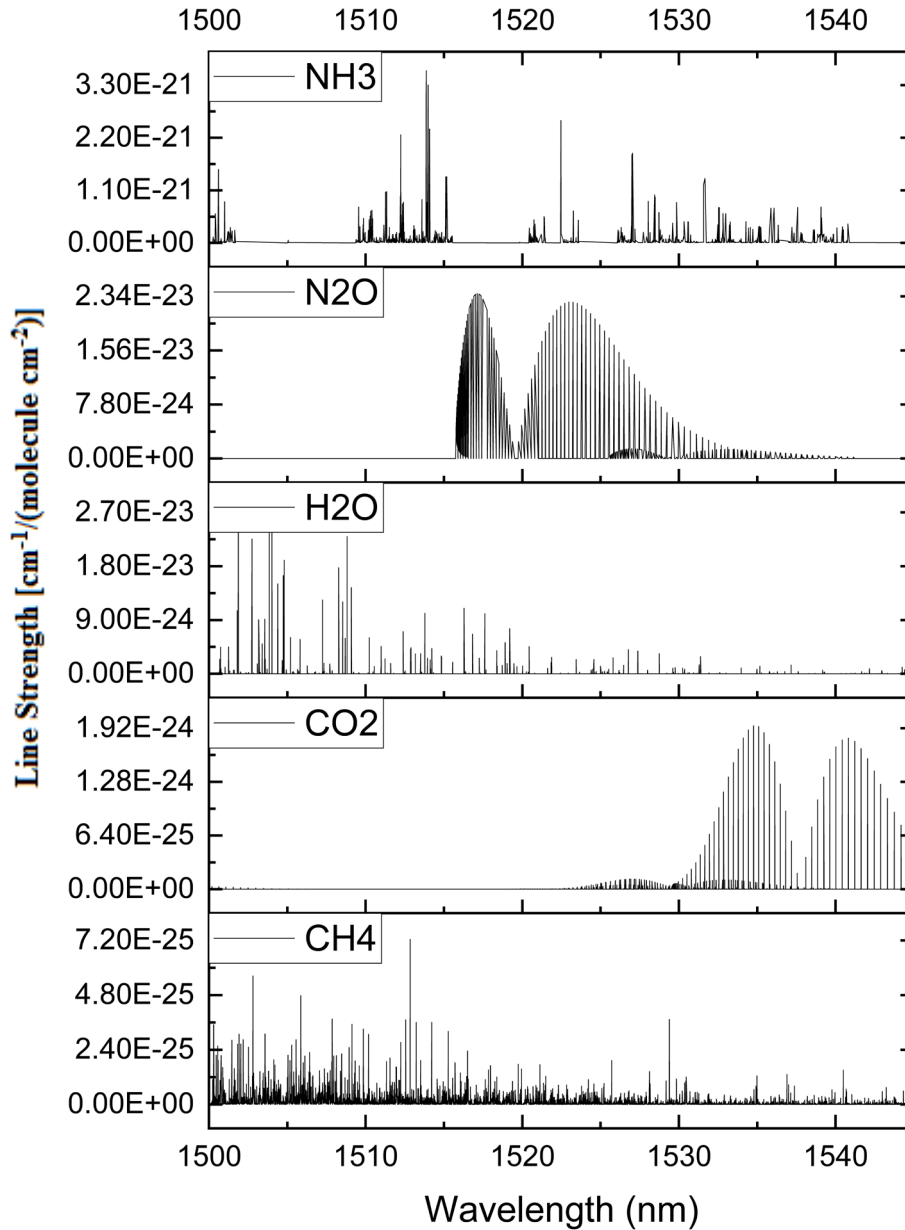
Figure 4.1: Absorption line strength of NH_3, N_2O, CO_2, H_2O, and CH_4 in the range of

the ASE of the fiber laser system used in this work [67]

Acetylene has been covered significantly in the previous chapters, and it is the gas for which the majority of the work has been done in terms of ensuring that the new system works as intended. Other gases of potential interest are ammonia, nitrous oxide, and even carbon dioxide, all of which have absorption lines residing within the ASE of this fiber laser system.

Ammonia gas (NH_3) is produced as a by-product when fields are fertilized, primarily through volatilization. This process of ammonia production accounts for, on average, 12% of atmospheric ammonia [90]. When nitrogen is converted to this form it cannot be taken in by plants, and it is considered a wasteful by-product of fertilization which can not only affect the health of the plants directly, but the entire ecosystem [91]. In addition, ammonia can react with other compounds in the air and form particulates resulting in haze, which can also affect our health negatively [91-94]. As with most chemical reactions occurring in the soil, the rate of ammonia volatilization is affected by everything from the humidity, temperature, pH, bacterial content, and overall aeration of the soil, as well as the type of crop planted within the soil [95;96]. It is for this reason that it is difficult to accurately predict what percentage of the total nitrogen mass deposited onto the field via fertilizer will be converted to ammonia for any particular season. This same argument can be made for most by-products of nitrogen-based fertilizer, including nitrous oxide, highlighting the usefulness of a cost effective, low footprint detector which is capable of operating at room temperature capable of detecting such emissions. When it is difficult to predict percentage of nitrogen that will be lost to wasteful by-products, direct measurement is a good substitute when it is viable to do so.

In terms of ammonia, one of the most common pathways for its production is through the reaction of urea in the soil when applied as fertilizer. Urea is the most common nitrogen fertilizer [97], however as has been mentioned there are many by-products produced during its reaction within the soil which cannot be utilized by the plants which the fertilizer is intended to help [98].

Several other molecules are produced as a result of adding urea to the soil, some of which are harmful while others are benign. One way in which fertilizer has been adapted is to coat it with a polymer in order to slowly release the urea into the soil, such as the Environmentally Smart Nitrogen developed by Nutrien (https://smartnitrogen.com). By this slow release method, the overall change in pH caused by the above mechanism can be buffered over a longer period of time, reducing the overall amount of volatized ammonia [99]. This is one potential application for a cost effective and portable gas sensor which can easily be deployed in the field: testing alternative fertilizers to bare urea in the extremely varied soil and weather conditions around the world in order to see how the emission of waste nitrogen is affected.

Another GHG produced by the agricultural industry through fertilization is N_2O, which has a three hundred times greater pound for pound capacity for absorbing infrared radiation than CO_2 [100]. In addition, it is one of the most destructive compounds affecting the Earth's ozone layer [101]. It is estimated that the agricultural industry is responsible for approximately 27% of N_2O emissions, with the remainder being produced naturally from the soil and the oceans [102]. As with NH_3, N_2O can also be produced through the breakdown of nitrogen based fertilizers when they are applied in the field,

with a significant spike in production if applied at the wrong time or in the wrong amount [103]. N_2O can be produced both through nitrification and denitrification, however denitrification dominates the many complex pathways leading to its production [104;105]. The factors affecting the rate of N_2O production through each pathway greatly depend on the same environmental factors as described for the production of NH_3, namely soil pH, temperature, humidity, and grain size, as well as the microbiom present within the soil [103;105;106]. The denitrification pathway is favoured when the soil is especially water logged, which favours anaerobic processes due to the lack of oxygen. The process is caused by bacteria utilizing nitrates and nitrites as an electron acceptor when oxygen is not readily available [105]. This water logged state can occur of course during heavy rainfall, but also if the soil is over-irrigated [107]. It is difficult to predict the reason for changes in N_2O production as the soil and environment change[108], and as such direct measurement is key in predicting the N_2O output globally.

One important factor to consider when it comes to the application of this particular spectroscopic system, particularly when applied in the agricultural industry, is the collection method itself. There are many agricultural GHG emission techniques in the literature including chamber based methods, and micrometeorological methods [109]. Chamber based methods are implemented by enclosing an area with a sealed chamber, often called static chambers, from which gas samples are collected at set time intervals. Chamber based methods are advantageous, since they are relatively cheap to construct, easy to deploy in remote areas, and low frequency sensors can be used for measurements. Some disadvantages include the inability to cover a broad area as a new chamber would need to be introduced to each area of interest, additionally care must be taken not to

disturb or modify the biological component of the soil when covered by the chamber as this can significantly impact the rate at which gas is produced. There are many micrometeorological methods which include eddy covariance, the aerodynamic gradient method, mass balance and plume methods, and the boundary layer budget approach [109]. Micrometeorological methods have an advantage of covering a significantly larger area than the chamber technique described above; however this is countered by their significantly higher cost and the effect of terrain features playing a significant role in measurements, in addition it requires a sophisticated high frequency data collection system. The data collection rate for micrometeorological systems is not met by the system which has been described and developed in this work, however a chamber based collection method would absolutely be viable due to the slower data collection rate, which is required in order to keep the soil healthy, as over collecting data (having the chamber sealed too many times per day or for too long each time) keeps the soil within out of the sun and the rain. This fact identifies another benefit of the segmented HC-PCF gas cell, as it can take in gas at a significantly higher rate than its unsegmented counterpart a real time monitoring system based on the chamber method would be possible without unnecessary damage to the microbiom of the soil caused by prolonged chamber closure.

The GHG measurement techniques using static chambers are extremely diverse, and there are many variations in chamber design, deployment, sampling volume and analysis technique, as well as the flux calculations used [89]. When deploying chambers in the field one must consider the pattern of the crop being planted, the method of fertilizer application (which can change the coverage within the field), as well as the

plant height. When sampling, a balance must be struck between the time required to see a change in flux of a particular gas species, while minimizing the disturbance of the microclimate the chamber contains while its closed to collect data [110]. Much work has been done to standardize measurements and data reporting in this field, particularly from the Department of Agriculture Agricultural Research Services Greenhouse gas Reduction through Agricultural Carbon Enhancement network (GRACEnet) [111] and by the Global Research Alliance on Agricultural Greenhouse Gases (GRA) [112]. Of particular note is the GRA which provides an extensive list of recommendations in terms of chamber design, deployment, and sample collection. The GRA review in particular provides an exhaustive list of recommendations on the chamber design, deployment protocols, air sample collection, as well as data analysis procedures and report formatting.

A static chamber consists of an anchor which is embedded within the soil, with a lid placed on top during sample collection. Care must be taken when inserting the anchor so as not to disturb the soil extraneously, and the anchor height above the soil should be kept to a minimum (5 cm) to avoid large reservoirs of water forming during rainstorms, which would affect the microclimate of the soil within [111;112]. The lid should make a gas tight seal with the anchor using a gasket, while also facilitating the collection of gas samples. The chamber should be constructed from a material such as stainless steel or PVC to avoid reaction with the sample of interest and with the microbiome the chamber contains. Static chamber design requirements suggested by the GRA in order to maximise flux sensitivity and minimize and measurement artefacts include everything from the material of the chamber to its dimensions and insulation and venting [112].

There are many sample collection techniques, ranging from manual collection methods to automatic. The most common manual technique encountered in the literature involves a syringe fitted with a needle and stopcock which is used to extract a sample from the chamber via a septum . Once the sample is drawn into the syringe, the syringe is removed from the septum, and the stopcock is closed. The samples are transferred into vials for storage, slightly over-pressurizing the vial to ensure sample integrity [89].

Automated sample collection is possible, and desirable, when many systems are deployed over a large area, and the sampling approach depends on the specific design of the automated chamber. Umwelt- und Ingenieurtechnik GmbH Dresden (UIT) in Germany have a commercially available automated system which collects gas samples in vials. The chamber is positioned on the anchor electronically, guided by a rail, to facilitate the opening and closing of the chamber. When the sample vials available in the device are all filled, the sample vials must be manually removed from the device, and replaced with new vials. The sample vials are typically then taken off site to the laboratory to determine the gas concentration in each sample. Another automated chamber technique has been developed where samples are collected in copper loops [113]. The lid of the chamber is connected through a linkage system and an actuator is utilized to close the chamber during sample collection. Once the sample is collected, the copper loop is automatically rotated, isolating the sample within a particular loop and preparing a new loop for sample collection. The system contains twenty four copper loops, which allows for a number of samples to be taken before they, as with the previous system, must be collected and brought to a lab for analysis. It is at this stage in the sample collection process where a cost-effective mobile sample analysis setup could be

particularly useful, where data could be collected and transmitted remotely to a database for further processing and analysis. These measurements could also be accompanied by direct ancillary measurements including soil and air temperature, atmospheric pressure, total rainfall, and soil water content [114].

By taking advantage of the faster fill and evacuation rate of segmented HC-PCF it is possible to perform real time monitoring for gasses of interest, with the agricultural industry particularly highlighted due to the ever-present and increasingly important need to monitor and minimize GHG output. By taking advantage of a low- cost room temperature detection system with a small footprint and sample volume requirement it may be possible to perform data collection in areas which would otherwise be prohibitive either due to distance or lack of manpower to supervise and collect samples manually. GHG monitoring is not the only area where such a system could find use, everything from industrial applications to mining and other raw resource extraction processes could take advantage of such a system. Making PCF more applicable in terms of real time monitoring by minimizing its major downside, that being extremely long fill and evacuation periods, in addition to providing the option of direct coupling of the input and output of the cell to the fiber laser system, will allow it to be considered for applications in sensing beyond the laboratory and allow it to be fully explored and taken advantage of in the constantly developing world of gas detection.

References

[1] W. Herschel, "IV. On the Power of Penetrating into Space by Telescopes; with a Comparative Determination of the Extent of that Power in Natural Vision, and in Telescopes of Various Sizes and Constructions; Illustrated by Select Observations," *Philosophical Transactions of the Royal Society of London*, vol. 90, pp. 49-85, 1880.

[2] W. Herschel, "On the Absorption of Light by Coloured Media, and on the Colours of the Prismatic Spectrum exhibited by certain Flames ; with an Account of a ready Mode of determining the absolute dispersive Power of any Medium, by direct experiment.," *Earth and Environmental Science Transactions of The Royal Society of edinburgh*, vol. 9, no. 2, pp. 445-460, 1823.

[3] N. C. Thomas, "The Early History of Spectroscopy," *Journal of Chemical Education*, vol. 68, no. 8, pp. 631-634, 1991.

[4] W. Abney, "XVII. The Bakerian Lecture.—On the Photographic Method of Mapping the least R frangible End of the Solar Spectrum.," *Philosophical Transactions of the Royal Society of London*, vol. 171, pp. 653-667, 1880.

[5] F. S. Brackett, "An Examination of the Infra-Red Spectrum of the Sun, ë8900-ë9900," *Astrophysical Journal*, vol. 53, pp. 121-132, 1921.

[6] C. Abney and Lieut.-Colonel Festing, "On the Influence of the Atomic Grouping in the Molecules of Organic Bodies on Their Absorption in the Infra-Red Region of the Spectrum.," *Philosophical Transactions of the Royal Society of London*, vol. 172, pp. 887-918, 1881.

[7] R. G. Kuehni and A. Schwarz, *Color Ordered: A Survey of Color Order Systems from Antiquity to the Present*, 1 ed Oxford University Press, 2008.

[8] N. Bohr, "I. On the Constitution of Atoms and Molecules," *Philosophical Magazine and Journal of Science*, vol. 26, no. 151, pp. 1-25, 1913.

[9] B. L. Haendler, "Presenting the Bohr Atom," *Journal of Chemical Education*, vol. 59, no. 5, pp. 372-376, 1982.

[10] R. B. Barnes, R. S. McDonald, and V. Z. Williams, "Small-Prism Infra-Red Spectrometry," *Journal of Applied Physics*, vol. 16, pp. 77-86, 1945.

[11] A. Walsh, "The Application of Atomic Absorption Spectra to Chemical Analysis,", 7 ed 1955, pp. 108-117.

[12] A. Kumar, T. M. G. Kingson, R. P. Verma, A. Kumar, R. Mandal, S. Dutta, S. K. Chaulya, and G. M. Prasad, "Application of Gas Monitoring Sensors in Underground Coal Mines and Hazardous Areas," *International Journal of Computer Technology and Electronics Engineering*, vol. 3, no. 3, pp. 9-23, 2013.

[13] A. Abbaszadeh, S. Makouei, and S. Meshgini, "Ammonia Measurement in Exhaled Human Breath using PCF sensor for Medical Applications," *Photonics and Nanostructures - Fundamentals and Applications*, vol. 44, pp. 1-8, 2021.

[14] U. Platt, "Modern Methods of the Measurement of Atmospheric Trace Gases," *Physical Chemistry Chemical Physics*, vol. 1, pp. 5409-5415, 1999.

[15] T. D. Rapson and H. Dacres, "Analytical Techniques for Measuring Nitrous Oxide," *Trends in Analytical Chemistry*, vol. 54, pp. 64-75, 2014.

[16] J. Hodgkinson and R. P. Tatam, "Optical gas sensing: a review," *Measurement Science and Technology*, vol. 24, no. 1 Jan.2013.

[17] G. Stewart, K. Atherton, H. B. Yu, and B. Culshaw, "An investigation of an optical fibre amplifier loop for intra-cavity and ring-down cavity loss measurements," *Measurement Science & Technology*, vol. 12, no. 7, pp. 843-849, July2001.

[18] K. Stelmaszczyk, M. Fechner, and P. Rohwetter, "Towards Supercontinuum Cavity Ring-Down Spectroscopy," *Applied Physics B*, vol. 94, pp. 369-373, 2009.

[19] V. M. Baev, Latz T., and Toschek P.E., "Laser Intracavity absorption spectroscopy," *Applied Physics B*, vol. 69, pp. 171-202, 1999.

[20] B. Lohden, S. Kuznetsova, K. Sengstock, V. M. Baev, A. Goldman, S. Cheskis, and B. Palsdottir, "Fiber laser intracavity absorption spectroscopy for in situ multicomponent gas analysis in the atmosphere and combustion environments," *Applied Physics B-Lasers and Optics*, vol. 102, no. 2, pp. 331-344, Feb.2011.

[21] W. G. French, J. B. MacChensney, P. B. O'Connor, and G. W. Tasker, "Optical Waveguides with Very Low Losses," *The Bell system technical journal*, vol. 53, no. 5, pp. 951-954, 1974.

[22] G. Keiser, *Optical Fiber Communications*, 3 ed. Boston, MA: McGraw Hill, 2000.

[23] A. W. Snyder and J. D. Love, *Optical Waveguide Theory* Chapman and Hall Ltd, 1983.

[24] P. Russell, "Photonic Crystal Fibers," *Science*, vol. 299, no. 358, p. 362, 2003.

[25] W. Schmidt, F. Schuth, and C. Weidenthaler, "Diffraction and Spectroscopy of Porous Solids," in *Comprehensive Inorganic Chemistry II,* 2 ed Elsevier, 2013, pp. 1-24.

[26] J. Shao, G. Liu, and L. Zhou, "Structural colors of photonic crystals on textiles," in *Active Coatings for Smart Textiles,* 1 ed. J. Hu, Ed. Elsevier, 2016, pp. 284-286.

[27] X. Tao, *Wearable Electronics and Photonics*, 1 ed Woodhead Publishing, 2005.

[28] G. Freymann, V. Kitaev, B. Lotsch, and G. Ozin, "Bottom-Up Assemply of Photonic Crystals," *Chemical Society Reviews*, vol. 42, pp. 2528-2554, 2013.

[29] A. F. Koenderink and W. I. Vos, "Optical Properties of Real Photonic Crystals: Anomalous Diffuse Transmission," *Optical Society of America B*, vol. 22, no. 5, pp. 1075-1084, 2005.

[30] H. Kano and H. O. Hamaguchi, "In-vivo Multi-Nonlinear Optical Imaging of a Living Cel Using a Supercontinuum Lught Source Generated from a Photonic Crystal Fiber," *Optics Express*, vol. 14, no. 7, pp. 2798-2804, 2006.

[31] J. E. Sharping, M. Fiorentino, P. Kumar, and R. S. Windeler, "Optical Parametric Oscillator Based on Four-Wave mixing in Microstructure Fiber," *Optics Lett.*, vol. 27, no. 19, pp. 1675-1677, 2002.

[32] J. Hansryd, P. A. Andrekson, M. Westlund, J. Li, and P. Hedekvist, "Fiber-Based Optical Parametric Amplifiers and Their Applications," *Ieee Journal of Selected Topics in Quantum Electronics*, vol. 8, no. 3, pp. 506-520, 2002.

[33] R. Holzwarth, T. Udem, and T. W. Hansch, "Optical Frequency Synthesizer for Precision Spectroscopy," *Physical Review Lett.*, vol. 85, no. 11, pp. 2264-2267, 2000.

[34] T. Udem, R. Holzwarth, and T. W. Hansch, "Optical Frequency Metrology," *Nature*, vol. 416, pp. 233-237, 2002.

[35] B. Povazay, K. Bizheva, A. Unterhuber, B. Hermann, H. Sattmann, A. F. Fercher, W. Drexler, and A. Apolonski, "Submicrometer Axial Reslution Optical Coherence Tomography," *Optics Lett.*, vol. 27, no. 20, pp. 1800-1802, 2002.

[36] D. L. Marks, A. L. Oldenburg, J. J. Reynolds, and S. A. Boppart, "Study of an ultrahigh-numerical-aperture fiber continuum generation source for

optical coherence tomography," *Optics Letters*, vol. 27, no. 22, pp. 2010-2012, Nov.2002.

[37] A. M. R. Pinto and M. Lopez-Amo, "All-Fiber Lasers Through Photonic Crystal Fibers," *Nanophotonics*, vol. 2, no. 5-6, pp. 355-368, 2013.

[38] Z. Zhu and T. Brown, "Analysis of the Space Filling Modes of Photonic Crystal Fibers," *Optics Express*, vol. 8, no. 10, pp. 547-554, 2001.

[39] T. A. Birks, J. Roberts, D. Atkin, P. J. Russell, and T. J. Shepherd, "Full 2-D Photonic Bandgaps in Silica/Air Structures," *Electronics Letters*, vol. 31, no. 22, pp. 1941-1943, 1995.

[40] R. F. Cregan, J. C. Mangan, T. A. Birks, P. St. J. Russell, P. J. Roberts, and D. C. Allan, "Single-Mode Photonic Band Gap Guidance of Light in Air," *Scientific Reports*, vol. 285, pp. 1537-1539, 1999.

[41] G. Bouwmans, F. Luan, J. C. Knight, P. S. Russell, L. Farr, B. J. Mangan, and H. Sabert, "Properties of a Hollow-Core Photonic Bandgap Fiber at 850 nm Wavelength," *Optics Express*, vol. 11, no. 14, pp. 1613-1620, 2003.

[42] F. Benabid, "Hollow-Core Photonic Bandgap Fibre: New Light GUidance for New Science and Technology," *Philosophical Transactions of the Royal Society Series A*, vol. 364, pp. 3439-3462, 2006.

[43] J. C. Knight, J. Broeng, T. A. Birks, and P. S. J. Russel, "Photonic band gap guidance in optical fibers," *Science*, vol. 282, no. 5393, pp. 1476-1478, Nov.1998.

[44] P. J. Roberts, F. Couny, H. Sabert, B. J. Mangan, D. P. Williams, L. Farr, M. W. Mason, and A. Tomlinson, "Ultimate Low Loss of Hollow-Core Photonic Crystal Fibers," *Optics Express*, vol. 13, no. 1, pp. 236-244, 2005.

[45] J. K. Valiunas, G. Stewart, and G. Das, "Detection of Nitrous Oxide (N2O) at Sub-ppmv Using Intracavity Absorption Spectroscopy," *Ieee Photonics Technology Letters*, vol. 28, no. 3, pp. 359-362, Feb.2016.

[46] J. K. Valiunas, M. Tenuta, and G. Das, "A Gas Cell Based on Hollow-Core Photonic CrystalFiber (PCF) and Its Application for the Detection ofGreenhouse Gas (GHG): Nitrous Oxide (N2O)," *Journal of Sensors*, pp. 1-9, 2016.

[47] A. Isomaki and O. G. Okhotnikov, "Femtosecond Soliton Mode-Locked Laser Based on Ytterbium-Doped Photonic Bandgap Fiber," *Optics Express*, vol. 14, no. 20, pp. 9238-9243, 2006.

[48] A. Shirakawa, H. Maruyama, K. Ueda, C. B. Olausson, J. K. Lyngso, and J. Broeng, "High-Power Yb-Doped Photonic Bandgap Fiber Amplifier at 1150-1200 nm," *Optics Express*, vol. 17, no. 2, pp. 447-454, 2008.

[49] S. Gowre, S. Mahapatra, and P. K. Sahu, "A Modified Structure for All-Glass Photonic Bandgap Fibers: Dispersion Characteristics and Confinement Loss Analysis," *International Scholarly Research Notices*, vol. 2013, pp. 1-5, 2013.

[50] W. J. Miniscalco, "Erbium-Doped Glasses for Fiber Amplifiers at 1500-Nm," *Journal of Lightwave Technology*, vol. 9, no. 2, pp. 234-250, Feb.1991.

[51] W. L. Barnes, R. I. Laming, E. J. Tarbox, and P. R. Morkel, "Absorption and Emission Cross-Section of Er3+ Doped Silica Fibers," *Ieee Journal of Quantum Electronics*, vol. 27, no. 4, pp. 1004-1010, Apr.1991.

[52] P. C. Becker, N. A. Olsson, and J. R. Simpson, *Erbium-Doped Fiber Amplifiers: Fundamentals and Technology*, 1 ed. San Diego: Academic Press, 2010.

[53] N. Arsad, M. Li, G. Stewart, and W. Johnstone, "Intra-Cavity Spectroscopy Using Amplified Spontaneous Emission in Fiber Lasers," *Journal of Lightwave Technology*, vol. 29, no. 5, pp. 782-788, Mar.2011.

[54] P. Tsai, F. Sun, G. Xiao, Z. Zhang, S. Rahimi, and D. Ban, "A New Fiber-Bragg-Grating Sensor Interrogation System Deploying Free-Spectral-Range-Matching Scheme With High Precision and Fast Detection Rate," *IEEE Photincs Technology Letters*, vol. 20, no. 4, pp. 300-302, 2008.

[55] P. Kronenberg, P. Rastogi, P. Giaccari, and H. Limberger, "Relative Humidity Sensor with Optical Fiber Bragg Gratings," *Optics Lett.*, vol. 27, no. 16, pp. 1385-1387, 2002.

[56] F. J. Arregui, I. R. Matias, K. L. Cooper, and R. O. Claus, "Simultaneous measurement of humidity and temperature by combining a reflective intensity-based optical fiber sensor and a fiber Bragg grating," *IEEE Sensors Journal*, vol. 2, no. 5, pp. 482-487, 2002.

[57] G. Hwang, C. Ma, D. Huang, and L. Liao, "Study on Reflection Spectrum Areas of an FBG for Strain Gradient Measurment,", 10.1109/ICSENS.2012.6411410 ed 2012, pp. 1-4.

[58] K. O. Hill, Y. Fujii, D. C. Johnson, and B. S. Kawasaki, "Photosensitivity in Optical Fiber Waveguides - Application to Reflection Filter Fabrication," *Applied Physics Letters*, vol. 32, no. 10, pp. 647-649, 1978.

[59] G. Meltz, W. W. Morey, and W. H. Glenn, "Formation of Bragg Gratings in Optical Fibers by A Transverse Holographic Method," *Optics Letters*, vol. 14, no. 15, pp. 823-825, Aug.1989.

[60] M. Bakaic, M. Hanna, C. Hnatovsky, D. Grobnic, S. Mihailov, S. S. Zeisler, and C. Hoehr, "Fiber-Optic Bragg Gratings for Temperature and Pressure Measurements in Isotope Production Targets for Nuclear Medicine," *Applied Sciences*, vol. 10, pp. 1-14, 2020.

[61] G. Palumbo, D. Tosi, A. Iadicicco, and S. Campopiano, "Analysis and design of Chirped Fiber Bragg Grating for Temperature Sensing for Possible Biomedical Applications,", 10 ed 2018.

[62] X. Dong, H. Zhang, B. Liu, and Y. Miao, "Tilted Fiber Bragg Gratings: Principle and Sensing Applications,", 1 ed 2011, pp. 6-30.

[63] C. H. Wang, L. R. Chen, and P. W. E. Smith, "Analysis of Chirped-Sampled and Sampled-Chirped Fiber Bragg Gratings,", 41 ed 2002, pp. 1654-1660.

[64] Z. Medendorp, J. Valiunas, and G. Das, "Wavelength-Switchable fiber laser," *Microwave and Opt. Technol. Lett.*, vol. 49, no. 6, pp. 1231-1233, 2007.

[65] G. Zhong, Z. Ma, J. Wang, C. Zheng, Y. Zhang, Y. Wang, and F. Tittel, "Near-Infrared Tunable Laser Absorption Spectroscopic Acetylene Sensor System Using a Novel Three Mirror-Based, Dense Pattern Gas Cell," *Sensors*, vol. 20, no. 5, p. 1266, 2020.

[66] V. M. Baev, I. N. Sarkisov, E. A. Sviridenkov, and A. F. Suchkov, "Intracavity Laser Spectroscopy," *Journal of Soviet Laser Research*, vol. 10, no. 1, pp. 61-85, 1989.

[67] L. S. Rothman, I. E. Gordon, Y. Babikov, A. Barbe, D. C. Benner, P. F. Bernath, M. Birk, L. Bizzocchi, V. Boudon, L. R. Brown, A. Campargue, K. Chance, E. A. Cohen, L. H. Coudert, V. M. Devi, B. J. Drouin, A. Fayt, J. M. Flaud, R. R. Gamache, J. J. Harrison, J. M. Hartmann, C. Hill, J. T. Hodges, D. Jacquemart, A. Jolly, J. Lamouroux, R. J. Le Roy, G. Li, D. A. Long, O. M. Lyulin, C. J. Mackie, S. T. Massie, S. Mikhailenko, H. S. P. Muller, O. V. Naumenko, A. V. Nikitin, J. Orphal, V. Perevalov, A. Perrin, E. R. Polovtseva, C. Richard, M. A. H. Smith, E. Starikova, K. Sung, S. Tashkun, J. Tennyson, G. C. Toon, V. G. Tyuterev, and G. Wagner, "The HITRAN 2012 molecular spectroscopic database," *Journal of Quantitative Spectroscopy & Radiative Transfer*, vol. 130, pp. 4-50, Nov.2013.

[68] J. Tennyson, P. F. Bernath, A. Campargue, A. G. Csaszar, L. Daumont, R. R. Gamache, J. T. Hodges, D. Lisak, O. V. Naumenko, L. S. Rothman, H. Tran, N. F. Zobov, and J. Buldyreva, "Recommended Isolated-Line Profile

for Representing High-Resolution Spectroscopic Transitions (IUPAC Technical Report)," *Pure and Applied Chemistry*, vol. 86, no. 12, pp. 1931-1943, 2014.

[69] V. M. Devi, R. R. Gamache, B. Vispoel, C. L. Renaud, D. C. Benner, M. A. H. Smith, T. A. Blake, and R. L. Sams, "Line Shape Parameters of Air-Broadened Water Vapor Transitions in the v1 and v3 Spectral Region," *Journal of Molecular Spectroscopy*, vol. 348, pp. 13-36, 2018.

[70] D. C. Benner, C. P. Rinsland, M. Devi, A. H. Smith, and D. Atkins, "A Multispectrum Nonlinear Least Squares Fitting Technique," *Journal of Quantitative Spectroscopy & Radiative Transfer*, vol. 53, no. 6, pp. 705-721, 1995.

[71] M. Simeckova, D. Jacquemart, L. S. Rothman, R. R. Gamache, and A. Goldman, "Einstein a-Coefficients and Statistical Weights for Molecular Absorption Transitions in the HITRAN Database," *Journal of Quantitative Spectroscopy & Radiative Transfer*, vol. 98, pp. 130-155, 2006.

[72] R. R. Gamache, B. Vispoel, M. Rey, A. Nikitin, V. Tyuterev, O. Egorov, I. Gordon, and V. Boudon, "Total Internal Partition SUms for the HITRAN2020 Database," *Journal of Quantitative Spectroscopy & Radiative Transfer*, vol. 271, pp. 1-16, 2021.

[73] K. Nakagawa, M. Labachelerie, Y. Awaji, and M. Kourogi, "Accurate Optical Frequency Atlas of the 1.5-um bands of acetylene," *Optical Society of America B*, vol. 13, no. 12, pp. 2708-2714, 1996.

[74] A. Popovas and U. G. Jorgensen, "I. Improved Partition Functions and Thermodynamic Quantities for Normal, Equilibrium, and Ortho and Para Molecular Hydrogen," *Astronomy and Astrophysics*, vol. 595, pp. 1-23, 2016.

[75] "https://hitran.org/," 2021.

[76] "https://hitran.iao.ru/home," 2021.

[77] K. P. Huber and G. Herzberg, *Molecular Spectra and Molecular Structure*, 1 ed Springer, 1979.

[78] C. di Lauro, *Rotational Structure in Molecular Infrared Spectra*, 1 ed Elsevier, 2013.

[79] T. Shimanouchi, *Tables of Molecular Vibrational Frequencies Consolidated Volume 1*, 6 ed 1972.

[80] P. Worsfold, A. Townshend, C. Poole, and M. Miro, *Encyclopedia of Analytical Science*, 3 ed Elsevier, 2019.

[81] J. M. Hollas, *Modern Spectroscopy*, 4th ed. Hoboken, NJ: J. Wiley, 2004.

[82] F. Benabid, F. Couny, J. C. Knight, T. A. Birks, and P. S. Russell, "Compact, stable and efficient all-fibre gas cells using hollow-core photonic crystal fibres," *Nature*, vol. 434, no. 7032, pp. 488-491, Mar.2005.

[83] Z. J. Chaboyer, P. J. Moore, and G. Das, "Medium power single-mode single-wavelength fiber laser," *Optics Commun.*, vol. 282, pp. 3100-3103, 2009.

[84] H. C. Lefevre, "Single-Mode Fiber Fractional Wave Devices and Polarization Controllers," *Electronics Letters*, vol. 16, no. 20, pp. 778-780, 1980.

[85] L. G. Wade, *Organic Chemistry*, 6 ed Pearson Prentice Hall, 2006.

[86] Arsad N. and Stewart G., "Stable, tunable, and single-mode operation of an erbium-doped fibre laser system using a saturable absorber for gas spectroscopy applications,", SPIE 7195 ed 2009, pp. 719525-1-719525-10.

[87] C. Pye-Smith, *Farming's Climate-Smart Future Placing Agriculture at the Heart of Climate-Change Policy* Technical Centre for Agricultural and Rural Cooperation ACP-EU, 2011.

[88] J. Bellarby, B. Foereid, A. Hastings, and P. Smith, *Cool Farming: Climate Impacts of Agriculture and Mitigation Potential* Greenpeace International, 2008.

[89] S. M. Collier, M. D. Ruark, L. G. Oates, W. E. Jokela, and C. J. Dell, "Measurement of Greenhouse Gas Flux from Agricultural Soils Using Static Chambers," *Jove-Journal of Visualized Experiments*, no. 90 Aug.2014.

[90] A. F. Bouwman, L. J. Bourmans, and N. H. Batjes, "Estimation of Global NH3 Volatization Loss from Synthetic Fertilizers and Animal Manure Applied to Arable Lands and Grasslands," *Global Biogeochemical Cycles*, vol. 16, no. 2, pp. 1024-1034, 2002.

[91] W. A. H. Asman, M. A. Sutton, and J. K. Schjorring, "Ammonia: Emission, Atmospheric Transport and Deposition," *New Phytol.*, vol. 139, pp. 27-48, 1998.

[92] M. Ferm, "Atmospheric Ammonia and Ammonium Transport in Europe and Critical Loads: A Review," *Nutrient Cycling in Agroecosystems*, vol. 51, pp. 5-17, 1998.

[93] B. J. Finlayson-Pitts and J. N. Pitts, *Chemistry of the Upper and Lower Atmosphere* Academic Press, 1999.

[94] C. A. Pope and D. W. Dockery, "Health Effects of Fine Particulate Air Pollution: Lines That Connect," *Journal of Air and Waste Management Association*, vol. 56, pp. 709-742, 2008.

[95] W. L. Hargrove, "Evaluation of Ammonia Volatization in the Field," *Journal of Production Agriculture*, vol. 1, pp. 104-111, 1988.

[96] C. Proctor, R. Koenig, and W. Johnston, "Potential for Ammonia Volatization from Urea in Dryland Kentucky Bluegrass Seed Production Systems," *Communications in Soil Science and Plant Analysis*, vol. 41, no. 3, pp. 320-331, 2010.

[97] H. Dittmar, M. Drach, and R. Vosskamp, "Fertilizers, 2. Types," in *Ullmann's Encyclopedia of Industrial Chemistry* Weinheim: Wiley-VCH, 2016, pp. 199-245.

[98] D. E. Kissel, M. L. Cabrera, and R. B. Ferguson, "Reactions of Ammonia and Urea Hydrolysis PRoducts with Soil," *Soil Sciences Society of America*, vol. 52, pp. 1793-1796, 1988.

[99] A. Shaviv, S. Raban, and E. Zaidel, "Modeling Controlled Nutrient Release from a Population of Polymer Coated Fertilizers: Statistically Based Model for Diffusion Release," *Environmental Science and Technology*, vol. 37, no. 10, pp. 2257-2261, 2003.

[100] K. Denman, G. Brasseur, A. Chidthaisong, P. Ciais, P. Cox, and M. Dickinson, "Couplings Between Changes in the Climate System and Biogeochemistry," in *Climate Change 2007: The Physical Science Basis*. S. Solomon, D. Qin, M. Manning, and Z. Chen, Eds. New York: Cambridge University Press, 2007, pp. 499-587.

[101] A. R. Ravishankara, R. W. Portmann, and J. S. Daniel, "Nitrous Oxide (N2O): The Dominant Ozone-Depleting Substance Emitted in the 21st Century," *Science*, vol. 326, pp. 123-125, 2009.

[102] A. Syakila and C. Kroeze, "The Global Nitrous Oxide Budget Re-Visited," *Greenhouse Gas Measurement Management*, vol. 1, pp. 17-26, 2011.

[103] C. Wang, B. Amon, K. Schulz, and B. Mehdi, "Factors that Influence Nitrous Oxide Emissions from Agricultural Soils as WEll as their Representation in Simulation Models: A Review," *Agronomy*, vol. 11, pp. 1-30, 2021.

[104] D. Fowler, C. E. Steadman, D. Stevenson, M. Coyle, R. M. Rees, U. M. Skiba, M. A. Sutton, and J. N. Cape, "Effects of Global Change During the 21st Century on the Nitrogen Cycle," *Atmospheric Chemistry and Physics*, vol. 15, pp. 13849-13893, 2015.

[105] K. Butterbach-Bahl, E. Baggs, M. Dannenmann, R. Kiese, and S. Zechmeister-Boltenstern, "Nitrous Oxide Emissions from Soils: How well do we Understand the Processes and Their Controls?," *Philosophical Transactions of the Royal Society of London*, vol. 368, pp. 1-13, 2013.

[106] A. R. Mosier, "Nitrous Oxide Emissions from Agricultural Soils," *Fertilizer Research*, vol. 37, pp. 191-200, 1994.

[107] P. M. Groffman, M. A. Alabet, J. K. Bohlke, K. Butterbach-Bahl, M. B. David, and M. K. Firestone, "Methods for MEasuring Denitrification: Diverse Approaches to a Difficult Problem," *Ecological Applications*, vol. 16, pp. 2091-2122, 2006.

[108] F. Schreiber, P. Wunderlin, K. Udert, and G. Wells, "Nitric Oxide and Nitrous Oxide Turnover in Natural and Engineerd Microbial Communities: Biological Pathways, Chemical Reactuions, and Novel Technologies," *Frontiers in Microbiology*, vol. 3, pp. 1-24, 2012.

[109] A. Hensen, U. Skiba, and D. Famulari, "Low Cost and State of the art Methods to Measure Nitrous Oxide Emissions," *Environmental Resources Letters*, vol. 8, pp. 1-10, 2013.

[110] G. Borjesson, A. Danielsson, and B. H. Svensson, "Methane fluxes from a Swedish landfill determined by geostatistical treatment of static chamber measurements," *Environmental Science & Technology*, vol. 34, no. 18, pp. 4044-4050, Sept.2000.

[111] T. Parkin and R. Venterea, "Chamber-Baed Trace Gas Flux Measurments," in *USDA-ARS GRACEnet Project Protocols*. R. Follett, Ed. USDA, 2010, pp. 3-1-3-39.

[112] C. de Klein and M. Harvey, *Nitrous Oxide Chamber Methodology Guidelines* Ministry for Primary Industries, 2015.

[113] K. Smith and K. Dobbie, "The Impact of Sampling Frequency and Sampling Times on Chamber-Based Measurements of N2O Emissions From Fertilized Soils," *Global Change Biology*, vol. 7, pp. 933-945, 2001.

[114] L. Barton, R. Kiese, D. Gatter, K. Butterbach-Bahl, R. Buck, C. Hinz, and D. Murphy, "Nitrous Oxide Emissions from a Cropped Soil in a Semi-Arid Climate," *Global Change Biology*, vol. 14, pp. 177-192, 2008.